A STRUCTURAL ANALYSIS OF ZEOLITE-TEMPLATED CARBONS

by

Erin Elizabeth Taylor

A dissertation submitted in partial fulfillment
of the requirements for the degree

of

Doctor of Philosophy

in

Chemistry

MONTANA STATE UNIVERSITY
Bozeman, Montana

December 2022

DEDICATION

I would like to dedicate this work to my high school chemistry teacher, Chris Jacobson. Mr. Jacobson is the reason I fell in love with chemistry and I am certain that this document would not exist without his guidance and enthusiasm. I owe him my deepest thanks for teaching me to see beauty in the world through science.

ACKNOWLEDGEMENTS

First and foremost, I would like to thank my advisor, Dr. Nicholas Stadie. It has been a great pleasure to see him build a lab from the ground up. I thank him for creating a collaborative space for my fellow labmates and me to research. I would also like to thank my labmates, both past and present, for the coffee walks and carbon chats.

Next, I would like to acknowledge those who have expanded my understanding of chemistry throughout the past five years. I thank the members of my committee: Dr. Erik Grumstrup, Dr. Sharon Neufeldt, Dr. Rob Walker, and Dr. Stephanie Wettstein. I thank Dr. Gary Wyss for his patience and company during my trips to Butte for XRD measurements in the early days of my studies. I thank Dr. Robert Szylagi for his endless support in my computational efforts. Dr. Szylagi's chemical intuition has informed a large part of my understanding of zeolite-templated carbon structure. I thank the entire Kyotani Lab for their hospitality and collaboration during my visit to Sendai, Japan. I thank Nishihara-sensei for teaching me how to assess carbon deposition and Nomura-san for teaching me how to template mesoporous graphenes.

Lastly, I would like to thank my family for their unwavering support. I thank Grandpa Sam for inspiring me to explore and Grandma Barbara for reminding me to stop and smell the irises. I thank my siblings for their encouragement, random video chats, and keeping me grounded. I also thank my parents for always motivating me to reach further and reminding me that hard things take hard work. A special thanks is owed to my husband for being my rock, my sounding board, and my best friend throughout this entire process.

TABLE OF CONTENTS

TABLE OF CONTENTS – CONTINUED

TABLE OF CONTENTS – CONTINUED

TABLE OF CONTENTS – CONTINUED

LIST OF TABLES

LIST OF FIGURES

LIST OF FIGURES – CONTINUED

Figure Page

LIST OF FIGURES – CONTINUED

Figure Page

LIST OF FIGURES – CONTINUED

Figure Page

LIST OF FIGURES – CONTINUED

Figure Page

LIST OF FIGURES – CONTINUED

Figure Page

LIST OF FIGURES – CONTINUED

Figure Page

NOMENCLATURE

12MR	12-membered ring
***BEA**	beta zeolite
BET	Brunauer–Emmett–Teller
CIF	crystallographic information file
CVD	chemical vapor deposition
DFT	density functional theory
DVB	divinylbenzene
EMT	EMC-2 zeolite
EDX	energy-dispersive X-ray spectroscopy
FA	furfuryl alcohol
FAU	faujasite zeolite
GCMC	Grand canonical Monte Carlo
HF	hydrofluoric acid
ICP	inductively coupled plasma
m_f	final mass
m_i	initial mass
MS	mass spectroscopy
NaY	sodium exchanged zeolite Y
NLDFT	non-linear density functional theory
OES	optical emission spectroscopy
P-CVD	pulsed chemical vapor deposition
PSD	pore size distribution
REBO	reactive bond order
SA	surface area
SEM	scanning electron microscopy
SPD	structural packing density
SQUID	superconducting quantum interference device
TEM	transmission electron microscopy
TGA	thermogravimetric analysis
TPMS	triply periodic minimal surface
XAS	X-ray absorption spectroscopy
XPS	X-ray photoelectron spectroscopy
XRD	X-ray diffraction
ZTC	zeolite-templated carbon

ABSTRACT

Zeolite-templated carbons (ZTCs) are a distinct class of porous framework materials comprised of a three-dimensional pore network contained between atomically thin, polycyclic hydrocarbon walls. This class of materials arose from the goal to develop carbon-based frameworks with ordered, homogeneous microporosity (see Chapter 1), as opposed to activated carbons where the pore network is random. It has more recently been suggested that zeolite-templating may be a viable synthetic route to carbon schwarzites, an elusive class of theoretical materials, which follow triply periodic minimal surfaces and are predicted to have many fundamentally interesting properties. Herein we show that while experimentally synthesized ZTCs (see Chapters 2 and 3) are too amorphous to be considered schwarzites, understanding the current structural features of ZTCs may be the key to finally isolating a schwarzite via zeolite-templating. The experimentally relevant open-blade model developed in our work predicts paramagnetism of ZTC materials (see Chapter 5); superconducting quantum interference device measurements on archetypical ZTC materials confirms this prediction, highlighting the unique nature of spin polarization in porous carbon materials. While the current ZTC structure resembles an open-blade, generating a closed-tube schwarzite-like ZTC variant may be accessible by tuning the catalytic activity of the zeolite template pore walls. In Chapter 6, alkali metal exchange is explored as a route to strengthen cation-π interactions between the growing ZTC framework and zeolite template in an attempt to achieve a more schwarzite-like ZTC. LiY-templated ZTCs show beginning signs of conversion to a closed-tube structure. Lastly, recent benchmark computational studies suggest that nitrogen-doping of open-blade porous carbon surfaces has a significant, beneficial effect on the binding energy toward methane: a strengthening by up to 3 kJ mol^{-1} over pure carbon. The work presented in Chapter 7 identifies optimal conditions to achieve nitrogen-doped ZTCs with N-contents ranging from 0-9 at%. Therein, we show that indeed high-pressure (100 bar) methane adsorption characterization of nitrogen-doped ZTCs exhibit an increased methane binding energy of 1.3 kJ mol^{-1}, validating the theoretical predictions.

Best enjoyed with peppermint tea.

CHAPTER ONE

INTRODUCTION

1.1 Carbon Allotropes

Carbon is one of the most versatile elements from the perspective of chemical bonding, with the ability to form single, double, and triple bonds to other carbon atoms as well as an assortment of heteroatoms.[1] Simply changing the bonding hybridization in pure carbon materials from sp^2- to sp^3-hybridized, corresponding to graphite and diamond (Figure 1.1), respectively, leads to dichotomous structural, electrical conductivity, and thermal conductivity properties (see Table 1.1). Prior to 1985, graphite and diamond were the only known solid forms of pure carbon. That was, until the isolation of buckminsterfullerene (Figure 1.2), a zero-dimensional network solid of sp^2-hybridized carbon,[2] initiated the "era of carbon allotropes".[3] Since then, one- and two-dimensional sp^2-hybridized carbon allotropes have been realized in the form of carbon nanotubes[4] and graphene,[5] respectively (see Figure 1.2).

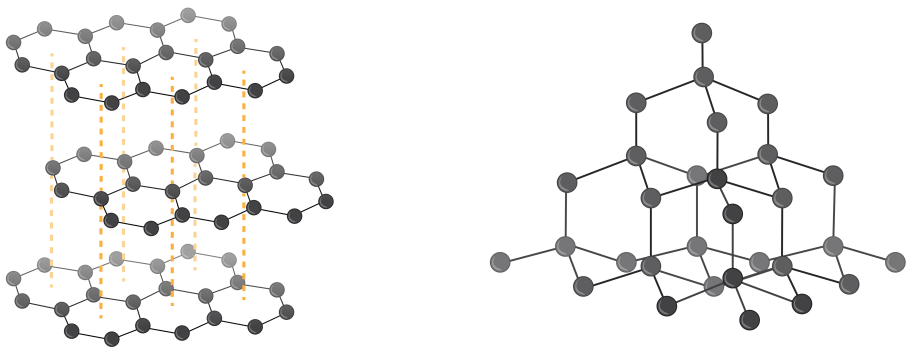

Figure 1.1: Carbon structures: graphite (left) and diamond (right).

Table 1.1: Material properties of graphite and diamond.

Material	Hardness[6] (Mohs Scale)	Electrical Conductivity [a,6] (mho m^{-1})	Thermal Conductivity[a,6] (W mol^{-1} K^{-1})
Graphite	0.5	18.9×10^{4}	268.0
Diamond	10	10^{-12}	545.0

[a] at 293 K

Graphite is made of layered graphene, atomically thin sheets of interlocking six-membered sp^2-hybridized carbon rings. However, isolating a single sheet of graphene reveals unique properties such as remarkable material strength and ballistic electrical conductivity.[7,8] Conceptually cutting and rolling a graphene sheet results in the one-dimensional sp^2-hybridized allotrope known as a carbon nanotube. Introducing five-membered rings into the graphene lattice causes the sheet to fold in on itself, resulting in a zero-dimensional analog known as fullerene, one of which is C_{60} buckminsterfullerene. Just as wrapping graphene (introducing positive Gaussian curvature) leads to the lower dimensional carbon networks, isolating the last structure in the series of sp^2-hybridized carbon allotropes requires graphene to be "unwrapped" or lifted into the third dimension.

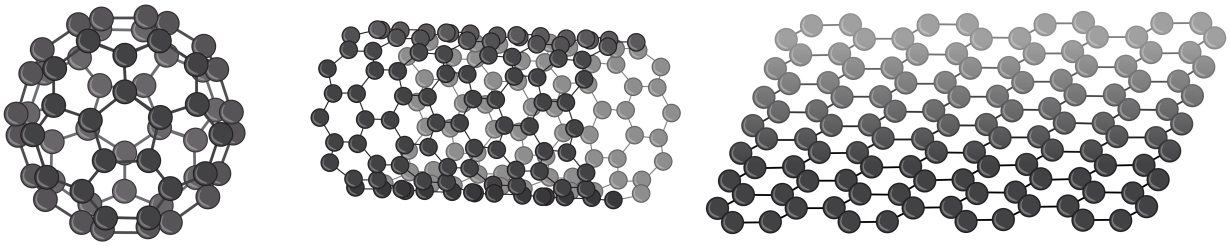

Figure 1.2: Pure sp^2-hybridized carbon allotropes, from left to right: C_{60} buckminsterfullerene, a single-walled carbon nanotube, and graphene.

1.2 Carbon Schwarzites

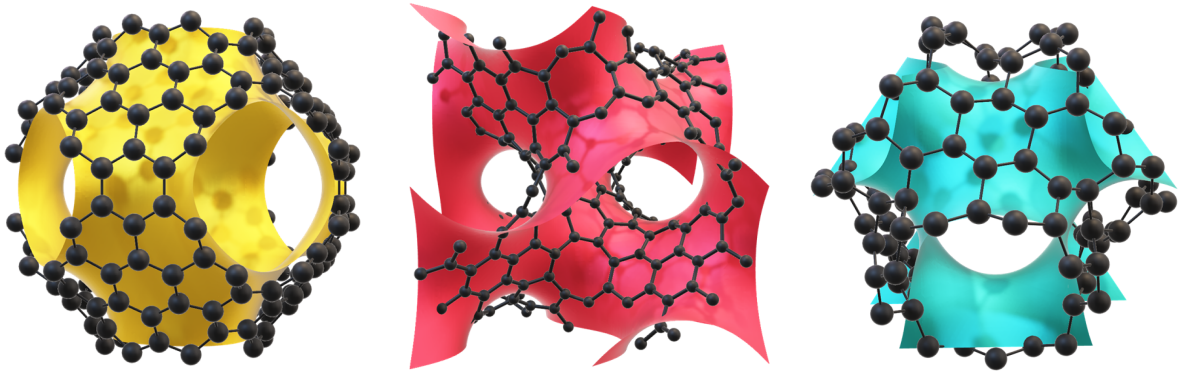

Figure 1.3: From left to right: P8bal schwarzite (black) overlaid on Schwarz P-Surface (yellow), G8bal schwarzite (black) overlaid on Schoen G-Surface (red), D766 schwarzite (black) overlaid on Schwarz D-Surface (blue).

Three-dimensional sp^2-hybridized carbon network solids were first described in 1991 by David Jones,[9] a prolific science communicator known for his eccentric scientific musings. Under the pen name of Daedalus,[10] Jones described a hypothetical "ultra-fine soap-foam" composed of a monolayer of carbon, like a porous "polymeric higher fullerene". Later that same year, Mackay and Terrones published the first atomistic rendering of such a structure, known as P8bal (see Figure 1.3).[11] The resulting material is a double-sided surface made of sp^2-hybridized carbon with negative Gaussian curvature. In graphene, six-membered sp^2-hybridized carbon rings give the sheet its flat topology. To induce negative Gaussian curvature, Mackay and Terrones systematically added eight-membered rings which pucker due to the decreased C-C-C bond angle. The surface they constructed follows a triply periodic minimal surface (TPMS) known as the Schwarz P-surface, shown in Figure 1.3. Mackay and Terrones also note that other Schwarz surfaces could be generated with carbon, including the Schwarz D-surface which would ironically create a diamond network

from graphene. In 1992, Lenosky et al. added to the library of triply periodic sp^2-hybridized carbon frameworks, and termed these class of structures "schwarzites",[12] partly because of the materials' anticipated black color ("schwarz" translating to "black" in German) but most notably after the mathematician Hermann Schwarz,[13] who along with Alan Schoen,[14] was attributed with the discovery of Schwarz surfaces, a subset of TPMSs (see Figure 1.3). Around this time, a handful of other research groups began publishing new models ultimately compiling a set of nine smallest schwarzite structures, shown in Figure 1.4.[15–21]

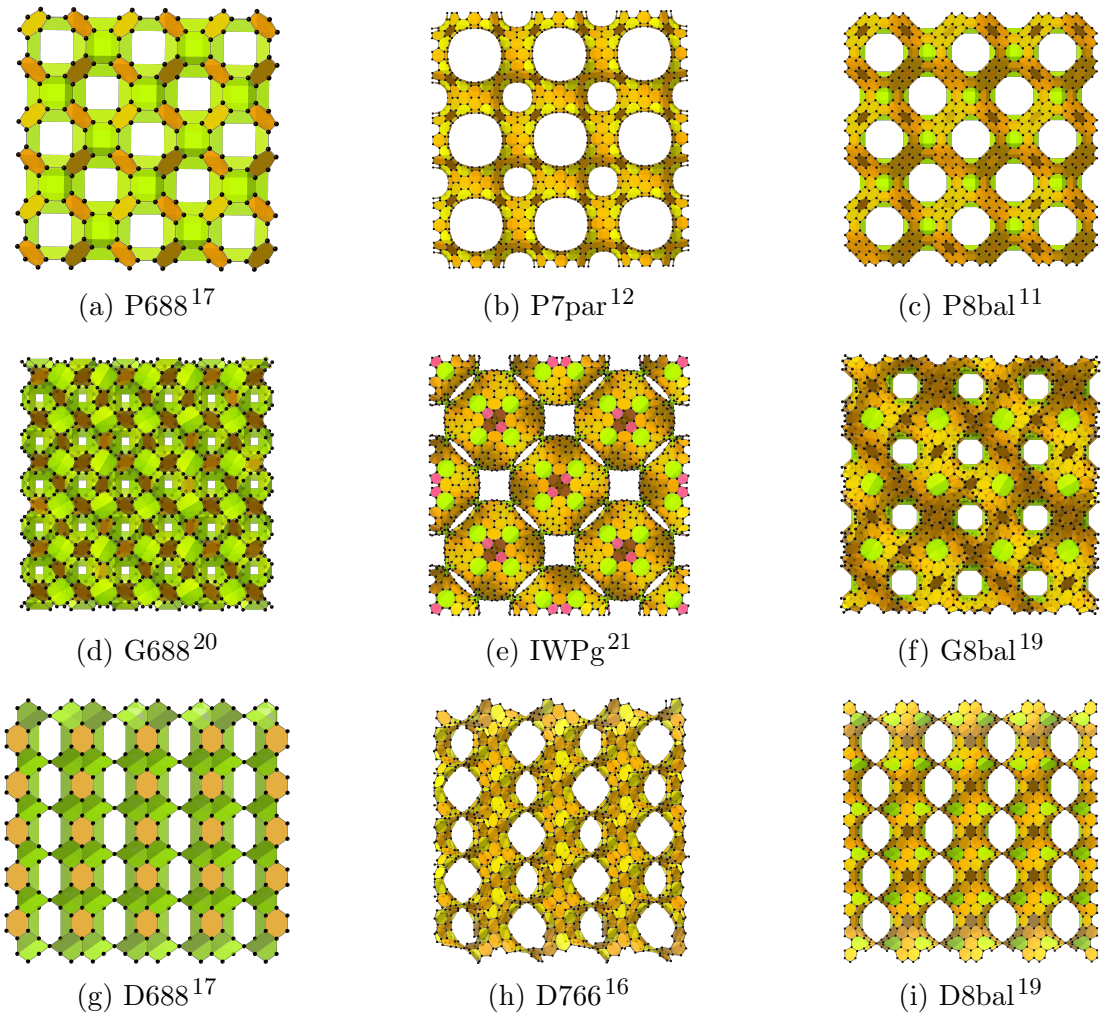

(a) P688[17] (b) P7par[12] (c) P8bal[11]

(d) G688[20] (e) IWPg[21] (f) G8bal[19]

(g) D688[17] (h) D766[16] (i) D8bal[19]

Figure 1.4: Extended multicell schwarzite frameworks with five-, six-, seven-, and eight-membered rings highlighted in pink, orange, yellow, and green, respectively.

By definition, TPMSs are balanced surfaces, equally dividing space into two identical volumes; however, not all proposed carbon schwarzite-like frameworks are balanced surfaces.[12,19] While the introduction of eight-membered rings (P8bal, G8bal, and D8bal) can result in balanced schwarzites, the addition seven-membered rings (P7par and D766) yields structures which are parallel to the Schwarz surfaces, dividing space into two unequal volumes.[19]

1.3 Predicted Properties of Schwarzites

Since schwarzites discovery, scientists have modeled schwarzite and schwarzite-like material characteristics, predicting that these structures could exhibit rare mechanical and electronic properties. Like graphene, schwarzites are also predicted to be ballistic electrical conductors.[22] Some schwarzite structures are predicted to be extremely flexible (bulk modulus: 95 GPa).[23] The G8bal structure in particular is expected to demonstrate auxetic behavior (negative Poisson's ratio),[23] meaning that when stretched G8bal would become thicker perpendicular to the applied force, and vice versa. Auxetic materials are of interest due to their counter-intuitive behavior and accompanying unique properties.[24,25] Other schwarzites are predicted to be exceptional energy absorbers, outperforming even Kevlar, with specific energy absorbance estimations of 500 kJ kg^{-1}, compared to 0.09 kJ kg^{-1}, respectively.[23] While theoretical material property calculations anticipate rare properties of schwarzites, energetic calculations predict that schwarzites should be more energetically stable than the already realized C_{60} buckminsterfullerene (Table A.1). Yet, schwarzites remain elusive in the laboratory as of this writing.

1.4 Synthesizing Schwarzites

In 1992, Lenosky et al. conceptually explored the possible routes to isolating carbon schwarzites.[12] They reasoned that fullerenes (positive Gaussian curvature) form as the result of slow growth, and thus analogously schwarzites (negative Gaussian curvature) should result from fast, explosive crystallization. Furthermore, they noted that these conditions probably exist in the carbon-arc fullerene synthesis and could be ideal for schwarzite formation. Such experiments have been investigated and revealed amorphous porous carbon foam materials.[26] Organic tiling has also been attempted using Suzuki coupling of ketone-functionalized aromatic saddles with borinic acid to form carbon nanobelts or schwarzite fragments. However, first attempts at assembling these saddles into schwarzite fragments were not successful.[27] Another route to realizing schwarzites in the laboratory is by depositing carbon onto a template with a pre-existing TMPS topology.

1.5 Early Zeolite-Templated Carbons

Attempts to control carbon structure via templating began in 1982 when silica gels and porous glasses were impregnated with polymers which were then carbonized to form amorphous porous carbons.[28] However, three-dimensional template fidelity was not maintained until the use of a three-dimensionally ordered zeolite template was introduced as a concept in 1997 by Kyotani and coworkers, resulting in the first zeolite-templated carbon (ZTC).[28,29] Kyotani and coworkers introduced two methods for templating zeolites, by either impregnating the porous template with a liquid polymeric precursor which could later be carbonized, or using chemical vapor deposition (CVD). The first ZTC with structural regularity imparted from the zeolite template, i.e. pore-to-pore ordering, was finally observed in 2000.[30,31]

CHAPTER TWO

SYNTHESIS AND CHARACTERIZATION OF ZEOLITE-TEMPLATED CARBONS

2.1 Two-Step Zeolite-Templated Carbon Synthesis

Since 2000, ZTCs have been synthesized a myriad of ways, with the highest template fidelity samples synthesized via a two-step method, as shown in Figure 2.1. In this method, a sacrificial zeolite template is impregnated with a liquid polymeric precursor. After impregnation the polymeric precursor is polymerized, pyrolyzed, and further carbon deposition is achieved via CVD with the introduction of small carbon gases. Following CVD, the zeolite-carbon composite undergoes a heat-treatment step to firm up the carbon structure, such that when the zeolite is removed, a free-standing three-dimensional carbon framework material is revealed.

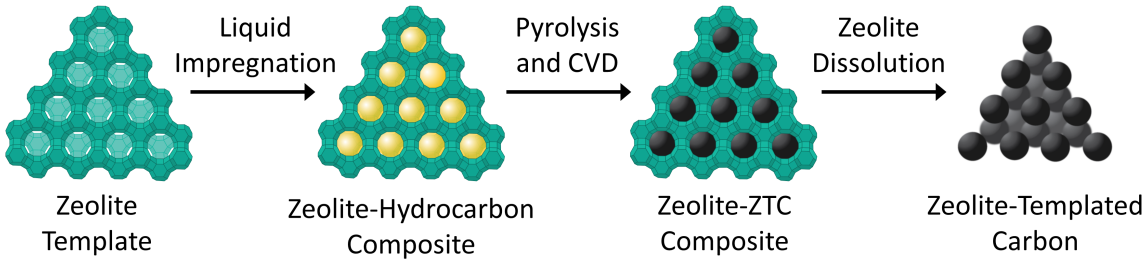

Figure 2.1: Typical zeolite-templated carbon synthesis strategy: zeolite impregnation and polymerization by a liquid polymeric precursor (optional), hydrocarbon pyrolysis (i.e., carbonization) with or without chemical vapor deposition (CVD), and template removal (i.e., zeolite dissolution).

2.1.1 Zeolite Templates

Zeolites are a class of more than 240 framework types of microporous aluminosilicate minerals with a crystalline pore structure,[32] and are most known for their use as catalysts in hydrocracking of petroleum-based fuels. Not all zeolites are suitable candidates for the

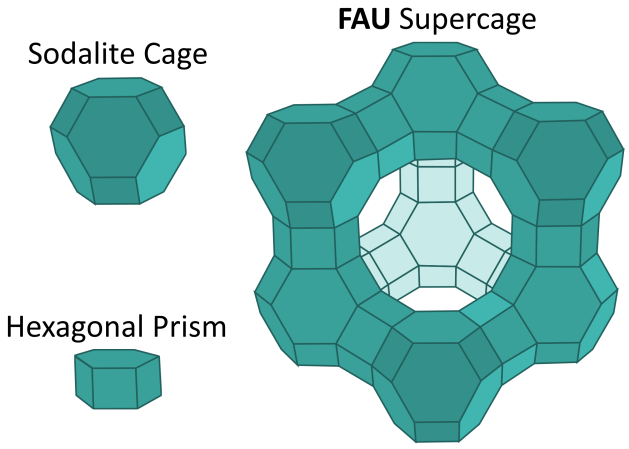

Figure 2.2: **FAU** zeolite building blocks (left) and supercage looking down a 12MR pore opening (right). T-sites (Si or Al) are shown as the vertices of a polyhedral depiction of **FAU** (teal lines and faces) and zeolitic oxygen sites and cations are omitted for clarity.

synthesis of ZTCs. Eligible zeolite candidates must have a three-dimensionally connected pore network and pores large enough to host carbon precursors in order to generate a free standing three-dimensionally connected carbon network. Computational efforts have identified a small library of ZTC template candidates, including: ***BEA**, ***BEB**, **BEC**, **-CLO**, **CON**, **EMT**, **FAU**, **IRR**, **-IRY**, **ISV**, **ITT**, **-ITV**, **IWR**, **IWS**, **IWW**, **MSE**, **POS**, **RWY**, **SAO**, **SBS**, and **SBT**.[33,34] The International Zeolite Association (IZA) designated framework type code is listed in bold face and zeolites with disordered porous networks are indicated with an asterisk (*). To date, well-replicated carbon network materials have only been made using ***BEA**[35–52], **EMT**[44,46,51,53–58], and faujasite (**FAU**) zeolite templates. The entirety of this work is focused on **FAU**-templated ZTC materials (**FAU**-ZTCs).

FAU, shown in Figure 2.2 is the most commonly used template in ZTC synthesis, due to its commercial availability, high symmetry, thermal stability, and tunable catalytic properties. **FAU** is classified as a 12-membered ring (12MR) zeolite, since the pore entrance contains 12 T-sites, occupied by silicon in a pure SiO_2 zeolite. The **FAU** structure carries the

D-surface topology (Figure 1.3) and is made up of sodalite cages, connected by hexagonal prisms, as shown in Figure 2.2. Zeolites can undergo a substitution of silicon (4+) with aluminum (3+), requiring the introduction of extra-framework charge-balance cations. For example, **FAU** zeolites can be exchanged with a wide range of cations: most commonly Na^+, K^+, Ca^{2+}, NH_4^+, or H^+.[59] Aluminum-substituted **FAU** zeolites are commonly named with the charge-balance cation followed by an indicator for the substitution amount. A ratio of silicon to aluminum of 1-1.5 is classified as an X-type zeolite and a ratio larger than 1.5 is classified as a Y-type zeolite.[60] A sodium-exchanged **FAU** zeolite with a Si:Al ratio of >1.5 is referred to as NaY.

2.1.2 Liquid Impregnation

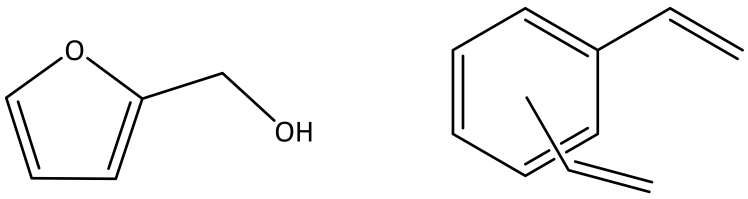

(a) (b)

Figure 2.3: Common liquid polymeric precursors used in two-step ZTC synthesis procedures: a) FA and b) DVB.

Liquid impregnation is an optional step when synthesizing ZTCs that involves filling the zeolite pores with a liquid polymeric precursor which can later undergo polymerization creating nanographene islands. These nanographene islands are later connected via CVD and are imperative for high template fidelity.[61] The most common polymeric precursor is furfuryl alcohol (FA, Figure 2.3a) which is used in excess for impregnation via soaking and is later washed from the surface of the zeolite with mesitylene (see Appendix B). Recently, divinylbenzene (DVB, Figure 2.3b) has been introduced as an alternative, oxygen free polymeric precursor with facile polymerization conditions.[61] Whereas typical FA

impregnation requires a 24 h soaking period followed by filtration and washing before 24 h of polymerization, DVB impregnation uses a fraction of the precursor, does not require washing, and is fully polymerized within 2 h of impregnation. ZTC materials synthesized with either FA or DVB impregnation show very similar templating fidelities and material characteristics.[61] It is therefore expected that in the future, DVB will be the liquid polymeric precursor of choice for ZTC synthesis. Other precursors are also being developed[62] and this remains an active area of research. All materials made in this work are impregnated with FA before CVD.

2.1.3 Chemical Vapor Deposition Synthesis Parameters

After liquid impregnation and polymerization, additional carbon is introduced via CVD, where small carbon gases flow over/through the zeolite bed at high temperatures. Many carbon CVD gases have been used to successfully synthesize **FAU**-ZTCs, including methane[63], acetylene[48,64–80], ethylene[46,50,81–92], propylene[30,31,51,57,61,62,93–119], and butylene[96,120]. Liquid precursors can also be used during CVD, by bubbling an inert gas through volatile liquid precursors.[91,121] This work mainly describes **FAU**-ZTCs synthesized using propylene and later (Chapter 7) explores nitrogen incorporation via acetonitrile deposition.

2.1.4 Heat-Treatment

After CVD, a heat-treatment step is required to anneal the carbon structure inside the zeolite template. Heat-treatment inside of NaY typically occurs at 900 °C, which is near but just below the thermal decomposition of the zeolite template (see Figure 2.4).

2.1.5 Template Etching

Removal of the zeolite is typically achieved via washing with hydrofluroic acid (HF) (Appendix B.4). However, safety concerns (especially when scaling up ZTC production) has lead to the use of other acids and bases to etch the template.[50]

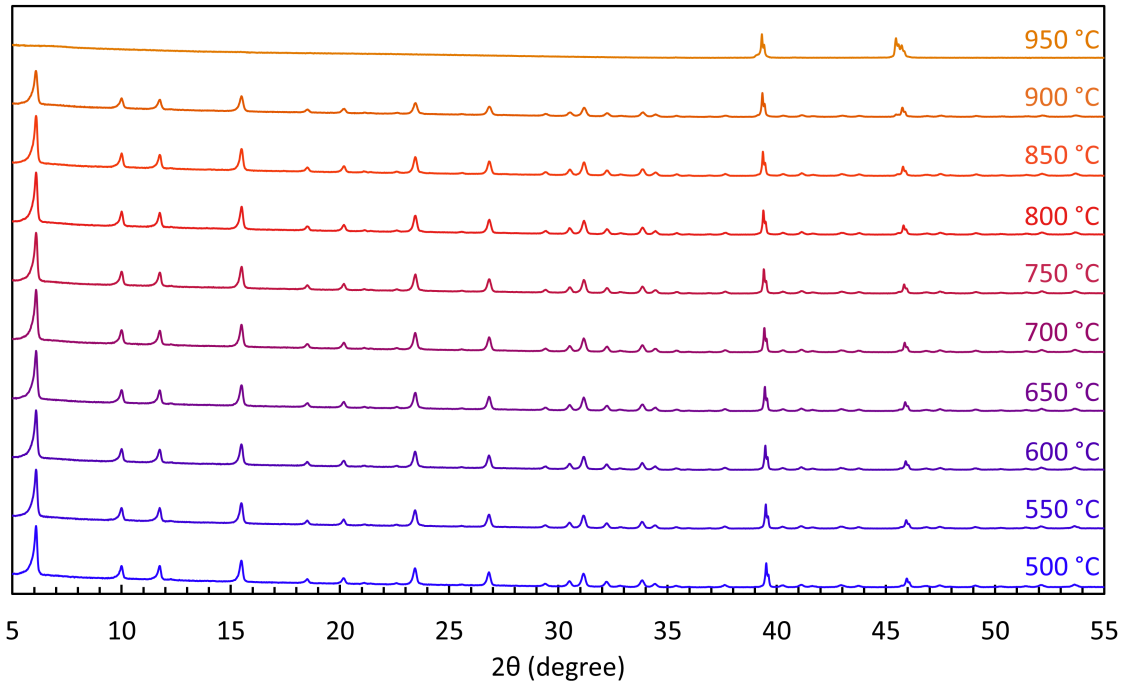

Figure 2.4: High-temperature XRD patterns, collected for the purposes of this work, of NaY under flowing argon. To best replicate ZTC synthesis conditions, XRD patterns were collected by heating at 5 °C per min starting at 500 °C collecting patterns every 50 °C up to 950 °C, at which point the crystallinity of the zeolite was lost. The remaining peaks at 950 °C appearing at $2\theta \approx 39°$ and $2\theta \approx 46°$ originate from the platinum sample holder.

2.2 Zeolite-Templated Carbon Characterization

2.2.1 Powder X-Ray Diffraction

As seen in Figure 2.5, the zeolite template (NaY) is a highly ordered crystal, as indicated by the well defined diffraction peaks, especially at high angles. Successful templating of a **FAU**-ZTC is indicated by the replication of the **FAU** (111) reflection at $2\theta \approx 6.3°$ using Cu Kα radiation. Optimized procedures have also resulted in the appearance of the **FAU** (220) and (311) reflections at $2\theta \approx 10.3°$ and 12.5°, respectively. The diffraction planes imparted to the ZTC are shown for clarity on the native **FAU** template in Figure 2.6. Poor templating is indicated by the presence of a peak at $2\theta \approx 26°$, corresponding to the (002)

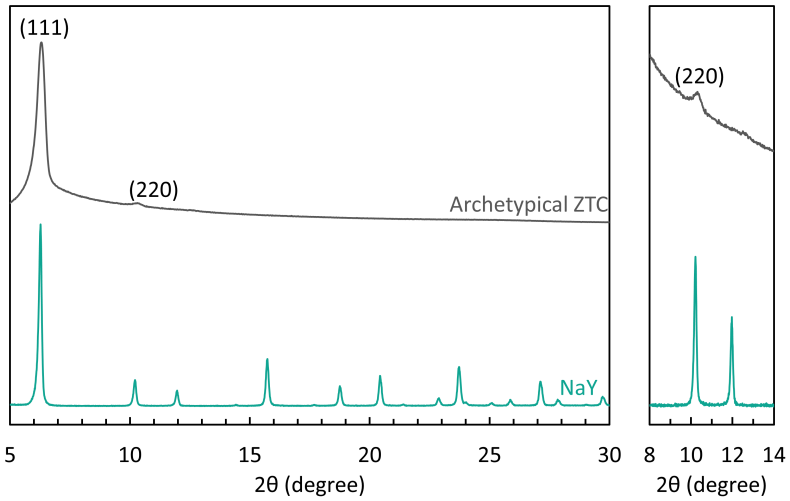

Figure 2.5: XRD pattern of zeolite NaY and an NaY-templated ZTC with high template fidelity, with replicated planes indicated on the **FAU** framework shown on the right.

reflection of graphite. This is the result of either over-templating, i.e., graphitic growth on the outside of the zeolite template, or poor connectivity of the carbon network during synthesis, leading to collapse of the ZTC framework upon dissolution of the template.

2.2.2 Thermogravimetric Analysis and Structural Packing Density

Thermogravimetric analysis (TGA) is used to determine the amount of carbonaceous material deposited within the zeolite template. Upon heating the zeolite-ZTC composite to 800 °C in air, the carbonaceous material can be completely oxidized leaving behind the original zeolite. By analyzing the initial and final mass, the experimental structural packing density (SPD_{exp}) can be determined, as defined below:

$$SPD_{exp} = \frac{m_{ZTC}}{m_{zeolite}} = \frac{m_i - m_f}{m_f} = g_{ZTC}\, g_{zeolite}^{-1} \tag{2.1}$$

In Equation 2.1, m_i is the mass of the dried zeolite-ZTC composite (e.g., 16.219 mg as shown in Figure 2.7) and m_f is the mass of the zeolite (e.g., 11.978 mg as shown in Figure 2.7).

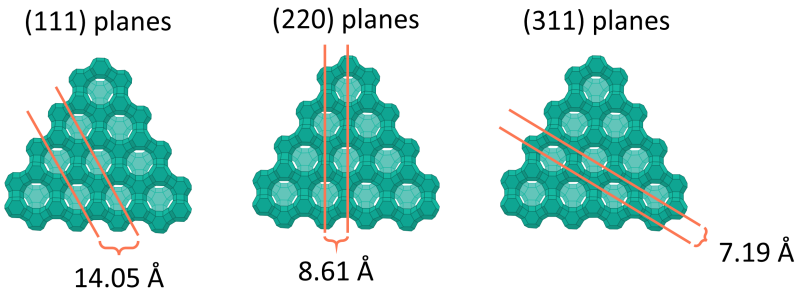

Figure 2.6: XRD pattern of zeolite NaY and an NaY-templated ZTC with high template fidelity, with replicated planes indicated on the **FAU** framework shown on the right.

Using Equation 2.1, the SPD_{exp} of the ZTC shown in Figure 2.7 is 0.35 g_{ZTC} $g^{-1}_{zeolite}$. This metric is useful when comparing ZTCs synthesized on the exact same zeolite template (e.g., **FAU** zeolite with a Si:Al ratio of 5.5 charge balanced with sodium cations). However, even zeolites of the same type may contain different Si:Al ratios or different charge-balance cations, resulting in difference zeolite masses. Thus, SPD_{exp} cannot be used to compare ZTCs synthesized within different zeolite templates. Instead, SPD_{exp} must be converted to one of two other metrics: SPD_{cell} or $SPD_{cell,vol}$.[118] The first, SPD_{cell}, can be used to compare across the same zeolite template type (e.g., **FAU**-ZTC) and the second, $SPD_{cell,vol}$, can be used across arbitrarily different zeolites (e.g., ***BEA**-ZTC vs. **FAU**-ZTC). These metrics are defined as follows:

$$SPD_{cell} = \frac{m_{ZTC}}{m_{SiO_2}} = SPD_{exp} \times \frac{MW_{zeolite}}{MW_{SiO_2}} = g_{ZTC}\, g^{-1}_{SiO_2} \tag{2.2}$$

$$SPD_{cell,vol} = \frac{m_{ZTC}}{mL} = SPD_{exp} \times \frac{MW_{zeolite}}{MW_{SiO_2}} \times \frac{1}{v_{cell,pore}} = g_{ZTC}\, mL^{-1} \tag{2.3}$$

In Equations 2.2 and 2.3, $MW_{zeolite}$ is the weight of the zeolite's unit cell, MW_{SiO_2} is the weight of the same zeolite unit cell assuming the zeolite template is comprised purely of SiO_2, and $v_{cell,pore}$ is the accessible pore volume of an idealized SiO_2 framework (based

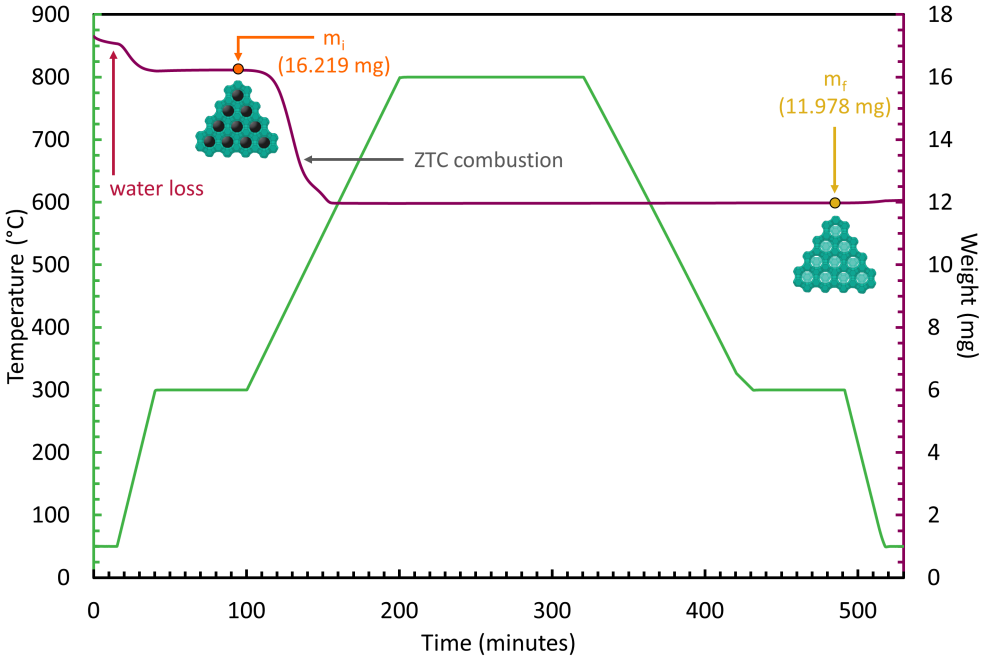

Figure 2.7: Thermogravimetric data of ZTC fully oxidizing inside of zeolite template while heating under exposure to air.

on a 2.8 Å probe molecule as designated by the International Zeolite Association[32]). Using Equation 2.2, the SPD_{cell} becomes 0.38 g_{ZTC} $g^{-1}{}_{SiO_2}$. The average SPD_{cell} values of **FAU**-ZTCs range from 0.32 to 0.40 g_{ZTC} $g^{-1}{}_{SiO_2}$. Higher SPD_{cell} values have been measured, but only for over-templated ZTCs where a core-shell structure is clearly observed.[72,77]

SPDs when combined with other characterization techniques can be used to determine the quality of a resulting ZTC material. Low SPD_{cell} (<0.30) indicates incomplete templating and will often lead to collapse of the carbon framework upon zeolite dissolution. Archetypical ZTCs exhibit SPD_{cell} ranging from 0.32-0.45 with generally the higher the SPD the more complete the templating of resulting ZTC. However, an increase in SPD does not always indicate successful templating as deposition of carbon on the outer surface of the zeolite can also result in an increased SPD. Thus, it is imperative to use a combination of characterization techniques to assess the state of the resulting ZTC material.

2.2.3 Chemical Composition

TGA can also be used to distinguish between the amount of carbon deposited within the zeolite as opposed to on the outer surface of the zeolite particles[72,77] and the relative quantity and type of O- and H-containing functionalities within the ZTC structure when combined with gas chromatography or mass spectroscopy.[72,102] High-quality archetypical **FAU**-ZTC exhibits a benchmark chemical composition of $C_{75.3}H_{19.0}O_{5.7}$ (where the O-containing functionalities are primarily attributed to ether, alcohol, acid anhydride, and some carbonyl groups) and exhibits only negligible carbon deposition on the outer surface. It has been determined by several ^{13}C solid-state NMR spectroscopy studies that **FAU**-ZTC consists predominantly of sp^2-hybridized carbon.[31,46,105]

2.2.4 Nitrogen Adsorption

Nitrogen (N_2) adsorption at 77 K is an important method for the primary structural characterization of ZTCs in the laboratory. All ZTCs exhibit sharply increasing N_2 adsorption uptake below $P/P_0 = 0.1$, which is typical of micropore filling, and very low additional uptake above $P/P_0 = 0.2$, with a distinct knee (see Figure 2.8). This is direct evidence that a majority of the N_2 accessible pore volume in ZTCs is within micropores with a narrow distribution in size.

Well-replicated ZTCs show a narrow non-local density functional theory (NLDFT) pore-size distribution (PSD) centered around 1.2 nm, as seen in Figure 2.9, indicating atomically thin connectivity of the carbon structure (having a pore-to-pore repeat distance of only 1.4 nm). Some of the N_2 uptake at $P/P_0 > 0.1$ may be attributable to adsorption in interparticle voids, while some also arises from imperfect templating (e.g., from heterogeneous carbon filling within the zeolite particles). Archetypical **FAU**-ZTC exhibits an almost flat plateau (see Figure 2.8) corresponding to ~45 mmol g^{-1} N_2 uptake (1000–1200 mL_{STP} g^{-1}), which is equivalent to ~4000 m^2 g^{-1} of geometrical surface area (SA) assuming that each nitrogen

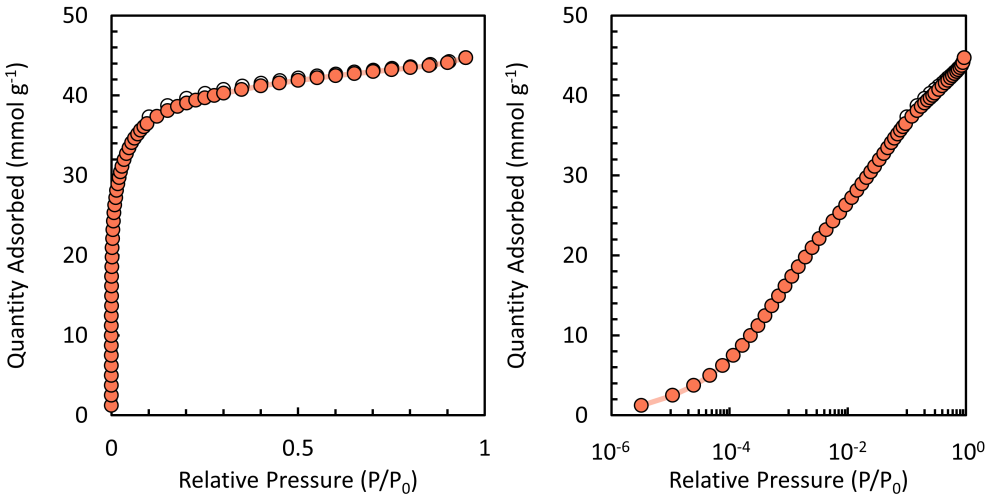

Figure 2.8: Nitrogen adsorption isotherms (left) of archetypical ZTC shown using a log scale on the right.

molecule adsorbed is resident on only one wall of the pore and occupies 0.162 nm^2 of surface, a standard convention.[122] N_2 adsorption at 77 K can also be used to determine the Brunauer-Emmett-Teller (BET) SA of porous materials. Archetypical laboratory synthesized **FAU**-ZTCs exhibit BET SAs ranging from 3200-3800 $m^2\ g^{-1}$, much larger than that of double-sided graphene; indicative of a structure that is accessible to N_2 on both sides with a significant number of edge sites.

2.2.5 Transmission Electron Microscopy

Particle morphology and pore-to-pore spacing is also evidenced by transmission electron microscopy (TEM), as seen in Figure 2.10, with a regular pore spacing of 1.4 nm.

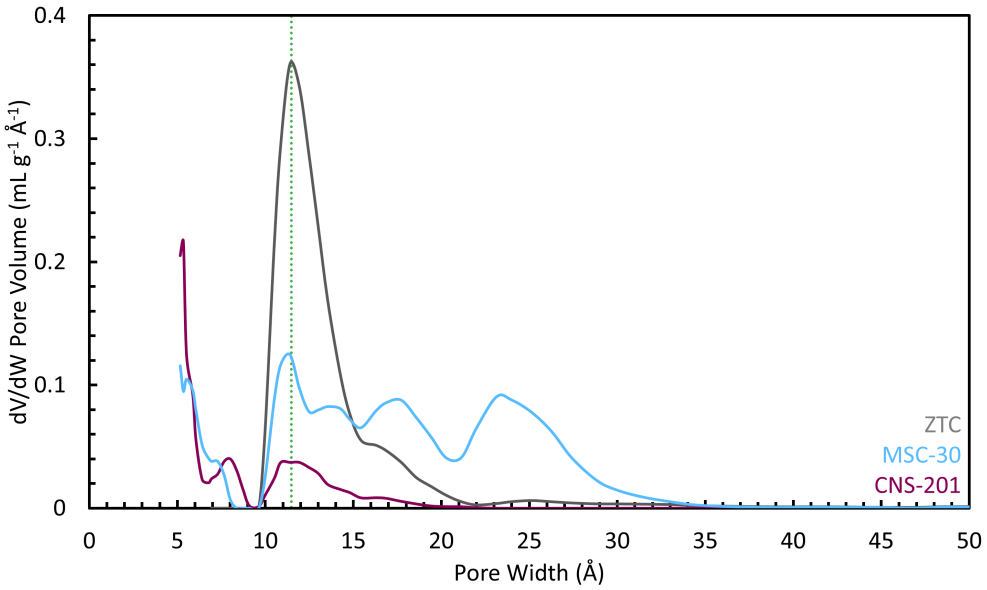

Figure 2.9: Experimental and theoretical N_2-accessible pore-size distributions for **FAU**-ZTC, MSC-30, and CNS-201.

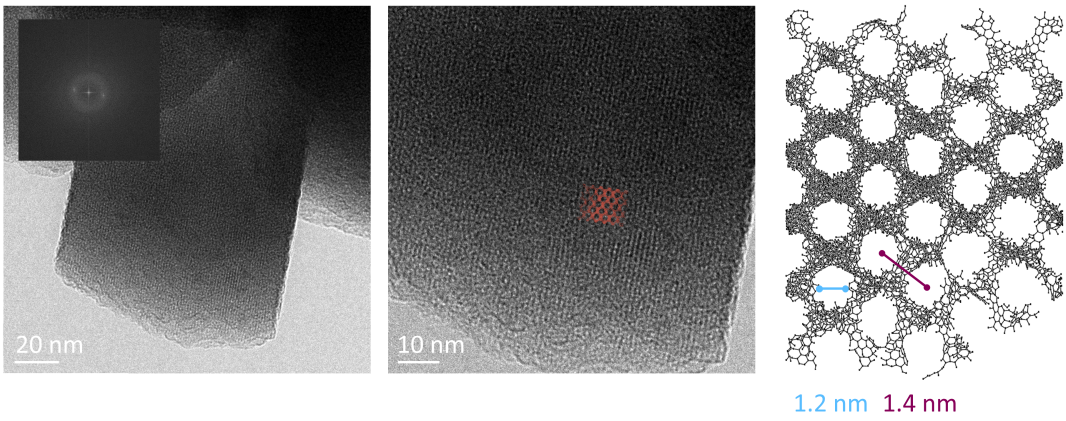

Figure 2.10: From left to right: TEM micrograph of **FAU**-ZTC and the Fourier transform of the image (inset), atomistic ZTC model overlaid on TEM micrograph, and atomistic ZTC model with pore-to-pore spacing and pore size shown in purple and blue, respectively.

CHAPTER THREE

OPTIMIZING CVD PARAMETERS FOR ZEOLITE-TEMPLATED CARBON SYNTHESIS

Among the numerous variables in the ZTC synthesis procedure, optimizing CVD temperature and time are crucial for ensuring the ZTC network is fully templated inside the zeolite pore without framework collapse or the presence of graphitic build up on the external surface of the zeolite. This process is typically unique to each laboratory and setup. Actual CVD optimization methods designed and executed by the author have been included in this chapter for the reader's reference.

Table 3.1: ZTC synthesis optimization material characteristics.

CVD Deposition Temperature	CVD Deposition Time	SPD_{cell} g_{ZTC} ($g^{-1}_{SiO_2}$)	BET SA (m^2 g^{-1})
500 °C	5 h	0.22	1880
600 °C	5 h	0.29	2780
700 °C	4 h	0.38	3360
700 °C	4.5 h	0.38	3380
700 °C	5 h	0.38	3560
700 °C	5.5 h	0.40	3690
700 °C	6 h	0.40	3400
800 °C	5 h	0.62	2150

The analysis of ZTC structure requires the use of a combination of at least three characterization techniques together. For example, as shown in Table 3.1, increasing the

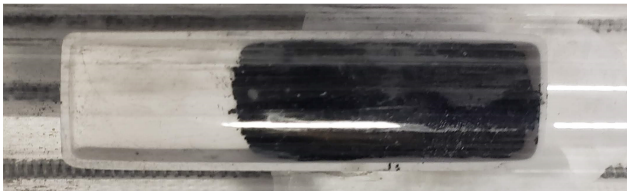

(a) 700 °C propylene deposition.

(b) 800 °C propylene deposition.

Figure 3.1: ZTC-zeolite composite in alumina boat inserted into a quartz tube, after propylene CVD for 5 h.

CVD temperature can cause a drastic increase of the SPD, with the highest SPD exhibited using 800 °C. However, the extra-framework charge-balance cations in the zeolite template serve as catalytic sites for carbon deposition. This necessitates CVD temperatures below typical carbon gas decomposition temperatures, allowing for selective deposition of gaseous precursors inside the zeolite pore network. For example, the decomposition temperature of propylene is 750 °C.[28] Thus, depositing carbon at temperatures at or above 750 °C will lead to uncontrolled carbon deposition, as seen by deposition of carbon on the quartz tube and alumina boat in Figure 3.1b.

Uncontrolled deposition is also evidenced by XRD with the emergence of the graphitic stacking (002) peak as shown in Figure 3.2. All intact **FAU**-ZTCs must exhibit a (111) reflection, indicative of the pore-to-pore order inherited from the zeolite template. In the temperature series shown in Figure 3.2, propylene deposition is not catalyzed until 700 °C with the appearance of a sharp and intense (111) reflection peak. A well templated ZTC will also replicate the (220) reflection as seen at $\sim 10.3^{\circ}$. These peaks are also observed at 800 °C, indicating a core shell structure where a graphitic shell encapsulates a ZTC interior.

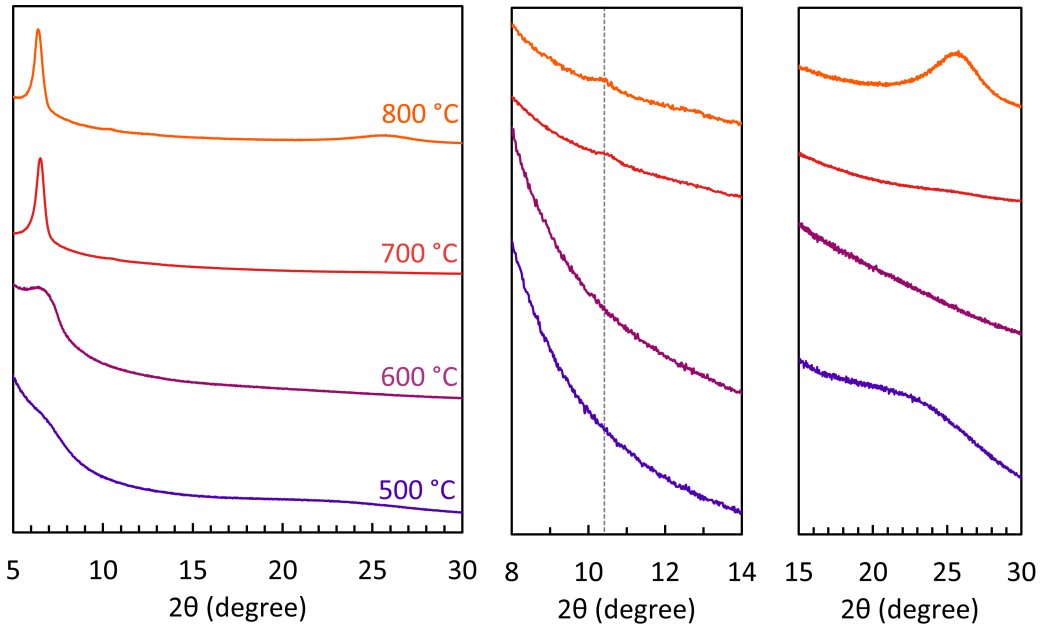

Figure 3.2: XRD patterns of ZTCs synthesized via propylene deposition at various CVD temperatures.

The presence of a graphitic shell is also evidenced by a decrease in the surface area from 700 °C to 800 °C (Table 3.1), as N_2 cannot access the interlayer spaces of graphite.

After identifying the CVD temperature of choice, further optimization can be achieved by varying the CVD time. All of the samples synthesized in the CVD time series shown in Figure 3.3, exhibit an intense sharp (111) reflection, with varying degrees of (220) peak intensity. However, as the CVD time increases, a slight graphitic hump can be seen in at $\sim 25^{\circ}$, as the pores of the zeolite have been blocked causing graphitic build up. Increasing the CVD time does not have a large effect on the SPD of the samples (see Table 3.1), however, an optimal BET SA can be observed at 5.5 h of deposition.

Combining the SPD, BET SA and XRD patterns of the ZTCs synthesized using the above CVD temperature and time series results in an optimized CVD procedure with propylene deposition at 700 °C for 5 h.

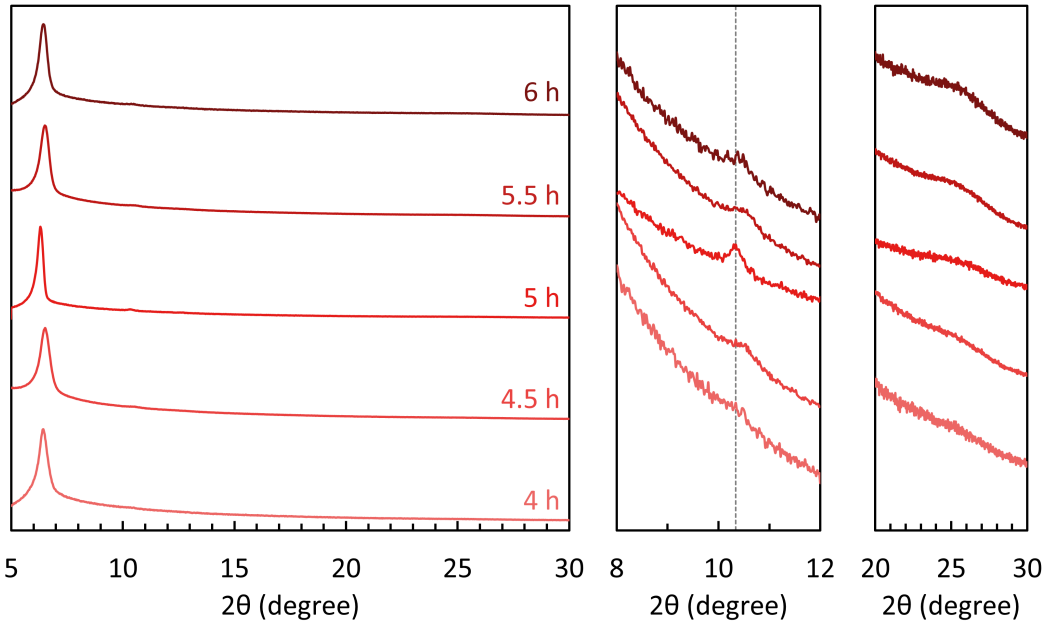

Figure 3.3: XRD patterns of ZTCs synthesized via 700 °C propylene deposition at various CVD times.

CHAPTER FOUR

ATOMISTIC STRUCTURES OF ZEOLITE-TEMPLATED CARBONS

4.1 Modeling Amorphous Carbons

Based on theoretical predictions of schwarzites (Chapter 1.3) and experimental characterization of ZTC materials (Chapter 2), it is apparent ZTCs do not resemble the schwarzite-like structures predicted in the 1990s. Reviewing atomistic models can be useful for understanding current structural limitations in the laboratory. Despite the fact that all synthetic ZTC materials prepared to date are amorphous at the atomic scale, pore-to-pore order is inherited from the zeolite template, making atomistic modeling of ZTC structure a challenging yet feasible endeavor. To date, a comparison of all ZTC atomistic models has not been presented. This work develops and utilizes techniques to compare all existing **FAU**-ZTC atomistic models and experimental characterization, ultimately identifying a ZTC atomistic model which most accurately represents real-world ZTC materials.

4.2 Theoretical Model Material Properties

4.2.1 Theoretical XRD Pattern Simulations

Powder XRD patterns were simulated for each of the periodic atomistic models of **FAU**-ZTC using openly accessible software (Mercury, v4.1.3, Cambridge Crystallographic Data Centre)[123] with a simulated wavelength of 1.54056 Å, a step size of 2θ=0.2°, and a full-width half-maximum (FWHM) of 2θ=0.1°.

4.2.2 Theoretical Surface Area

N_2 accessible SA calculations were performed using openly accessible software (Zeo++, v.0.3)[124] assuming a channel and probe radius of 1.86 Å , corresponding to N_2,[125] with 2000

Monte Carlo samples per atom. Refer to Appendix E for more information on calculations using Zeo++.

4.2.3 Theoretical Structural Packing Density

SPDs were calculated for all of the periodic atomistic models by determining the number (and mass) of all atoms within the unit cell per unit cell volume using the reported crystallographic information file (CIF) or molecular coordinate file for each structure. Then, based on the density of an SiO_2 **FAU** variant of 1.327 g mL^{-1}, the volumetric $SPD_{cell,vol}$ was converted to a gravimetric quantity, SPD_{cell}, in units of g_{ZTC} $g^{-1}{}_{SiO_2}$. Values for SPD_{cell} and $SPD_{cell,vol}$ of all ZTC atomistic models include contributions from all atoms in the unit cell of that model.

4.2.4 Model Visualization

In this work, all atomistic images were generated using CrystalMaker v. 9.2.9.[126] Ring sizes are highlighted by color. Five-, six-, seven-, eight-, and nine-membered rings are highlighted in pink, orange, yellow, green, and blue, respectively.

4.3 Zeolite-Templated Carbon Models

4.3.1 Roussel Model

The first atomistic model of **FAU**-ZTC was reported in 2006[127] and further described in 2007,[99] with the objective of corroborating experimental N_2 adsorption isotherms. This pure carbon model (Figure 4.1), referred to herein as the Roussel Model, was created using a series of grand canonical Monte Carlo (GCMC) simulations, where C–C interactions were modeled using the tight binding and reactive bond order (REBO) formalisms. Starting with a unit cell of pure SiO_2 **FAU**, C_2 dimers were introduced into the pore space and allowed to interact with the template using the PN-TrAZ potential function. The resulting structure,

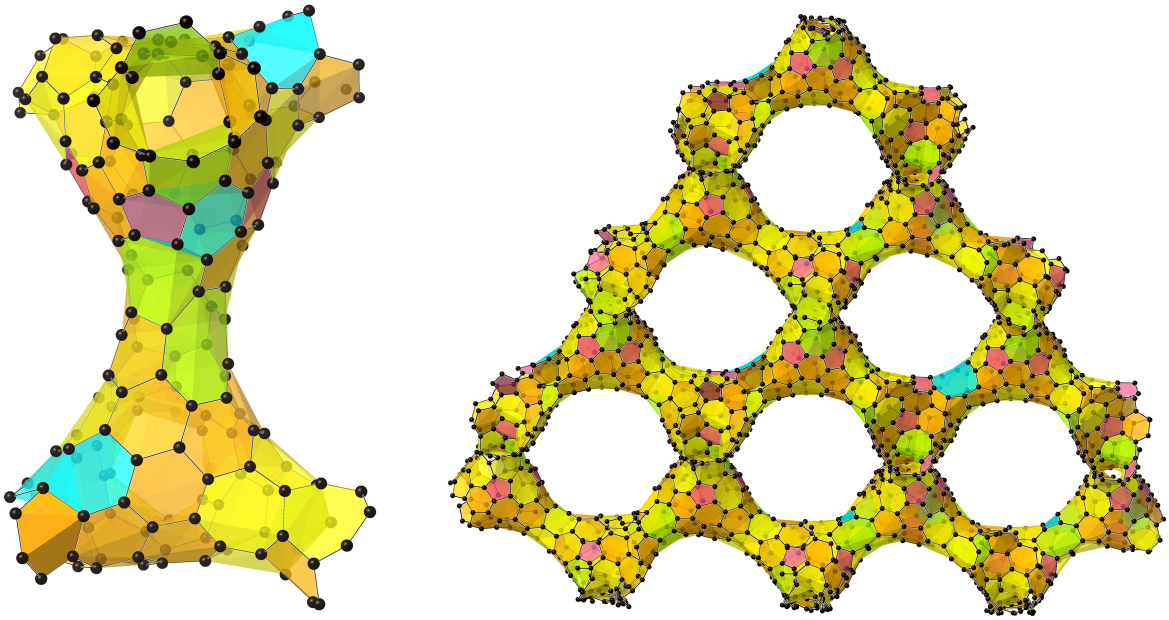

Figure 4.1: Roussel Model: (left) a two-cell closed-tube subunit and (right) an extended multicell structure.

determined to contain exclusively sp^2-hybridized carbon, is categorized as a closed-tube model (shown in Figure 4.1). The calculated surface area of this model is 1940 m^2 g^{-1}, lower than high-quality ZTCs synthesized by 2001–2002.[31,93] Owing to its relatively small size (corresponding to a single unit cell of the zeolite template), the simulated XRD pattern of the Roussel Model (shown in Figure 4.11) indicates a structure with both atom-to-atom and pore-to-pore long-range order. The SPD_{cell} of the Roussel Model, calculated retrospectively for the purposes of this review, is found to be 0.62 (see Table 4.1), roughly twice that of archetypical **FAU**-ZTC (an experimental feature of ZTCs that had been established by 2002[93]).

4.3.2 Nishihara Model I

In 2009, Nishihara and coworkers reported several atomistic models of ZTC in order to reconcile the low SPD experimentally observed in **FAU**-ZTC.[102] Using Chem3D Ultra software, a carbon framework limited to five-, six-, and seven-membered rings was first simulated within the pore space of a rigid **FAU** template. The resulting structure was then geometrically optimized using semiempirical methods (MOPAC PM5 with the linear-scaling algorithm MOZYME). In all cases explored, forcing the deposited carbon to connect

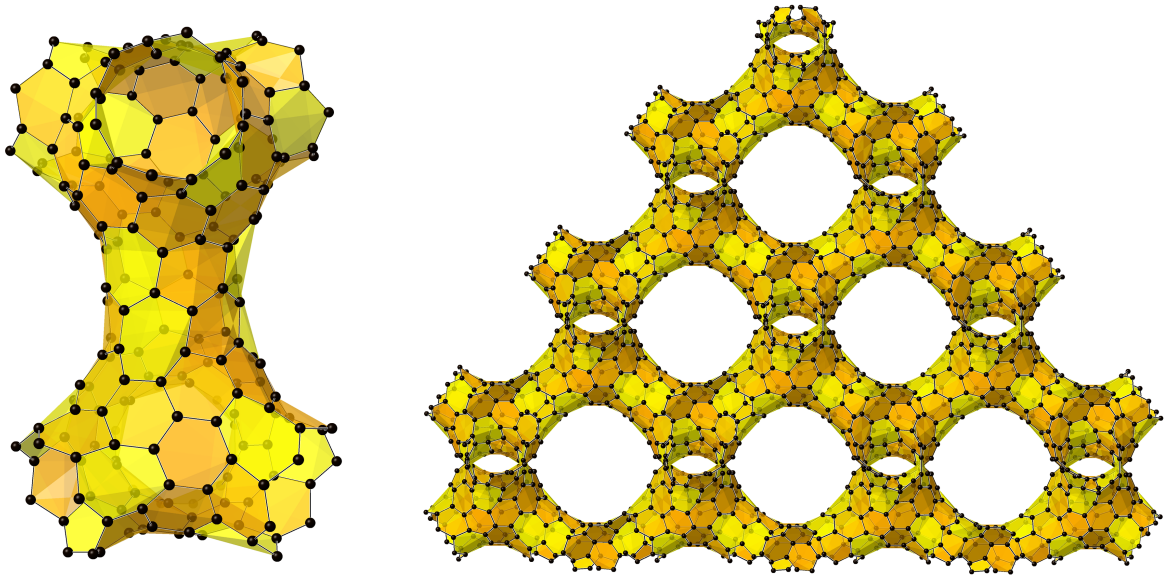

Figure 4.2: Nishihara Model 0a: (left) a two-cell closed-tube subunit and (right) an extended multicell structure with six- and seven-membered rings highlighted in orange and yellow, respectively.

through all four entrances of the **FAU** supercage (Figure 4.2 and 4.3) resulted in SPD_{cell} much larger than experimentally accessible materials: 0.77 and 0.45, respectively. To reduce the density of carbon necessary to construct a three-dimensionally connected framework, a positively curved, fullerene-like fragment was designed and oriented within the zeolite

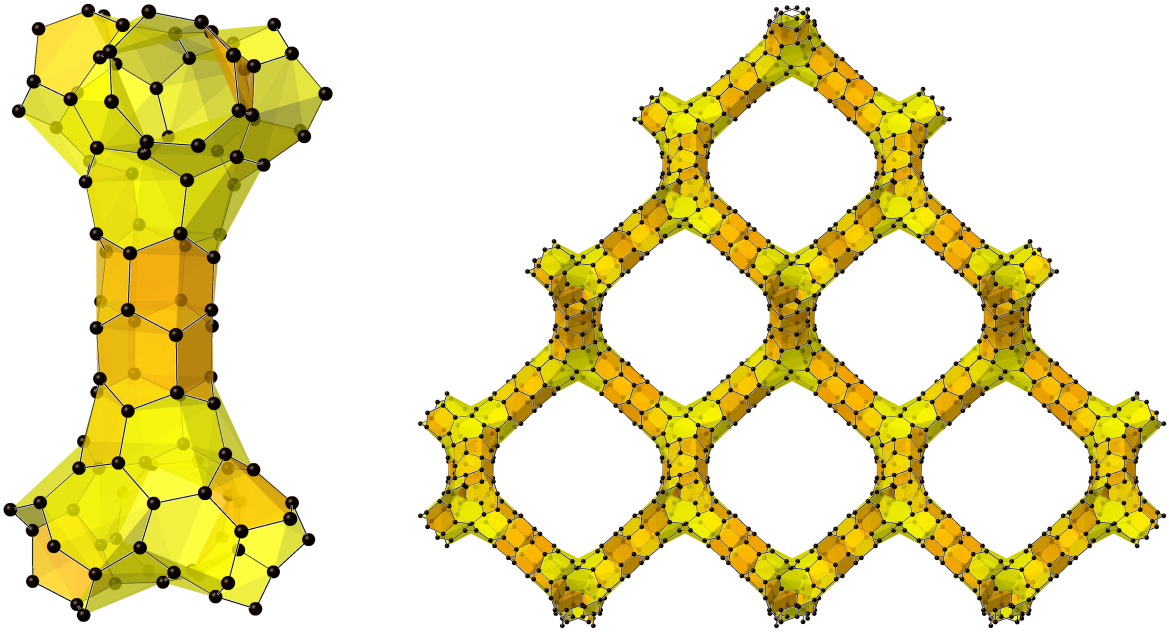

Figure 4.3: Nishihara Model 0b: (left) a two-cell closed-tube subunit and (right) an extended multicell structure with six- and seven-membered rings highlighted in orange and yellow, respectively.

template, allowing the carbon to connect through only three out of the four entrances in each zeolite supercage. The resulting model, referred to as Nishihara Model I and shown in Figure 4.4, resembles a connected "buckybowl" network and is classified as an open-blade structure. Despite initially being allowed to contain seven-membered carbon rings, the relaxed structure only consists of five- and six-membered rings and exhibits an SPD_{cell} of 0.32, which closely resembles that of archetypical **FAU**-ZTC. However, once again, the small unit cell (and hence high atomic regularity) of Nishihara Model I results in a highly ordered simulated XRD pattern (Figure 4.11). Due to its open-blade nature with an abundance of edge sites, Nishihara Model I exhibits a calculated surface area of 4980 m^2 g^{-1}, which is much higher than what has been observed experimentally. The idealized variant of Nishihara Model I (shown in Figure 4.4) has a chemical composition of $C_{80.0}H_{20.0}$ while

a more realistic variant includes a variety of oxygen-bearing functionalities consistent with experimental measurements and exhibits a chemical composition of $C_{78.4}H_{15.7}O_{5.9}$.

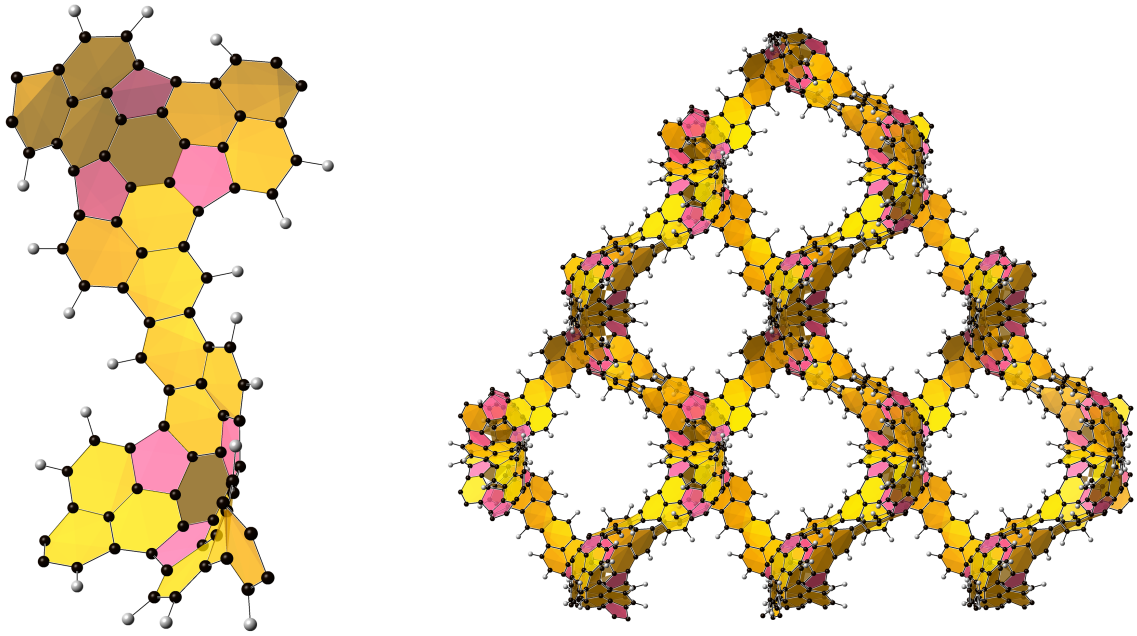

Figure 4.4: Nishihara Model I: (left) a two-cell open-blade subunit and (right) an extended multicell structure including hydrogen (white).

4.3.3 Nueangnoraj Model

A new type of CVD procedure, termed pulsed chemical vapor deposition (P-CVD), was reported by Nueangnoraj et al. to achieve a core-shell ZTC structure with a core SPD_{cell} higher than archetypical **FAU**-ZTC.[72] The "over-templated" variant of **FAU**-ZTC is referred to as "P7". Owing to newly acquired evidence of higher carbon packing density within the core of an "over-templated" variant of **FAU**-ZTC, Nueangnoraj and coworkers developed a new high-SPD molecular model by employing similar methods to those used for Nishihara Model I: construction of a carbon network using Chem3D Ultra software followed by semiempirical geometrical relaxations (MOPAC PM5 with the linear-scaling algorithm MOZYME). The carbon network was permitted to have a higher density of

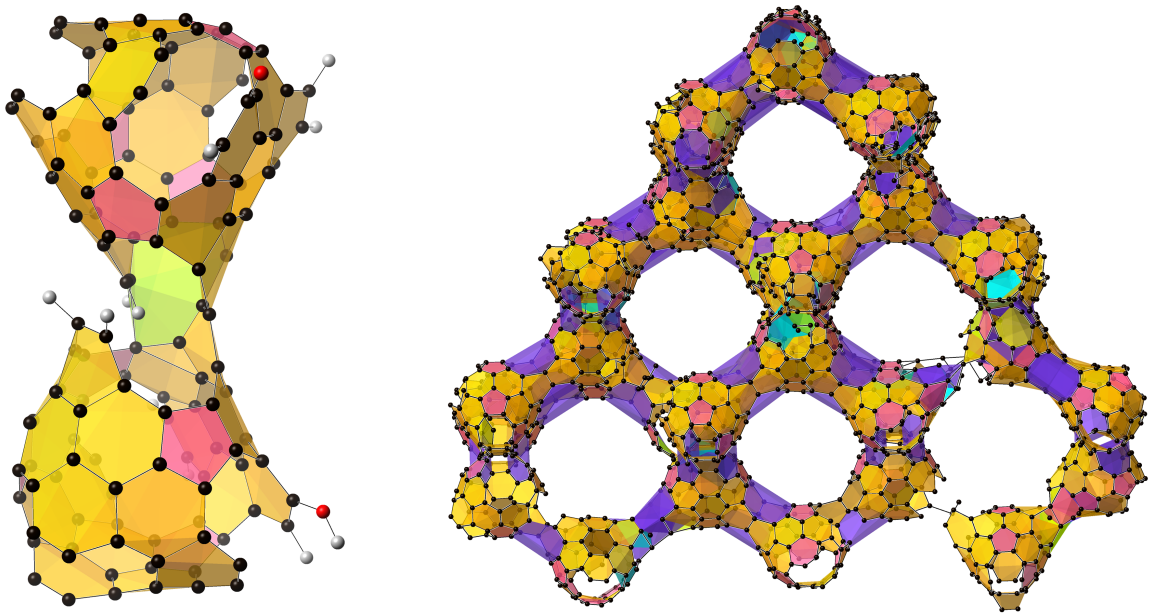

Figure 4.5: Nueangnoraj Model: (left) a two-cell open-blade subunit including hydrogen (white) and oxygen (red) and (right) an extended multicell structure.

carbon resulting closed-tube structure type. A simpler variant of the Nueangnoraj Model was constructed entirely out of carbon while a more complex variant includes some oxygen-bearing functionalities consistent with experimental measurements and exhibits a chemical composition of $C_{91.2}H_{7.5}O_{1.3}$ (as shown in Figure 4.5). A periodic structure was not developed in this work, and therefore further analysis of the Nueangnoraj Model could not be included within this review.

4.3.4 Kim Model

After templating a lanthanum-exchanged **FAU** template, Kim et al. utilized single crystal XRD of the zeolite-ZTC composite to obtain the Kim Model, as shown in Figure 4.6.[46] This model is different from previous models since it represents the measured average positions of carbon atoms in **FAU**-ZTC. XRD was performed on a single particle

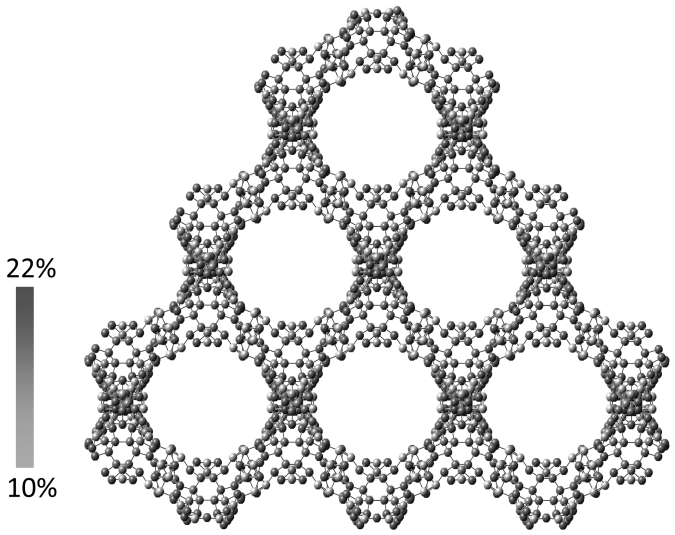

Figure 4.6: Kim Model: an extended multicell structure with partial occupancy ranging from 22% (dark gray) to 10% (light gray).

of ZTC (still captive inside the zeolite template), which was used to deduce an electron density map of the ZTC structure. The resulting atomistic model is therefore the product of experimental results (as opposed to the previous purely theoretical models) and represents the average structure over an entire particle of ZTC, while still captive within the zeolite template. While the overall carbon packing density of this model is low ($\mathrm{SPD}_{\mathrm{cell}} = 0.21$), the total number of carbon lattice sites is extremely high (corresponding to an $\mathrm{SPD}_{\mathrm{cell}}$ of 1.23 if every site were to be fully occupied). This is possible because the probability of occupation of each site is significantly lower than unity (varying between 10% and 22%). For this reason, the Kim Model is difficult to directly compare to the previous purely theoretical models. The Kim Model is a tetrahedrally coordinated (in terms of channel to channel connectivity), dense amorphous network consisting only of carbon, as shown in Figure 4.6, and therefore resembles a closed-tube structure at first view. However, the low occupancy of carbon at each lattice

site combined with the requirement of carbon connectivity in the resulting ZTC indicates that the Kim Model is likely to be an open-blade structure in actuality. Unfortunately, a reasonable standalone structure that remained connected in three-dimensions based on these measured site occupancies could not be conceived, making a fair comparison of this model's properties a challenge. The simulated XRD pattern (even when accounting for partial occupancy of each lattice site) shows several significant reflections above 11° (see Figure 4.11). Surface area calculations were performed for the purposes of this review on both the fully occupied and partially occupied versions of the Kim Model, resulting in surface areas of 790 and 6050 m^2 g^{-1}, respectively. The fully occupied model exhibits a very low surface area owing to the high carbon density; the partially occupied model, on the other hand, exhibits a much larger surface area due to the inherent introduction of large voids between the carbon atoms and the disconnected nature of the framework.

4.3.5 Nishihara Model II

In 2018, it was confirmed by neutron total scattering measurements that ZTCs contain up to at least seven-membered rings, with possible higher ring sizes.[128] To improve on past work and ensure larger rings were represented in the atomistic model of **FAU**-ZTC, Nishihara et al. developed the large (comprising a 2×2×2 native **FAU** supercell), open-blade Nishihara Model II. As noted above, in Nishihara Model I, sp^2-hybridized carbon rings including pentagons, hexagons, and heptagons were initially allowed, although the final structure included only pentagons and hexagons. While Nishihara Model I represented a reasonable local structure of **FAU**-ZTC, the model could not accurately capture the disordered nature of the extended structure (as evidenced by the largely featureless experimental XRD pattern of ZTC). In addition, neutron total scattering measurements confirmed the presence of larger carbon ring types (up to at least 7-membered rings), a further motivation for the development of Nishihara Model II. The updated model comprises

significantly more atom-to-atom disorder while maintaining the long-range pore-to-pore order that is characteristic of ZTC, by comprising more unit cells of the zeolite template (a 2×2×2 supercell). The simulated XRD pattern reflects this reduced overall crystalline order, as shown in Figure 4.11, having no significant features above 11°. Nishihara Model II, similarly to Nishihara Model I, exhibits a high surface area of 4590 m^2 g^{-1}. Lastly, while Nishihara Model I and Nishihara Model II are very different in terms of overall atom-to-atom order and presence of carbon rings larger than hexagons, the carbon packing densities are similar and roughly consistent with experimental results: SPD_{cell} = 0.33 for Nishihara Model II. The model contains only carbon and hydrogen, lending a chemical composition of $C_{72.4}H_{27.6}$. A more complex variant of Nishihara Model II, herein referred to as Nishihara Model II+, was later reported in 2019,[78] containing oxygen-bearing functionalities and exhibiting a chemical composition of $C_{71.2}H_{23.8}O_{5.0}$ (see Figure 4.7).

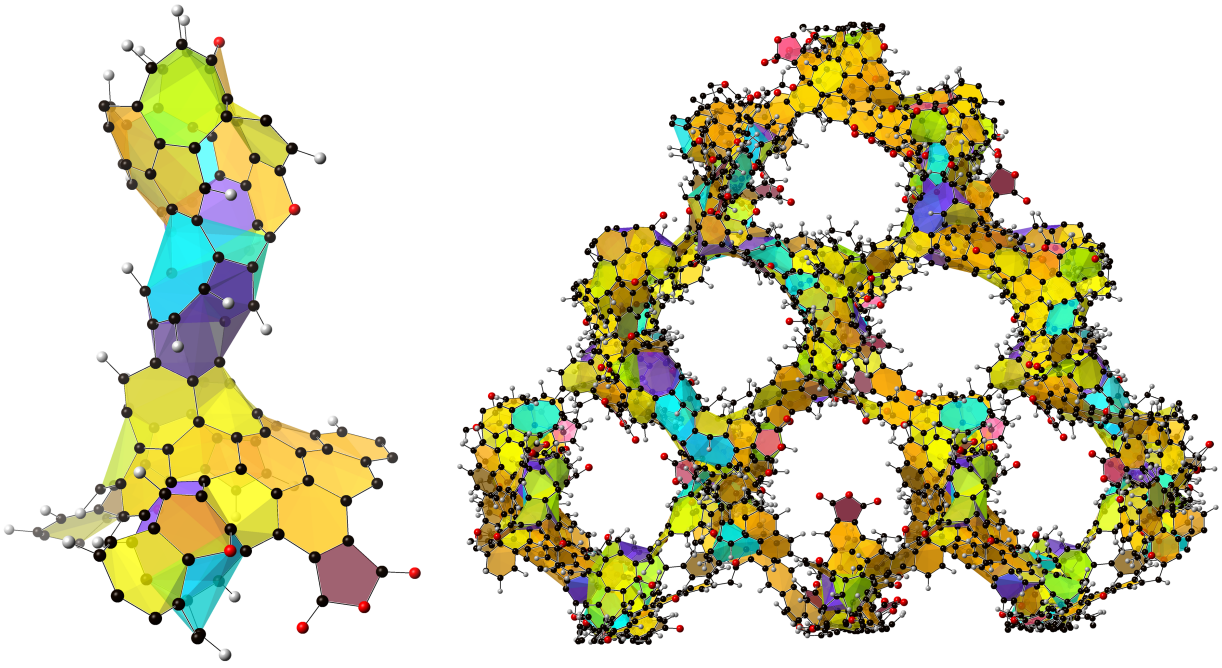

Figure 4.7: Nishihara Model II+: (left) a two-cell open-blade subunit and (right) an extended multicell structure including hydrogen (white) and oxygen (red).

4.3.6 Braun Model

In 2018, an extensive library of ZTC atomistic models was reported by Braun et al., developed using every candidate zeolite template that could host a three-connected carbon structure and carried out with high-level computational methods.[33] This work demonstrates the impressive power of computational methods in the structural modeling of complex materials (over 200 candidate ZTC variants were assessed). Beginning with all known zeolite structures, as approved by the IZA,[32] Braun et al. created a library of all stable triply periodic pure-carbon ZTC structures that could theoretically be synthesized. Zeolites with any pore entrances smaller than 4.8 Å were eliminated on the basis of inaccessibility, and ZTC structures were then formed in the zeolite pores using a custom Monte Carlo (MC) algorithm and relaxed using high-level density functional theory (DFT) methods (DFT-D3 with PBE density functional). The resulting structures were found to be highly stable, even upon annealing up to 1000 K. Fourteen of the proposed ZTC models, including 10 such materials in templates that have not yet been explored experimentally, resemble TPMSs and are schwarzite-like models. Two models in particular, referred to as Braun Model NR and Braun Model R (Figure 4.8), correspond to **FAU**-ZTC structures before and after structural relaxation, respectively. Both structures are closed-tube type models with high regularity and structural packing densities ($SPD_{cell} = 0.71$ and 0.68, respectively). A significant result of this work is that at least 14 schwarzite-like materials were shown to be obtainable within the pores of known zeolite templates.

Primary atomistic models were first achieved using an MC algorithm, distinct from previous methods in that carbon addition was only permitted at the zeolite template's surface. The zeolite template was then removed, producing highly regular nonrelaxed models (e.g., the so-obtained **FAU**-ZTC model, referred to herein as Braun Model NR). Upon relaxation by DFT methods, the relaxed models are highly regular carbon networks owing the original restriction of carbon binding directly at the surface of the zeolite templates. The

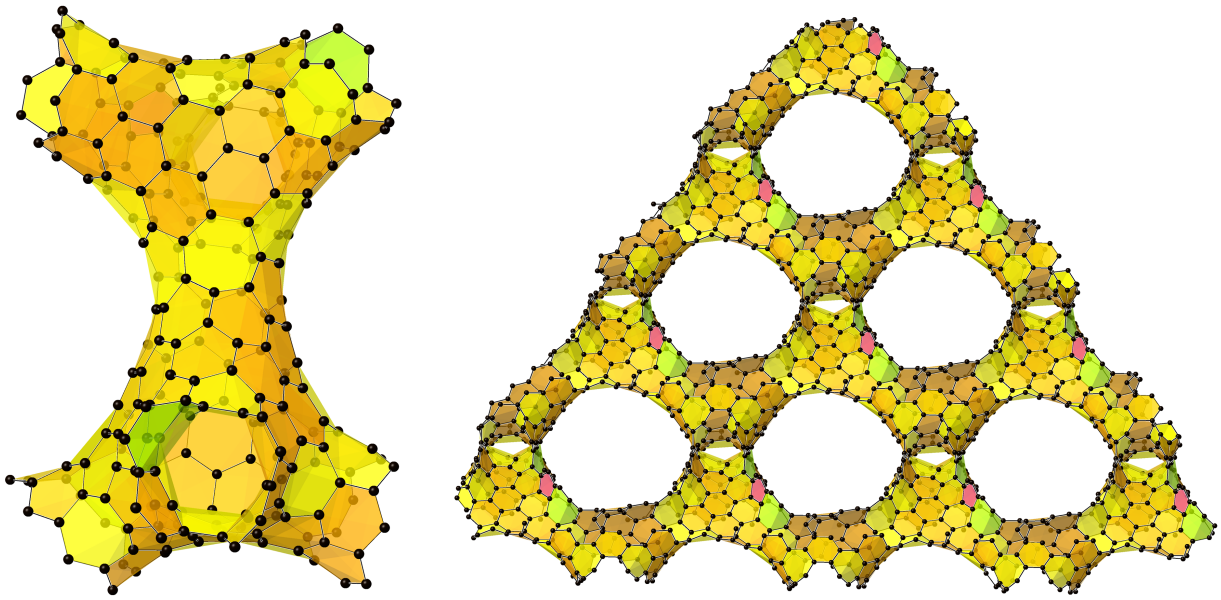

Figure 4.8: Braun Model R: an extended multicell structure.

relaxed **FAU**-ZTC variant, Braun Model R, is a tetrahedrally coordinated schwarzite-like network lying on a surface that resembles non-balanced Schwarz D-surface, and is classified herein as a closed-tube model. Due to the closed-tube nature of this model, the calculated surface area are close to that of one side of a graphene sheet: 1600 m^2 g^{-1}. Lastly, the chemical composition of the Braun Model is purely carbon (no hydrogen or oxygen were considered or would be possible based on the requirement of fully saturated sp^2-hybridized carbon networks inherent to their method).

4.3.7 Tanaka Model IV

Later in 2018, a collaborative effort between Tanaka and Nishihara resulted in a new **FAU**-ZTC model based on similar principles as those used to develop Nishihara Model II, referred to herein as Tanaka Model IV.[34] While Nishihara Model II is more disordered than Nishihara Model I, it was still recognized to exhibit more order and a more regular PSD

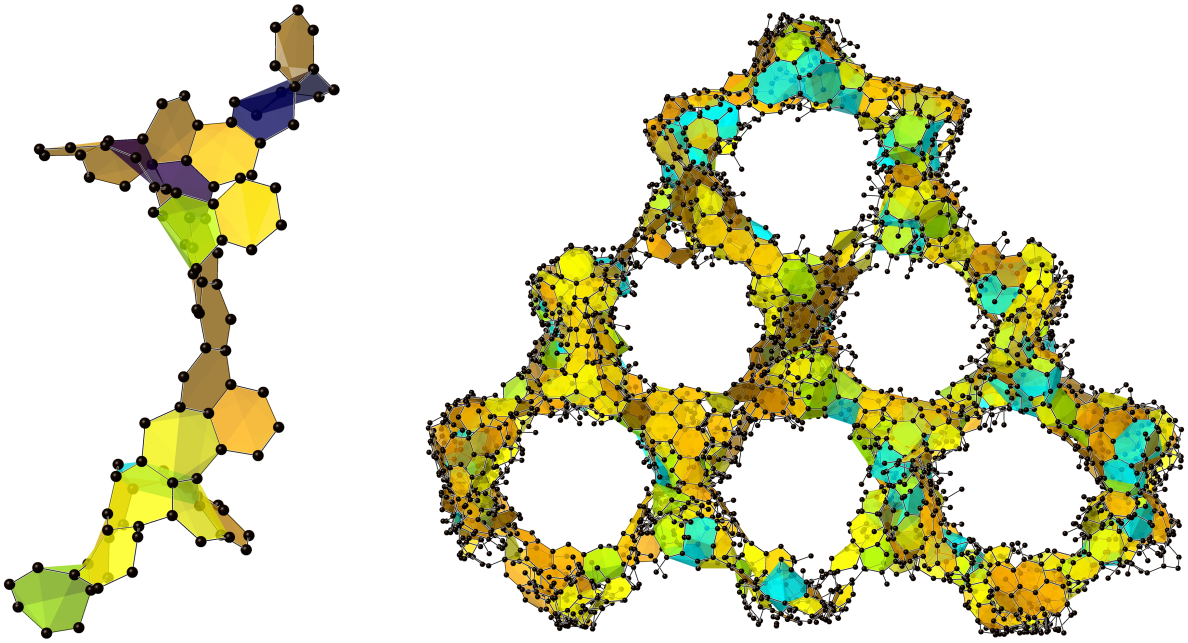

Figure 4.9: Tanaka Model IV: (left) a two-cell open-blade subunit and (right) an extended multicell structure.

than experimental ZTCs. This model was developed using reactive molecular dynamics enforcing a reaction state summation potential to model carbon–carbon interactions. After impregnation of the zeolite template at 1000 K and a quenching step down to 300 K, the zeolite template was removed (leading to an intermediate structure referred to as Tanaka Model III). To introduce further disorder (especially to account for the small but important pore size disorder of archetypical **FAU**-ZTC) the density of carbon was varied throughout the zeolite template to allow for the formation of larger micropores. Many different unit cells were constructed using a range of carbon packing densities from 15 to 55 atoms nm^{-3} (SPD_{cell} = 0.30-1.10). A random set of 27 cells of varying densities (each corresponding to a single **FAU** template unit cell) was used to create a 3×3×3 supercell, Tanaka Model IV, as shown in Figure 4.9. Methylene-type carbons were not restricted in this case. The simulated XRD pattern (see Figure 4.11) exhibits only three distinct peaks

(the 111, 220, and 311 reflections of the faujasite template) and only one minor reflection above 11°. Characteristic of the open-blade models, Tanaka Model IV exhibits a surface area of 3950 m^2 g^{-1}. The average carbon packing density of Tanaka Model IV corresponds to a SPD_{cell} of 0.36, slightly higher than Nishihara Models I and II. Sixteen other ZTCs (based on other viable zeolite templates) were also modeled by Tanaka et al. using similar methods.

4.3.8 Boonyoung Model

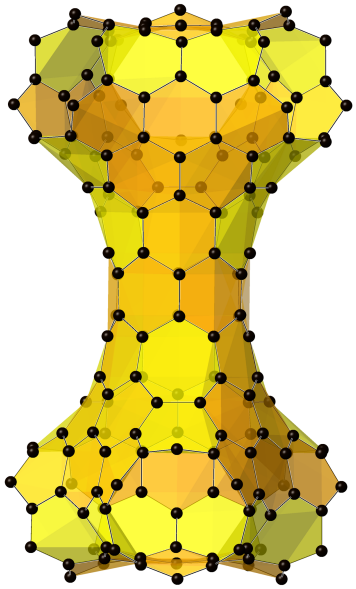

Figure 4.10: Boonyoung Model: tetrahedrally-coordinated "closed-tube" subunit with six- and seven-membered rings highlighted in orange and yellow, respectively.

In an attempt to alleviate the issue of heterogeneous carbon deposition within the zeolite template during ZTC synthesis, Boonyoung et al. reported the effort to template a nanosized **FAU** zeolite template in 2019.[77] Similar to earlier work by Nueangnoraj et al.,[72] this resulted in a core-shell ZTC structure, albeit with a higher SPD_{cell} in the core of each particle. Nevertheless, the highest experimentally observed SPD_{cell} of 0.63 (corresponding only to the core framework of each particle) was reported. A nonperiodic, closed-tube structure was developed using a combination of Avogadro and Chem3D 17.1 to model the

core part of these materials (Figure 4.10); unfortunately, due to the non-periodic nature of the Boonyoung Model, further characterization could not be performed in this review.

4.4 Analysis of Zeolite-Templated Carbon Models

Table 4.1: Experimental and Theoretical **FAU**-ZTC Structural Packing Densities

Model/Material	Precursor	SPD_{exp} $g_{ZTC}\ g^{-1}_{zeolite}$	SPD_{cell} $g_{ZTC}\ g^{-1}_{SiO_2}$	$SPD_{cell,vol}$ $g_{ZTC}\ mL^{-1}$
Roussel Model[127]	theoretical	-	0.62	0.82
Nishihara Model 0a[102]	theoretical	-	0.77	1.02
Nishihara Model 0b[102]	theoretical	-	0.45	0.59
Nishihara Model I[a 102]	theoretical	-	0.32	0.42
Nueangnoraj Model[72]	theoretical	-	0.54	0.72
Kim Model[b 46]	theoretical	-	0.21	0.28
Nishihara Model II[a 128]	theoretical	-	0.33	0.43
Braun Model R[33]	theoretical	-	0.68	0.91
Tanaka Model IV[34]	theoretical	-	0.36	0.47
P-CVD **FAU**-ZTC[c 72]	acetylene	0.54	0.55	0.73
LaY **FAU**-ZTC[46]	ethylene	0.32	0.42	0.56
ZTC40-15-6[c 77]	acetylene	0.60	0.63	0.76
Archetypical **FAU**-ZTC[102]	furfuryl alcohol and propylene	0.29	0.32	0.42
Archetypical **FAU**-ZTC[d]	furfuryl alcohol and propylene	0.35	0.40	0.53

[a] Hydrogen included.

[b] Partial occupation of lattice sites.

[c] Inner-particle structure, corrected for external carbon deposition.

[d] This work.

Structurally, the proposed atomistic models for **FAU**-ZTC can be divided into two categories: (a) having two-sided, ribbon-like "open-blade" connectors or (b) "closed-tube" connectors. In general, the latter (closed-tube) models exhibit lower surface area and higher

SPD, and the open-blade models exhibit higher surface area and lower SPD. The models therefore vary significantly in their resemblance to experimental features of laboratory-synthesized ZTCs. Archetypical **FAU**-ZTC remains the standard ZTC that is synthesized in the laboratory without the accumulation of graphitic material on the ZTC surface.

Table 4.2: Experimental (BET) and Theoretical Surface Areas of **FAU**-ZTC

Model/Material	Surface Area (m^2 g^{-1})	Percent Difference Compared to Archetypical **FAU**-ZTC
Roussel Model[127]	1940	-45%
Nishihara Model 0a[102]	1500	-57%
Nishihara Model 0b[102]	2670	-24%
Nishihara Model I[102]	4980	+42%
Kim Model[a][46]	790...6050	-77...+73%
Nishihara Model II[128]	4590	+31%
Braun Model R[33]	1600	-54%
Tanaka Model IV[34]	3950	+13%
"P7" Core-Shell **FAU**-ZTC[72]	1950	-
Archeypical **FAU**-ZTC[31]	4100	-
Archeypical **FAU**-ZTC[105]	3600	-
Archeypical **FAU**-ZTC[129]	3700	-
Archeypical **FAU**-ZTC[b]	3500	-

[a]Depending on occupation of lattice sites.

[b]This work.

The earliest atomistic model of ZTC (the Roussel Model) is a simple, pure carbon model that was designed for and succeeded at reproducing the primary features of the

experimental PSD of **FAU**-ZTC as measured by N_2 adsorption at 77 K.[127] When comparing their experimental and simulated nitrogen adsorption data, it was concluded that experimental ZTCs must contain more defects than what their model indicated, although both experimental and theoretical results indicate the presence of micropores between 1.1 and 1.2 nm. This model also failed to acknowledge the chemical composition (including a significant quantity of hydrogen and oxygen) and the actual SPD of experimental ZTCs. As a result, the SPD of the Roussel Model is significantly larger than that of archetypical **FAU**-ZTC.

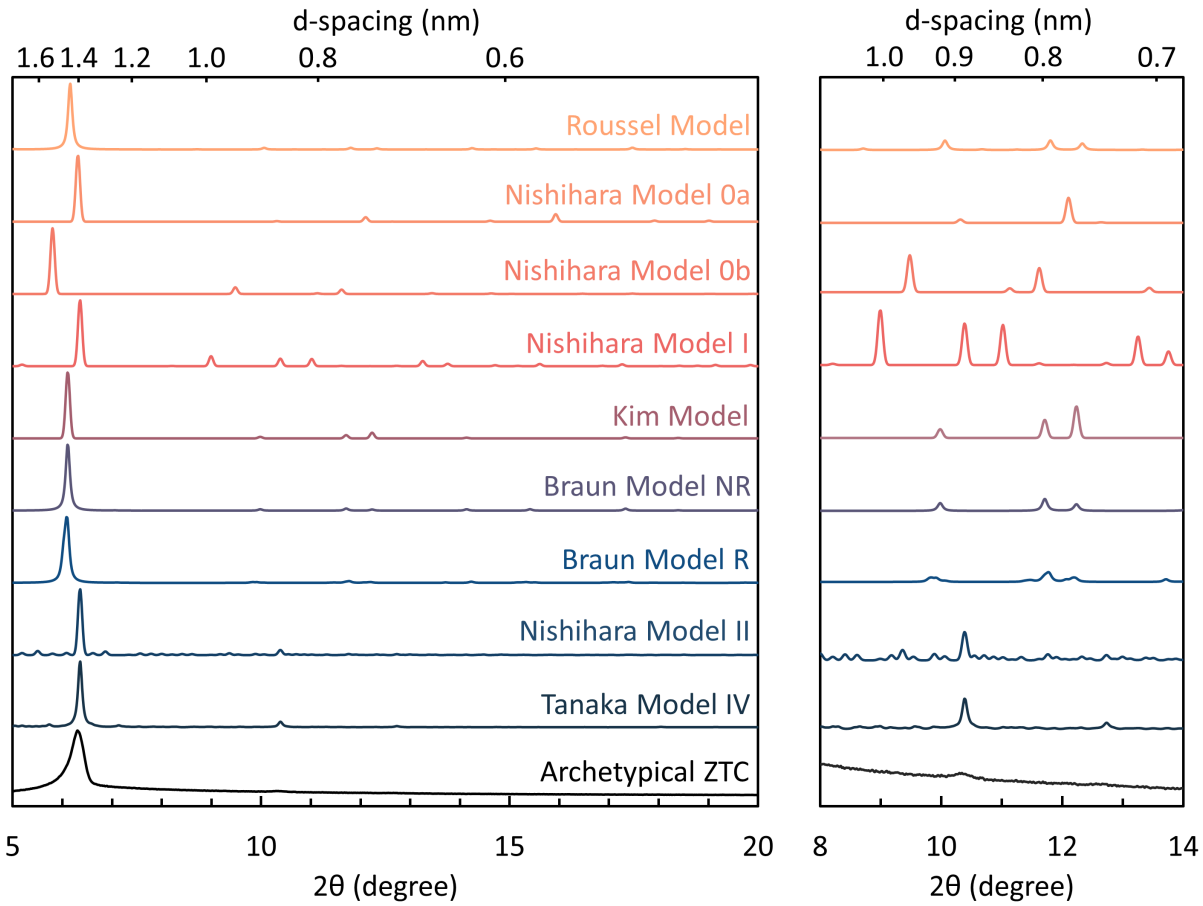

Figure 4.11: Simulated XRD patterns of the **FAU**-ZTC models and a typical set of experimental data for archetypical **FAU**-ZTC, showing (left) the intense (111) reflection at $2\theta = 6.3°$, and (right) the weak (220) reflection at $2\theta = 10.4°$ (for Cu Kα X-rays).

The three models reported by Nishihara and coworkers in 2009 show that closed-tube models (e.g., Nishihara Model 0a and Nishihara Model 0b) have a lower surface area and higher SPD than typical experimental ZTCs. This observation led to the development of the first open-blade model (Nishihara Model I) which exhibits both a larger surface area and a lower SPD; connectivity through only three of four zeolite cage entrances allowed a slight reduction of the SPD while increasing the surface area. Lastly, a more complex variant of Nishihara Model I was the first atomistic model to acknowledge the true chemical composition of ZTC, which is typically measured to be $C_{75.3}H_{19.0}O_{5.7}$. The true composition of ZTC is an important indicator that experimentally obtained ZTCs are certainly not equivalent to carbon schwarzites. In fact, ZTCs have significantly more edge character than activated carbons, lending ZTCs very unique characteristics in electrochemical applications.[28,130] The calculated surface area of Nishihara Model I (see Table 4.2) is significantly larger (by ∼42%) than the experimentally estimated surface area of archetypical **FAU**-ZTC (where N_2 uptake is modeled using the BET equation for multilayer adsorption).

As was demonstrated by Nueangnoraj and coworkers in 2013 and 2019, judicious modifications to the synthetic procedure can be used to increase SPD of ZTCs, though always at the cost of graphitic carbon accumulation at the particle surface. The experimental materials generated in their work exhibit the highest SPD values reported to date (when the external carbon shell has been excluded), and the inner structure is proposed to be of closed-tube type. This is also consistent with the lower measured surface areas of the corresponding experimental ZTCs (referred to as "P7" [72] and "ZTC40-15-6" [77]). Nevertheless, the hydrogen and oxygen content of these high SPD variants of **FAU**-ZTC remain significant: e.g., 0.6 and 2.4 wt % (i.e., $C_{91.2}H_{7.1}O_{1.7}$), respectively, for "P7".

The, tetrahedrally coordinated model proposed by Kim and coworkers based on single-crystal X-ray diffraction measurements failed to result in a connectable framework

when atom occupancies were considered. The reported model chemical formula of $C_{207.58}La_{23.52}Na_{14.27}O_{26.69}[TO_2]_{192}$ (T = Si or Al) would result in a $SPD_{cell} = 0.22$, which does not allow for a connected carbon framework. On the other hand, the packing density is much larger than the experimental SPD when all carbon atoms present in the crystallographic information file are considered as fully occupied lattice sites ($SPD_{cell} = 1.44$). This structure, as shown in Figure 4.6 except with all sites occupied, is clearly not a permissible representation of ZTC as it includes an unphysically large number of carbons in very close proximity. Simulated XRD powder patterns of the Kim Model (as obtained herein) show a primary peak at 6.2° (lower than that of archetypical ZTC but consistent with other zeolite-carbon composites before HF dissolution) as well as high short-range ordering due to the large number of lattice sites. However, it should be emphasized that the Kim Model is based on experimentally collected XRD measurements and therefore represents the true (average) electron density of ZTC prior to being freed from the zeolite template.

Many of the schwarzite-like structures reported by Braun and coworkers in 2018 represent a physical limit of carbon packing within a zeolite template; they exhibit extremely high SPD while requiring the carbon to be located at the surface of the original zeolite template. Despite several claims of the authors otherwise, these models should not be considered to represent actual ZTCs synthesized in the laboratory. Furthermore, the Braun structures (which are indeed pure carbon schwarzite-like materials) are not consistent with the actual chemical composition of ZTCs.

On the other hand, by using a semiempirical modeling procedure, Tanaka and coworkers were able to create a similar library of possible ZTCs while still reproducing the experimental XRD pattern, surface area, and SPD of experimental **FAU**-ZTC. A significant shortcoming of all of the proposed models of **FAU**-ZTC, with the possible exception of Tanaka Model IV, lies in their high short-range structural order, as shown in Figure 4.11. All proposed models inherently exhibit "perfect" atomic ordering by their description using a periodic unit cell.

This is more pronounced for models with smaller unit cells, demonstrated by the presence of sharp reflections in the XRD pattern at angles between 13˚and 20˚ that are inconsistent with experimental ZTCs. Therefore, the best model of **FAU**-ZTC is one that is large enough to contain significantly different regions of connectivity within the overall ZTC framework. While cumbersome in its extremely large size, the 3×3×3 supercell of Tanaka Model IV seems to be large enough to accurately describe most of the disorder inherent to experimental ZTCs.

The model described by Tanaka and coworkers in 2018 represents the most consistent fit to all of the experimental properties of archetypical **FAU**-ZTC (synthesized by the well-established two-step method). The predicted geometrical surface area is the closest to the experimentally measured surface area of 3950 m^2 g^{-1}. The SPD is equivalent to that of experimental samples to within the error of TGA experiments. By introducing local disorder into the atomistic model, all higher angle diffraction peaks in the predicted XRD pattern are observed to significantly diminish, while the long-range pore-to-pore ordering is maintained (as evidenced by the intense (111) reflection). This effect is aided by the very large unit cell of the Tanaka Model, corresponding to 27 unit cells of the original **FAU** template and a total of 8935 carbon atoms; such a large repeating unit lends much more possibility for disorder than is possible within a single-cell model such as Nishihara Model I. As for chemical composition, Tanaka Model IV fails to account for the presence of hydrogen and oxygen necessary to be a truly accurate model of ZTC; thus the author suggests further work should be carried out to modify Tanaka Model IV to incorporate hydrogen and oxygen.

4.5 Conclusion

Modeling the structure of porous carbon materials is a complex undertaking, and the metrics of comparison to experimental data are synthesis-specific. Unlike disordered porous carbons[131–134] or mesoporous ordered carbons,[135,136] materials produced by templating within zeolites have a high degree of order at a “molecular” length scale, allowing atomistic

modeling to be more tractable. In the case of ZTCs, experimental results depend on the zeolite template used, the carbon precursor, and the conditions of synthesis, among many other factors. Therefore, it is important to note that the reported models of ZTC should only be compared (to each other and to experimental ZTCs) with caution. All of the models reviewed herein contribute important fundamental insights into the structure of archetypical ZTC and potential future ZTCs. However, a successful model must be reasonably consistent with the available experimental evidence relevant to ZTCs currently synthesized in the laboratory in order to be labeled as such.

The Roussel Model represents a simple but practical first attempt to portray the atomistic structure of **FAU**-ZTC. Since then, Nishihara and coworkers have used more sophisticated methods to build structural models of ZTC that accurately represent the experimental properties of ZTC, both the standard variant and several unusual high SPD core–shell variants. This work showed that both open-blade and closed-tube structure types are likely accessible in the laboratory, but that a significant part of the ZTC structure must be of open-blade type to account for its very high surface area. Recently, Kim and coworkers introduced an interesting structure by direct inference from experimental data collected via single-crystal X-ray diffraction and its associated electron density map. This structure, while experimentally founded, is too sparsely populated with carbon when measured lattice site occupancies are considered (or much too dense when site occupancies are ignored), but perhaps some underlying substructures can be found by a computational approach. The models proposed by Braun and coworkers do not represent an accurate depiction of experimental ZTCs but remain intriguing if they could someday be synthesized. The most recent and promising model, Tanaka Model IV, introduces pore size disorder by varying the carbon density within its large unit cell and most closely aligns with experimental findings. However, its simple chemical composition (as pure carbon) leaves Nishihara Model II+ as the most successful overall model for describing experimental **FAU**-ZTC structure.

There remains further work in improving the atomic-scale description of ZTCs, especially by including hydrogen and oxygen in the composition of Tanaka Model IV. The exploration of wider synthetic conditions may also lead to the discovery of new ZTCs, and modeling the resulting structures should be undertaken with attention to surface area, short-range and long-range order, structural packing density, and chemical composition. We anticipate further complexity arising with the exploration of new zeolite templates and note that accurate atomistic models of **EMT**-ZTC and ***BEA**-ZTC do not yet exist though high-quality experimental materials do. Due to the wide availability of experimentally observable properties and their long-range pore-to-pore ordering yet local disorder, ZTCs will continue to be of high interest as model three-dimensional porous carbon framework materials until true schwarzites can be synthesized.

CHAPTER FIVE

THE ORIGIN OF SPIN POLARIZATION IN POROUS CARBON MATERIALS

Access to an atomistically representative and quantum-chemically refined ZTC model, like Nishihara Model II+, allows for further computational investigation of material properties such as spin polarization (the presence of unpaired electrons) in ZTCs. Classically, sp^2-hybridized carbon materials are predicted to be diamagnetic, meaning there are no unpaired electrons or spins in the material.[137] However, it has also been shown that sp^2-hybridized carbon materials with defects can present as paramagnetic, with unpaired electrons that weakly and temporarily align in a magnetic field.[138] In this chapter, experimental and computational techniques are combined to measure magnetic behavior and identify structural origins of spin polarization in ZTCs.

5.1 Experimental Materials and Measurements

5.1.1 Porous Carbon Materials

For comparison to the standard activated carbons, archetypical ZTC was synthesized by the two-step method. FA impregnation and propylene deposition at 700 °C for 5 h were followed by a 900 °C heat-treatment for 3 h (see Appendix B for full synthetic protocol). The final ZTC material was further degassed at 120 °C for 24 h under oil-free vacuum and stored under argon until further use.

In this work, the magnetic susceptibilities were compared. Firstly, two randomly arranged activated carbons were selected as representative carbonaceous adsorbents with medium to high surface areas: MSP-20 and MSC-30. MSP-20 and MSC-30 were obtained from Kansai Coke & Chemicals Company, Ltd. (Amagaraki, Japan). Both samples were degassed at 120 °C for 24 h under oil-free vacuum prior to use, but otherwise used as provided.

5.1.2 Materials Characterization

5.1.2.1 SEM-EDX To ensure the carbon samples were free from Fe, Co, and Ni which would lead to magnetic signatures, energy-dispersive X-ray (EDX) spectroscopy was performed using a scanning electron microscope (PHI 710 Scanning Auger NanoProbe, Physical Electronics Inc.) under a highly focused electron beam and using a windowless X-ray detector (XFlash 6| 10, Bruker Corp.). Samples were prepared by pressing the native powder into indium foil. No metal content was detected in the porous carbon samples studied in this work.

5.1.2.2 SQUID Measurements Superconducting quantum interference device (SQUID) measurements were performed using a Quantum Design MPMS3 magnetometer between 5 and 300 K in fields up to 6.8 T.

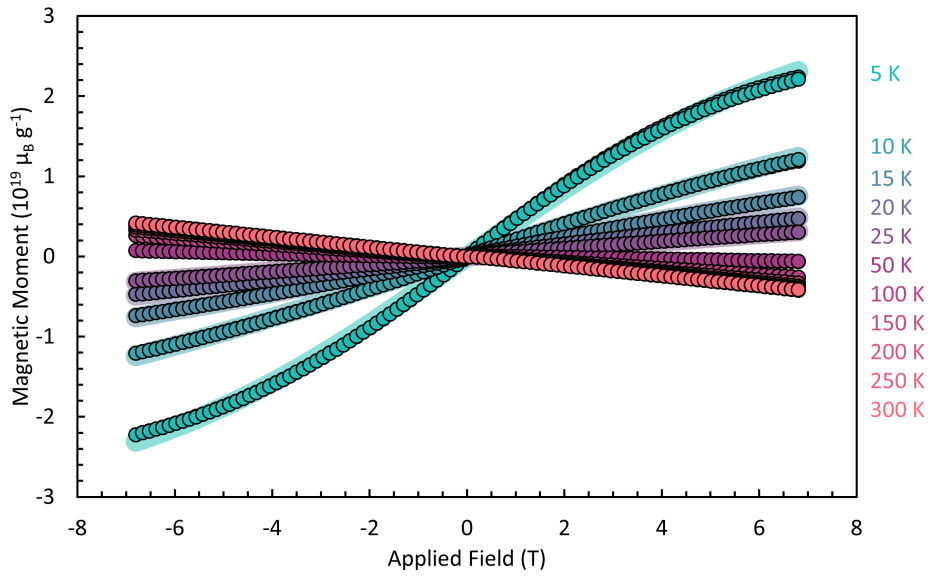

Figure 5.1: Magnetization isotherms of ZTC as a function of applied magnetic field, fitted with the Brillouin equation.

SQUID measurements can be used to quantify the magnetic susceptibility, or the degree of magnetization of a material in response to an applied magnetic field. Therefore,

magnetization curves, as shown in Figures 5.1, 5.2, and 5.3, indicate diamagnetic behavior when the slope of an isotherm is negative, and paramagnetic behavior when the slope of an isotherm is positive. Paramagnetism is detected when an applied external magnetic field induces unpaired electrons in a material to align. However, the strength of paramagnetic susceptibility decreases as the temperature increases, due to thermal fluctuations of the unpaired spins. This results in the detection of paramagnetic behavior (if present) at low temperatures, which transitions to diamagnetic behavior as the temperature increases.

5.1.2.3 SQUID Analysis All SQUID isotherms showing a positive magnetic susceptibility were fit using the paramagnetic Brillouin equation[139]:

$$m = m_{sat}\left(\left(\frac{2J+1}{2J}\right)\coth\left(\frac{x\,(2J+1)}{2J}\right) - \frac{1}{2J}\coth\left(\frac{x}{2J}\right)\right) \tag{5.1}$$

$$x = \frac{J\,B\,g\,\mu_B}{k_B\,T} \tag{5.2}$$

In Equation 5.1, m_{sat}, J, B, g, μ_B, k_B, and T are the saturation magnetization, total angular momentum quantum number ($J = \frac{1}{2}$), applied magnetic field, Landé g-factor ($g = 2$ for an electron), Bohr magneton, Boltzmann constant, and temperature, respectively. First, m_{sat} was determined from each magnetization curve. The positive values of m_{sat} (i.e., the values at all temperatures exhibiting paramagnetism) were then used to determine m_{sat} at 0 K by linear extrapolation, as shown in Figure 5.4.

Interestingly, both ZTC and MSC-30 show paramagnetic behavior at low temperatures, whereas MSP-20 does not. Fitting the paramagnetic magnetization curves using the Brillouin equation (Equation 5.1) allows for the extrapolation of the saturation magnetization (m_{sat}) to 0 K (Figure 5.4), which is a value that can be determined by computational modeling. The extrapolated saturation magnetization at 0 K indicates that ZTCs contain significantly

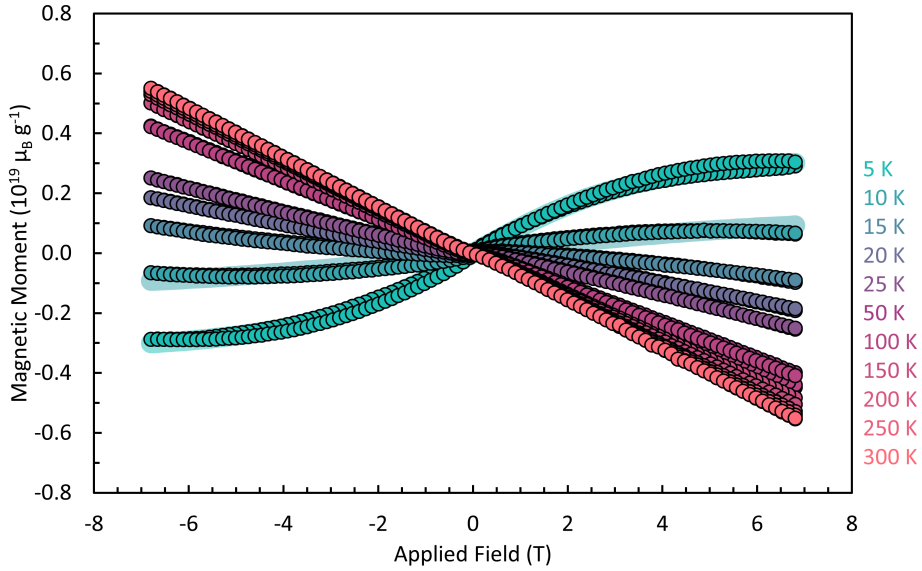

Figure 5.2: Magnetization isotherms of MSC-30 as a function of applied magnetic field, fitted with the Brillouin equation.

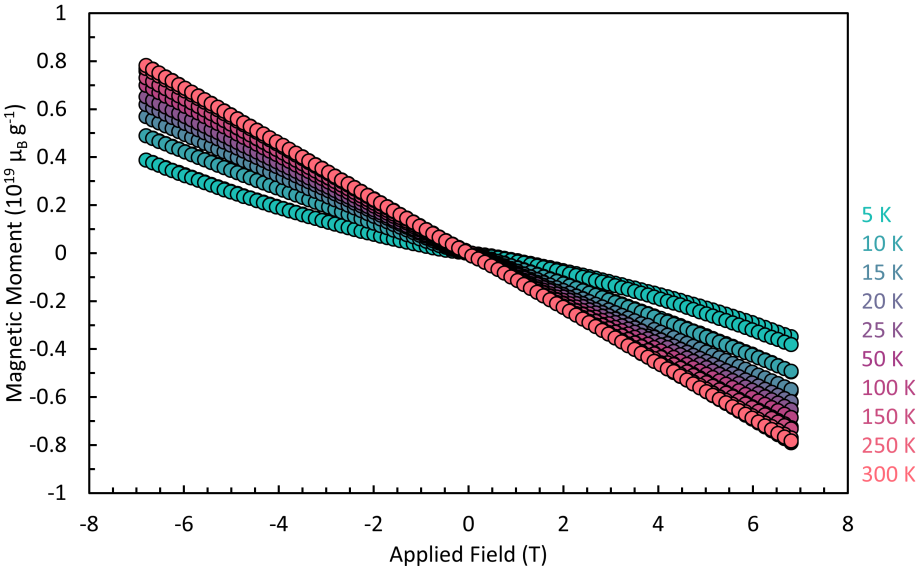

Figure 5.3: Magnetization isotherms of MSP-20 as a function of applied magnetic field.

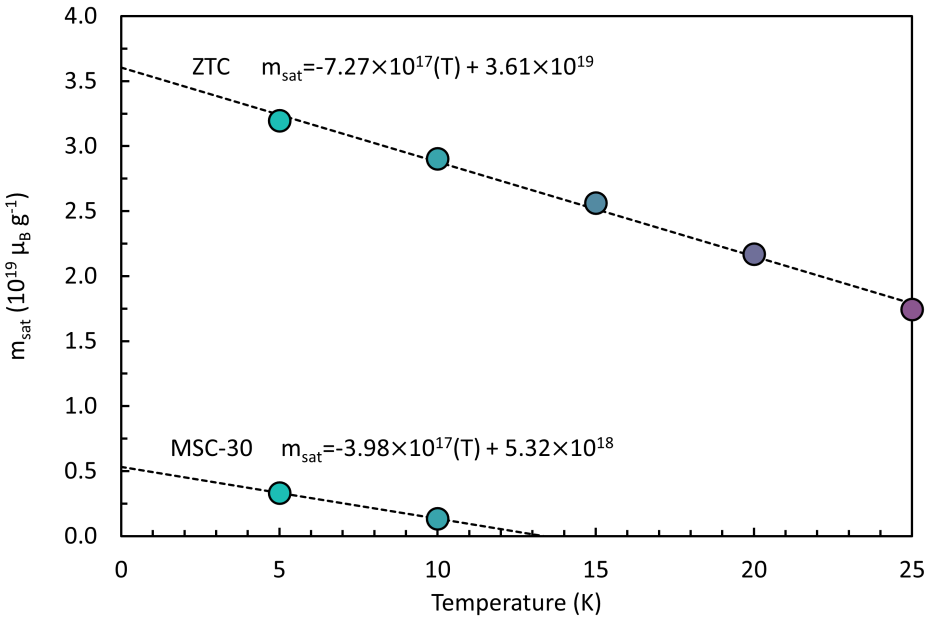

Figure 5.4: Fitted m_{sat} values for all paramagnetic SQUID isotherms, linearly extrapolated to 0 K.

more unpaired electrons than MSP-30. The determined saturation magnetization can be converted to units of unpaired electrons per gram (a conversion factor of 4.615 unpaired electrons per μ_B [140]) resulting in 1.67×10^{20} and 2.46×10^{19} unpaired electrons per gram for ZTC and MSC-30, respectively.

5.2 Spin Polarization in Nishihara Model II+

Prior to this work, no quantum-chemically refined model of ZTC existed for exploration of its expected magnetic properties (especially, the number of unpaired electrons per gram. Therefore, periodic DFTB optimizations were performed on Nishihara Model II+ using the matsci-0-3 parameter set.[141,142] Spin polarization calculations on Nishihara Model II+ were performed by enforcing a set number of unpaired electrons on the structure and then allowing the structure to geometrically optimize. The DFTB optimizations performed on

Nishihara Model II+ (Figure 5.5) indicate that ZTCs are detectably paramagnetic. While Nishihara Model II+ is only a representative model of experimental ZTC ,its magnetic susceptibility is found to have 4.65×10^{20} unpaired electrons per gram, remarkably within the same order of magnitude as determined experimentally using SQUID measurements. Furthermore, when Nishihara Model II+ was also allowed to fully relax from a state enforcing an extremely large number of unpaired spins (6.0×10^{20} unpaired electrons per gram), it minimized its energy by returning to the same spin state as in the above calculations, with 4.65×10^{20} unpaired electrons per gram.

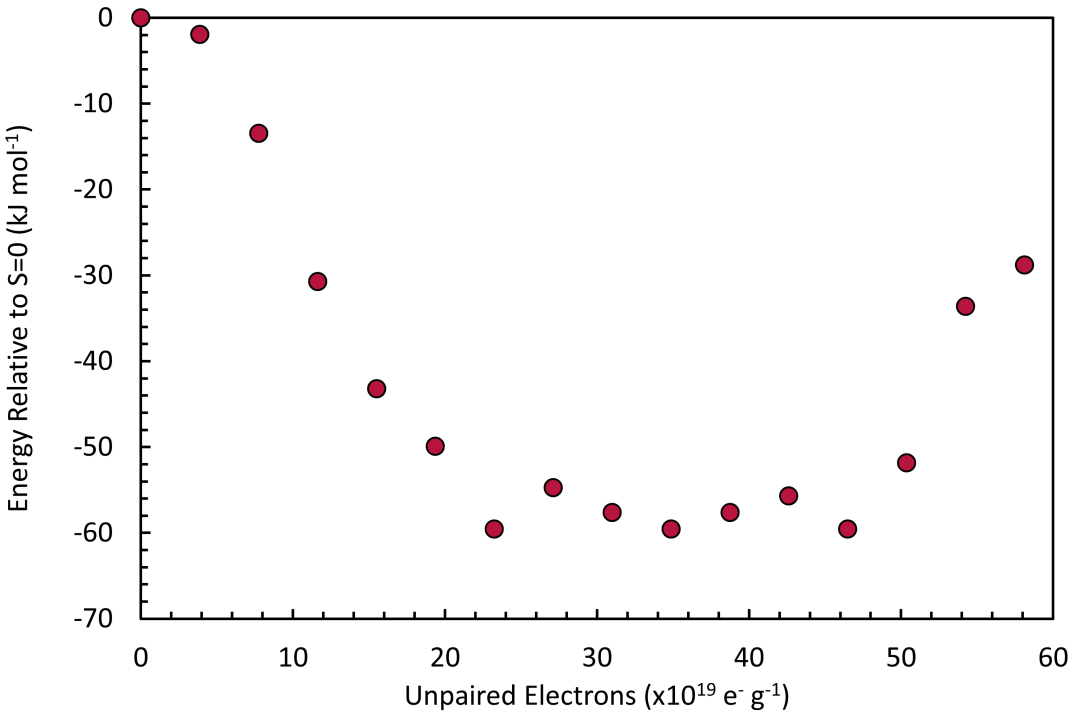

Figure 5.5: DFTB calculated relative energy as a function of enforced number of unpaired electrons on Nishihara Model II+.

5.3 Origin of Spin Polarization

Experimentally, it is evident there are some structural differences between ZTC and standard activated carbons like MSP-20 and MSC-30 that yields significantly different magnetic properties. Like well-known activated carbons, ZTC contains hydrogen- and/or oxygen-based functional groups at edge sites where the sp^2-hybridized network is interrupted in order to form permanent pores. Unlike activated carbons, ZTC is synthesized within an ordered microporous template (an aluminosilicate zeolite) under extreme steric confinement. Upon freeing the ZTC structure from the zeolite template, the remaining free-standing framework is composed predominantly of distorted graphene ribbon-like struts (which we refer to as "open-blade" structures). It is not clear a priori, and remains an open question in carbon materials research, which structural features of any carbonaceous solid give rise to magnetic susceptibility. The results of our experiments and computational modelling reveal that features prominent in ZTCs are more important contributors. But which aspects of the ZTC structure are most important contributors? We hypothesize that three structural features that could give rise to unpaired electrons are: unusual ring sizes (¿6-membered rings), framework contortions due to confinement, and/or edge-site features such as hydrogen terminations.

5.3.1 Ring Size Effects

Unlike activated carbons, ZTCs are forced to connect within a predefined pore network, thus inducing strain and ring sizes (from 5-9 membered rings) which may not be present in activated carbons. Schwarzites, fullerenes, and atomistic ZTC structures (Chapter 4) contain a myriad of ring sizes and serve as ideal atomistic models for evaluating the role ring size plays in spin polarization.

5.3.1.1 Methods Similar to Nishihara Model II+, DFTB+ was used to perform spin polarization calculations all other periodic models. However, the calculations performed with schwarzite, carbon allotrope, and ZTC models were performed without geometry optimization as forcing spin on these models while allowing the structure to change geometry lead to structure collapse. All schwarzite,[143] carbon allotrope,[144,145] and ZTC periodic models[118] were used as provided in literature. A periodic graphene model was generated by isolating a single layer of graphene from graphite and separating each layer by 60.0 Å. A periodic fullerene model was generated in a similar fashion, by isolating a single sphere and separating each C_{60} by 60 Å in every direction. The ZTC models chosen for this computational study were Nishihara Model 0a, Nishihara Model 0b, Nishihara Model I, and Braun Model R, which contain a combination of ring sizes, shown in Table 5.1.

Table 5.1: Contribution of ring sizes in selected **FAU**-ZTC models.

Model	Contribution of Ring Sizes			
	5	6	7	8
Nishihara Model 0a	-	71%	29%	-
Nishihara Model 0b	-	50%	50%	-
Nishihara Model I	23%	77%	-	-
Braun Model R	1%	73%	24%	2%

5.3.1.2 Results Benchmark computations performed on graphene perform as expected (Figure 5.6), with the lowest energy structure having no unpaired electrons. As the number

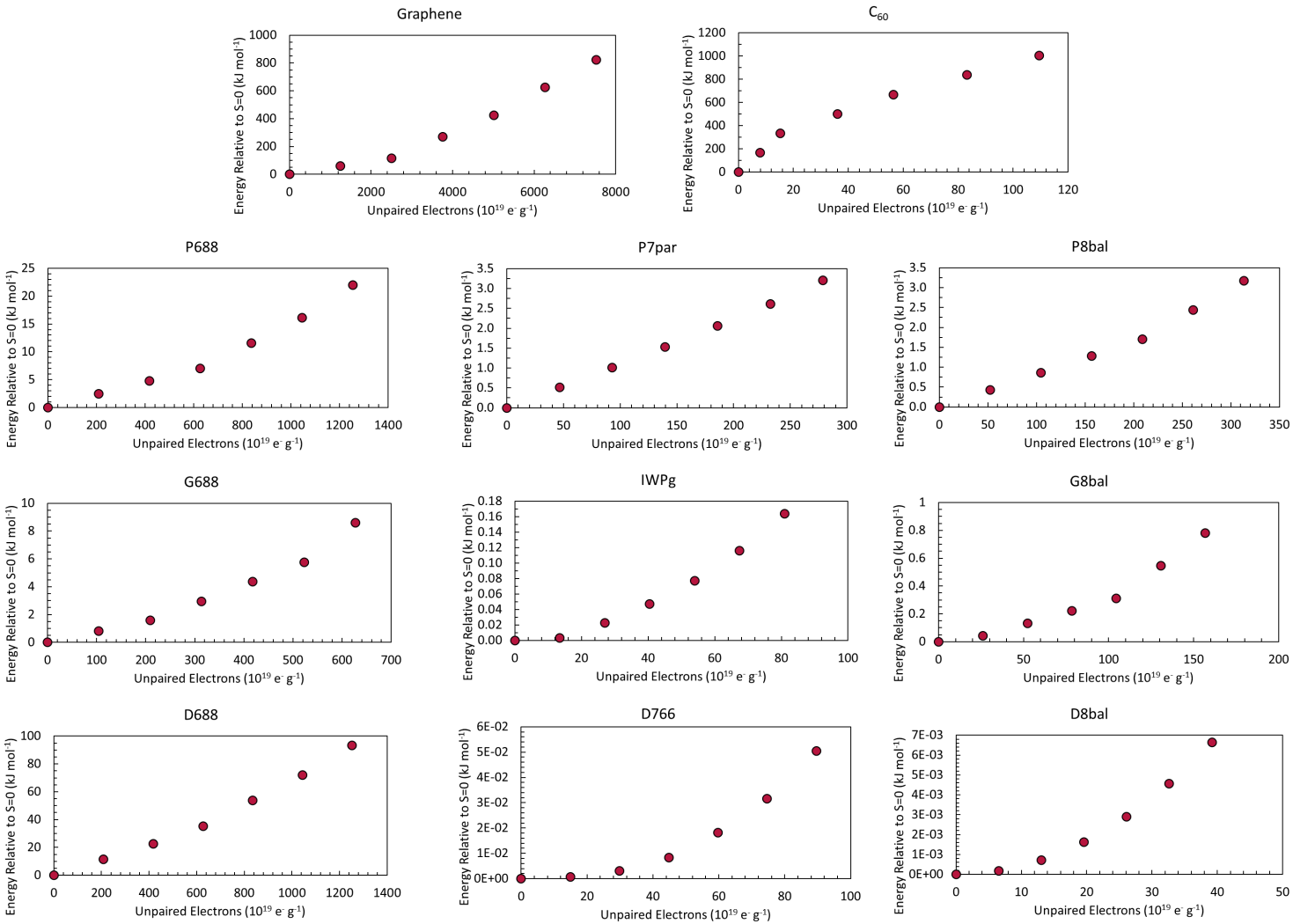

Figure 5.6: DFTB energetic results when forcing unpaired electrons on graphene, C_{60}, and small schwarzite models.

of unpaired electrons increases, so too does the relative energy of the structure, indicating that energetically graphene would be diamagnetic. The same trend can be seen for all periodic calculations on schwarzites, carbon allotropes, and ZTC models, as shown in Figures 5.6 and 5.7. These results suggest that incorporation of different ring sizes is not the cause of spin polarization in porous carbon materials.

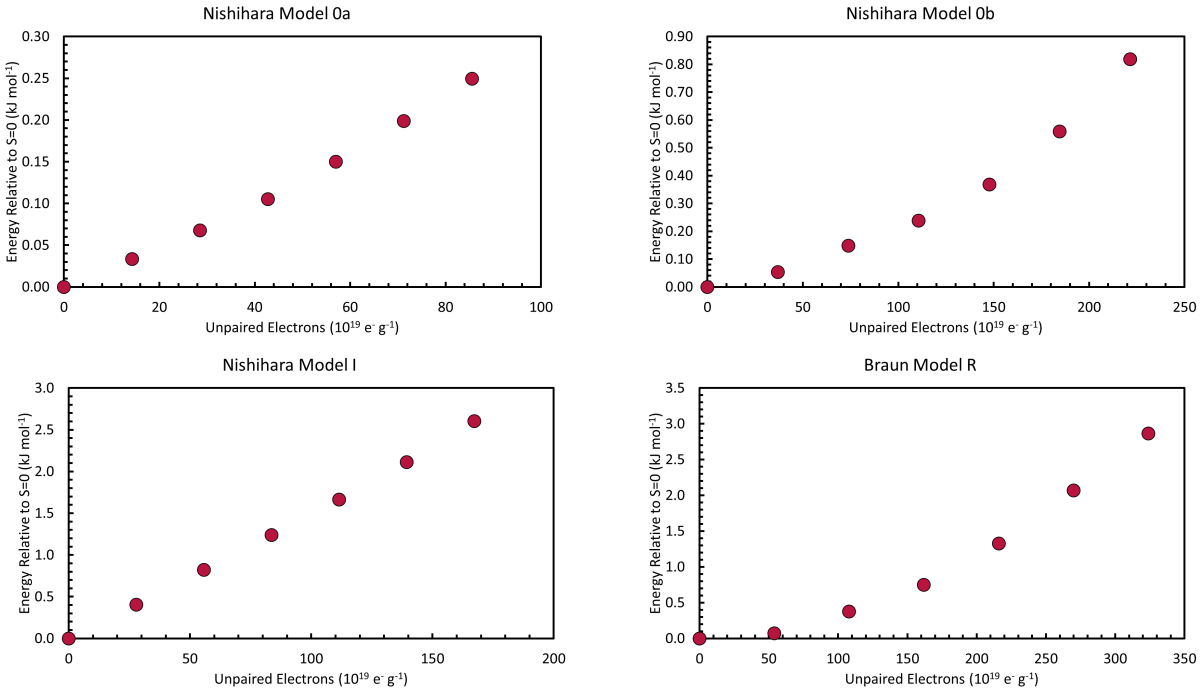

Figure 5.7: DFTB energetic results when forcing unpaired electrons on ZTC atomistic models.

5.3.2 Framework Confinement Effects

During CVD, ZTCs are forced to follow the pore structure of the zeolite template, inducing curvature into the carbon framework which activated carbons may not be subjected to. Curved vertexes in carbon surfaces have been theoretically suggested as locations where unpaired electrons can be trapped.[146]

5.3.2.1 Methods To investigate if framework folding could play a role in the presence of unpaired electrons in ZTC and MSC-30, small atomic-scale representative models with differing ring size combinations were generated as shown in Figure 5.8. The dihedral angles highlighted in Figure 5.8 were changed to fold the surface and these angles were fixed throughout the optimization process. Geometries of the folded models can be seen in Appendix F. All models were folded to a minimum of 100° with the exception of pyrene and dicyclopenta[ef,kl]heptalene which began collapsing after folding past 130° and 110°, respectively. These structures were optimized at the MN15/6-311++G** level evaluated in the singlet (no unpaired electrons) and triplet (two unpaired electrons) states. If in any configuration the triplet state was calculated to have a lower energy than the singlet state, the structure would be paramagnetic. All structures reported in this work were confirmed to be equilibrium structures without exhibiting any imaginary normal modes.

5.3.2.2 Results As seen in Figure 5.9, folding of the molecular models does not induce spin polarization as the triplet state is higher in energy than the singlet state at every geometry. These results suggest that framework folding is not the cause of spin polarization in porous carbon materials.

5.3.3 Edge-Site Character Effects

It is also been theoretically shown that edge sites in graphene-like surfaces can result in unpaired electrons, even leading to ferromagnetism, a particular magnetic response where unpaired electrons remain temporarily aligned after an external magnetic field is removed.[147–149]

If the amount of oxygen and hydrogen determined using combustion analysis, is assumed to mainly be located at edge-sites, the sum of oxygen and hydrogen content can be used as a

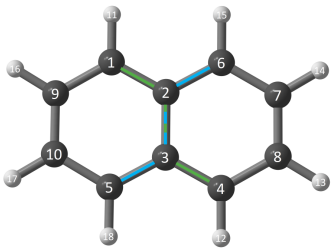

(a) napthlene

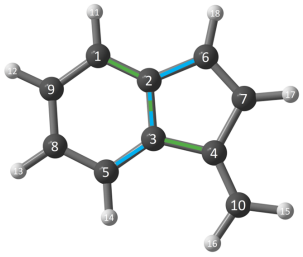

(b) 1-methyleneindene

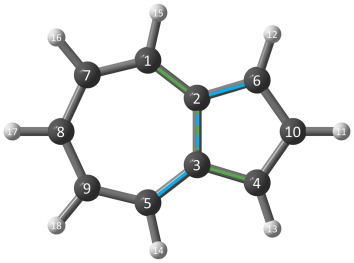

(c) azulene

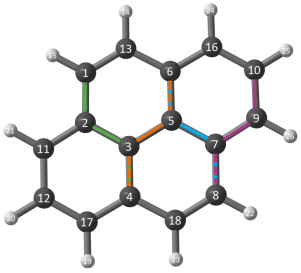

(d) pyrene

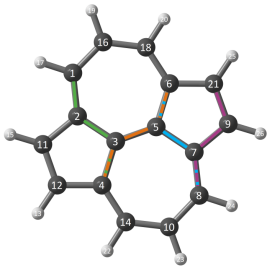

(e) dicyclopenta[ef,kl]heptalene

Figure 5.8: Set of molecular models used for folding calculations, by setting the highlighted dihedral angles to predetermined angles.

proxy for the percentage of edge-sites in a material. Figure 5.10 emphasizes the role amount of edge sites could contribute to the amount of unpaired electrons.

5.3.3.1 Methods ZTCs are made of blade-like struts which could be modeled by graphene nanoribbons, as shown in Figures 5.11 and 5.12. When cutting a graphene sheet to make a nanoribbon, the direction the sheet is cut can result in materials with two different edge characters; armchair edges and zigzag edges. To generate the graphene

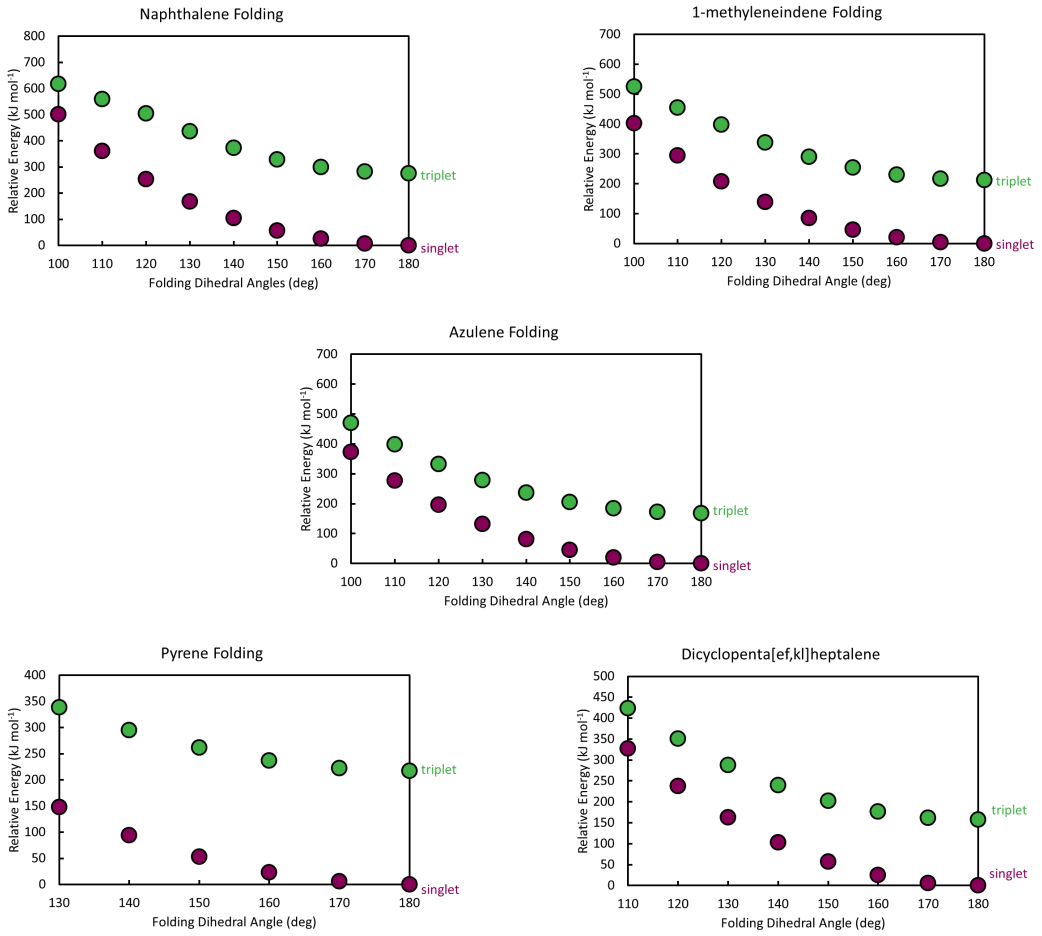

Figure 5.9: MN15/6-311++G** energetic results when folding molecular models in the singlet and triplet states.

nanoribbon structures, a periodic graphene sheet was cut into strips ranging from two rings wide (2R) to ten rings wide (10R) in two different directions resulting in armchair and zigzag edge terminated graphene nanoribbons. The nanoribbons were spaced 60 Å apart and geometrically optimized in a diamagnetic state using DFTB+. Then, as previously described single point calculations were performed with forced spin states applied.

5.3.3.2 Results As shown in Figure 5.13, armchair edge sites will lead to diamagnetic materials, as all structures with unpaired electrons are less energetically favorable than the

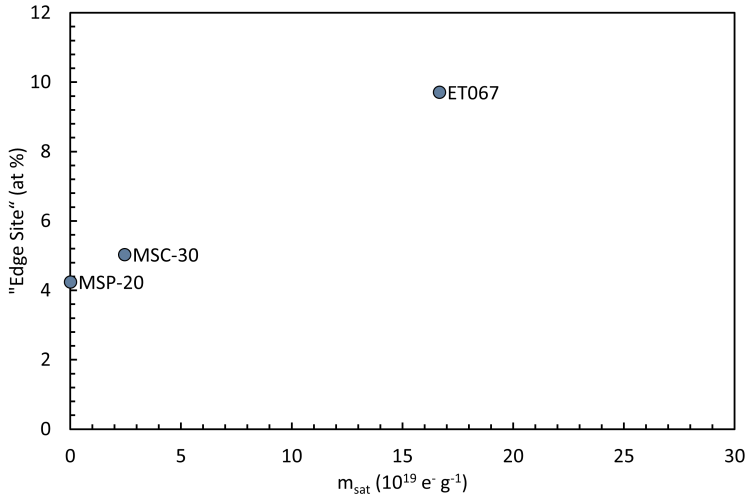

Figure 5.10: The contribution of edge sites in ZTC, MSC-30, and MSP-20 at determined from the oxygen and hydrogen content in combustion analysis plotted as a function of m_{sat} at 0K.

S=0 state. However, Figure 5.14 indicates that the presence of zigzag edges would result in as many as 8.35 $\times 10^{21}$ unpaired electrons per gram in a 2R zigzag edge terminated graphene nanoribbon. Out of all of the computations performed so far, graphene nanoribbons with zigzag edges are the only models that have indicated an energetically favorable presence of spin polarization. Further investigation of the paramagnetic zigzag edge nanographene models indicate that these unpaired electrons are concentrated at the hydrogen terminated edge carbon atoms (Figure 5.15). This begs the question, "Are unpaired electrons located near zigzag edges in Nishihara Model II+?".

5.3.3.3 Location of Spins in Nishihara Model II+ After selecting the five carbon atoms with the highest concentration of spin in the optimized variant of Nishiara Model II+ with 4.65×10^{20} unpaired electrons per gram (equivalent to 24 unpaired electrons per unit cell), snapshots of these high spin environments are shown in Figure 5.16. It is worth noting that four out of the five snapshots show the highest spin concentration on a hydrogen-terminated

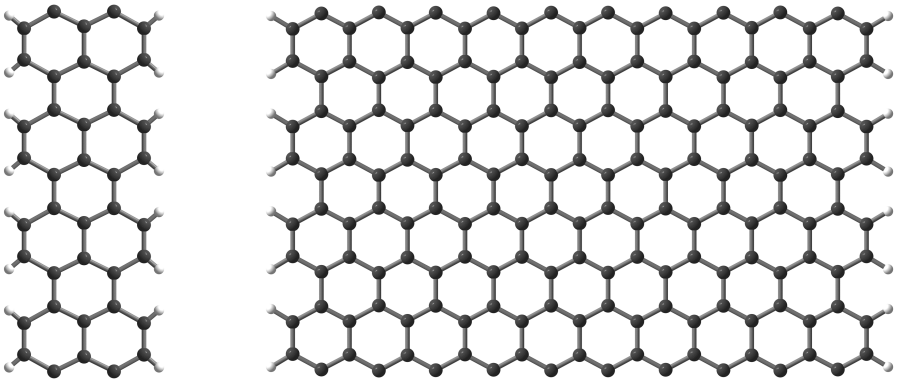

Figure 5.11: Representative graphene nanoribbon sub-units with armchair edge-sites ranging from 2-rings wide (2R) on the left to 10-rings wide (10R) on the right. These models are periodic and repeat along the top and bottom of each image.

zigzag edge, with all snapshots showing spin concentrated on zigzag edges in general. In some snapshots the concentration of unpaired electrons has been delocalized in the π-network over a six-membered ring. While ferromagnetism would not be expected for such disordered edge states, it is clear from these edge-site calculations that the presence of zigzag edges play a significant role in the spin polarization determined using DFTB. Further work remains to verify the validity of DFTB methods using higher levels of theory.

5.4 Conclusion

In this study, the magnetic susceptibility of ZTC was compared to MSC-30 and MSP-20, two high surface area activated carbons which are commonly compared to ZTC in literature. SQUID measurements detected 0, 2.46×10^{19}, and 1.67×10^{20} unpaired electrons per gram of MSP-20, MSC-30, and ZTC, respectively, indicating an expecially hihg content of unpaired electrons in ZTC. DFTB calculations performed on Nishihara Model II+ (Figure 5.5) indicate

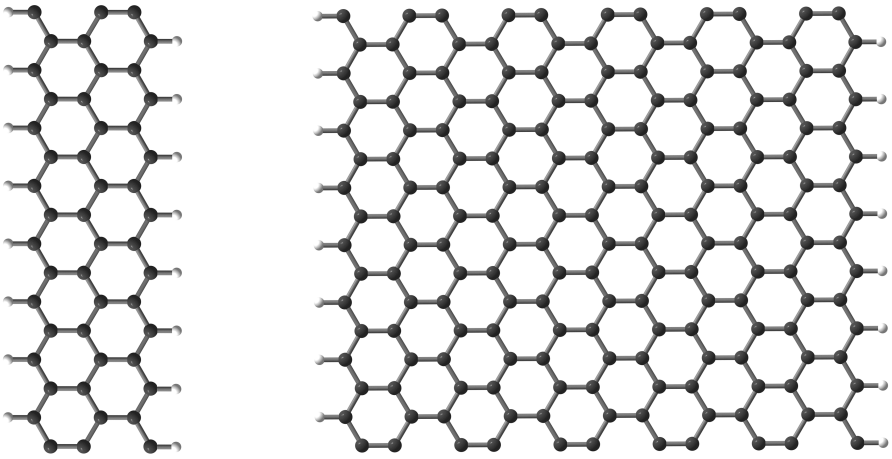

Figure 5.12: Representative graphene nanoribbon sub-units with zigzag edge-sites ranging from 2-rings wide (2R) on the left to 10-rings wide (10R) on the right. These models are periodic and repeat along the top and bottom of each image.

that ZTC materials could accommodate as many as 4.65×10^{20} unpaired electrons per gram, remarkably within the same order of magnitude as determined experimentally using SQUID measurements. According to a series of systematic DFTB calculations, most carbon models should be diamagnetic. Computational investigations of Nishihara Model II+ and systematic calculations using graphene nanoribbons indicate that the presence of unpaired electrons could be due zigzag type edge sites. Future work aimed at synthesizing a carbon schwarzite, whether within the pores of a zeolite or by any other synthetic route, would also benefit from quantification of paramagnetism as evidence for edge content that is uncharacteristic of such materials.

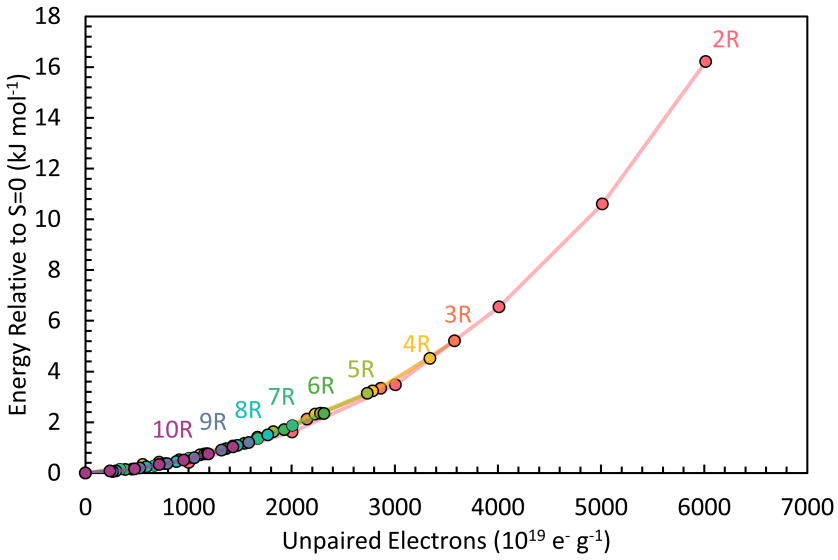

Figure 5.13: DFTB energetics resulting from forcing unpaired spin on armchair nanographene ribbons of different widths.

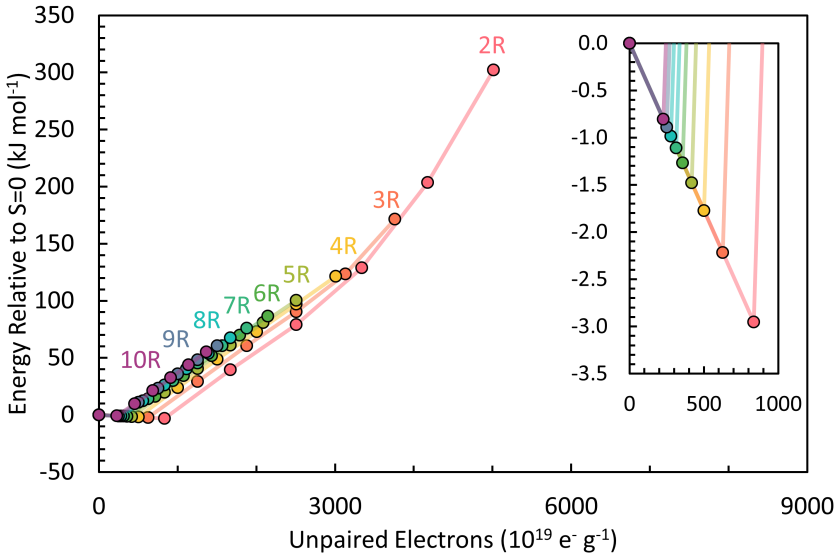

Figure 5.14: DFTB energetics resulting from forcing unpaired spin on zigzag nanographene ribbons of different widths.

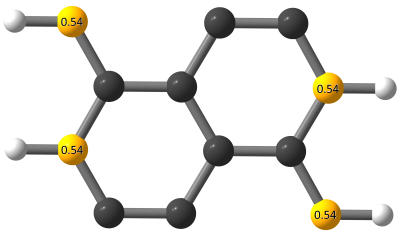

(a) 2R zigzag graphene nanoribbon

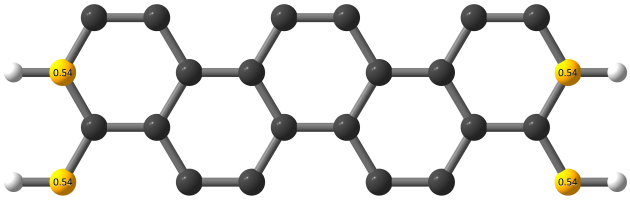

(b) 5R zigzag graphene nanoribbon

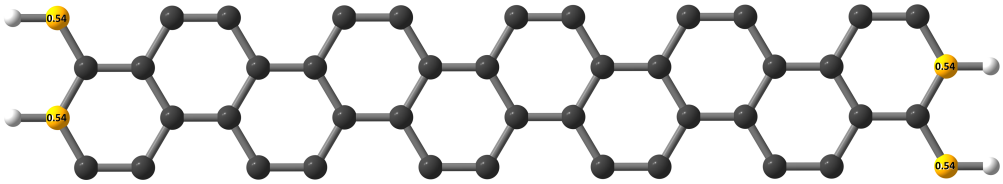

(c) 10R zigzag graphene nanoribbon

Figure 5.15: Spin distribution of zigzag terminated graphene nanoribbon structures.

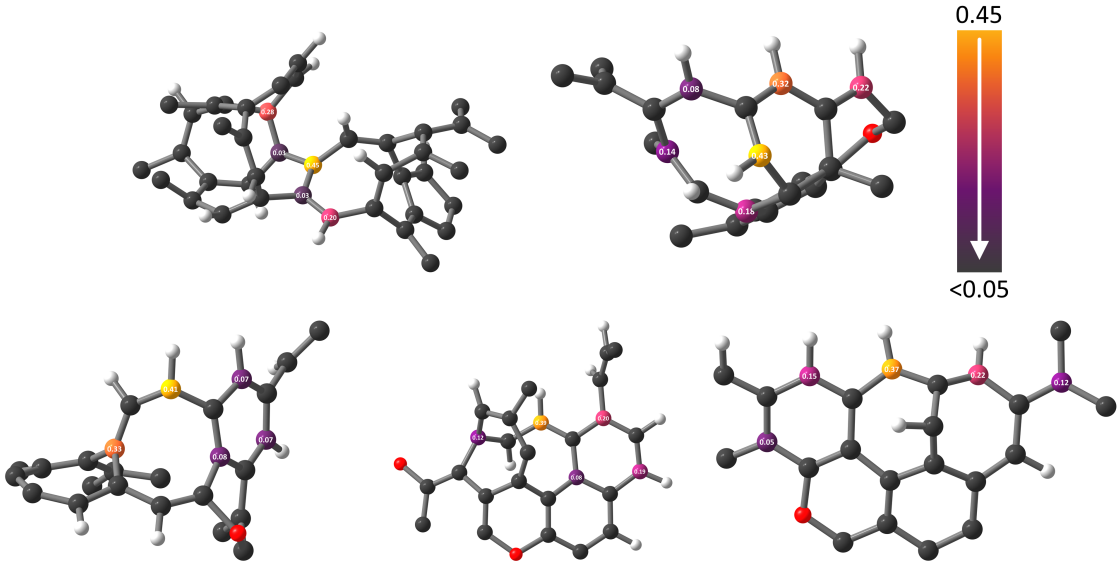

Figure 5.16: Location of the highest concentration of unpaired electrons in Nishihara Model II+.

CHAPTER SIX

CATION-EXCHANGED ZEOLITE-TEMPLATED CARBONS

As revealed by Braun and coworkers,[33] the key requirement for realizing a schwarzite-like material via zeolite templating is to deposit carbon directly and exclusively on the inner walls of the zeolite pores, as opposed to randomly within the entire pore volume (Figure 6.1). Thus, the goal of this work is to test how increasing the interaction strength of the growing

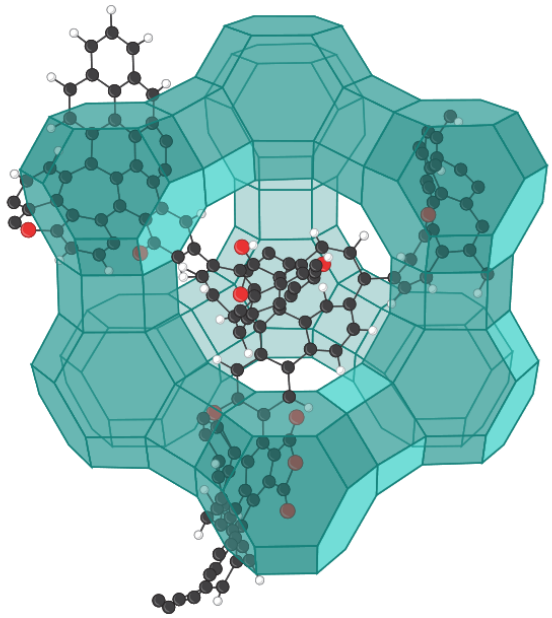

Figure 6.1: Representative depiction of an open-blade subunit of ZTC confined within a supercage of the **FAU** zeolite. Carbon, oxygen, and hydrogen atoms are shown in black, red, and white, respectively. The T sites (Si or Al) are shown as the vertices of a polyhedral depiction of **FAU** (teal lines and transparent faces) and zeolitic oxygen sites and cations are omitted for clarity.

carbon framework with the zeolite pore wall could result in schwarzite-like ZTC materials. To achieve this goal, this work focuses tuning the catalytic activity of the pore walls.

One major difference between schwarzite-like ZTC and experimental ZTCs is their SPD. Schwarzite-like ZTCs would exhibit a high SPD_{cell} of 0.63-0.71 g_{ZTC} $g^{-1}{}_{SiO_2}$ (see Table 6.1)

whereas currently existing high-quality experimental ZTCs typically exhibit SPD_{cell} 0.32 to 0.40 g_{ZTC} $g^{-1}{}_{SiO_2}$. Several strategies have been implemented to increase the SPD of ZTCs, including altering the deposition kinetics by means of P-CVD[72] and reducing the diffusion path length of precursor diffusion using nano-sized zeolites.[77] The highest SPD_{cell} values achieved to date are the following: 0.53 for P-CVD and 0.68 for nano-sized zeolites (all calculated using the same method herein). However, in these cases, over-deposition occurred[72,77] causing a graphitic shell to form on the external surface of the zeolite particles, resulting in a core-shell type structure. Hence, in both cases it was difficult to assess solely the SPD of the porous ZTC network and the solid was not a homogeneous framework.

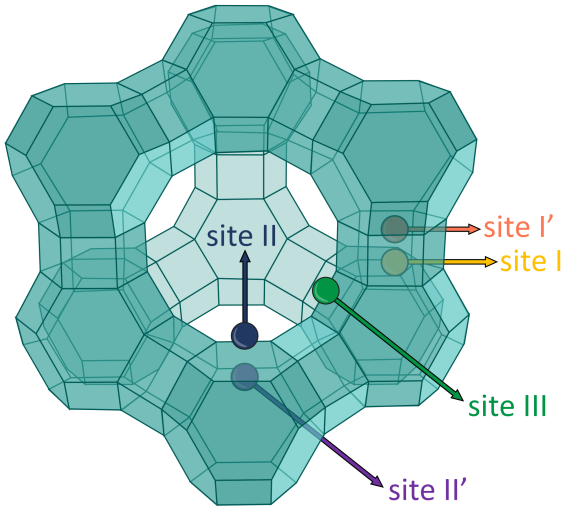

Figure 6.2: Extraframework cation sites in **FAU** zeolite supercell.

As mentioned previously (Chapter 2.1.1), zeolites can undergo a substitution of silicon with aluminum, requiring the introduction of an extra-framework charge-balance cation. The identity of the cation exchanged within the framework significantly influences the catalytic and functional properties of the zeolite.[59] These cations are located at extraframework positions in the unit cell; inside the hexagonal prism (site I), between the hexagonal prism and the sodalite cage (site I'), at the center of a hexagonal window inside the supercage (site II),

inside the sodalite cage (site II'), or in the supercage near a square window between two other square windows (site III), as labeled in Figure 6.2. Sites accessible in the pore network (site II and III) serve as adsorption sites for carbon molecules.[150] Thus, the polycyclic hydrocarbon rings formed during the synthesis of ZTCs can in principle participate in cation-π interactions[151] with the extra-framework cations present in the zeolite template. The strength of these interactions depends on the charge and size of the cations, increasing in strength as the size of the cation decreases. While multivalent cations increase the interaction strength and subsequent catalytic activity,[46,80] they also reduce the number of catalytic sites which could lead to carbon deposition heterogeneity. Monovalent cations like Li^+, Na^+, and K^+ all occupy sites II and III.[59] Therefore, in this study we aim to systematically investigate the effects of monovalent cation size on the template fidelity of **FAU**-ZTC by templating Li-, Na-, and K-exchanged variants of zeolite Y.

6.1 Cation-Exchange of Faujasite

Lithium-exchange was achieved using a previously reported procedure[152] by stirring 20 g of sodium-exchanged USY zeolite (HSZ-320NAA, Si:Al=11, Tosoh Corp.) in 200 mL of 1 M aqueous LiCl (99.0 %, J.T. Baker) at 80 °C for 4 h. The Li-exchanged zeolite was then filtered using cellulose filter paper (8 µm, Whatman 1002090), rinsed with water, dried under suction for 10 min, and then further dried at 80 °C for 12 h. The dried zeolite was then placed in an alumina boat (10 × 30 × 107 mm) which was inserted into a quartz tube (ϕ 45 mm) installed in a horizontal tube furnace (HST 12/600, Carbolite Gero) and heated to 350 °C at 1 °C per min, under flowing N_2 (99.999%). This procedure (comprising a single exchange step) was repeated five times in total. After each exchange step, 4 g of partially-exchanged zeolite were collected and a 10:1 ratio of LiCl solution volume to zeolite mass was maintained.

Potassium-exchange was achieved using a similar procedure as described above. Since

potassium can exchange with sodium more readily than lithium,[153] the concentration of potassium in each exchange solution was altered to create a diverse series of potassium-exchanged zeolites. This series was created by varying the volume ratio within a mixture of 1 M aqueous KCl (99.7%, Fisher Chemical) and 1 M aqueous NaCl (99.7%, Fisher Chemical). Mixtures containing volume ratios of 20:80, 40:60, 60:40, 80:20, and 100:0 were prepared in an attempt to achieve an extent of potassium exchange of 20%, 40%, 60%, 80% and 100%, respectively.

A control sample was also prepared to reveal any chemical or structural changes that could occur during the cation-exchange procedure described above. One exchange control step was performed using a similar procedure as in lithium- and potassium-exchange, with 5 g of USY zeolite (HSZ-320NAA, Si:Al=11, Tosoh Corp.) in 50 mL of 1 M aqueous NaCl (99.7%, Fisher Chemical).

The cation-exchanged zeolites are named to indicate the type of cation exchanged, the letter Y to indicate the zeolite type, and which exchange step the zeolite was collected after. For example, LiY3 and KY3 are zeolite Y samples that have undergone three cycles of lithium- and potassium exchange, respectively. The sodium-exchanged sample is referred to herein simply as NaY.

6.2 Zeolite-Templated Carbon Synthesis from LiY

All ZTCs were synthesized via a two-step method (see Appendix B) whereby 2 g of zeolite template was degassed in a glass oven (B-585, Büchi Corp.) at 300 °C for 24 h under oil-free vacuum ($< 2 \times 10^{-3}$ mbar). The dried zeolite template was then transferred into a 2-neck round-bottom flask in an inert atmosphere and 20 mL of furfuryl alcohol (FA, 98%, Aldrich) was added via syringe. The mixture was stirred at room temperature under passive vacuum for 12 h. The impregnated solid was then collected by vacuum filtration in air, washed three times with 10 mL aliquots of mesitylene (97%, Aldrich) and dried under

suction on the filter frit for 15 min. The impregnated and rinsed zeolite was then placed in an alumina boat (10×30×107 mm) which was inserted into a quartz tube (ø 45 mm) installed in a horizontal tube furnace (HST 12/600, Carbolite Gero). The tube was purged with dry argon flow (200 sccm) and the FA within the zeolite pores was first polymerized by heating up to 80 °C at 5 °C per min and held for 24 h. The poly-FA was then carbonized by heating up to 700 °C at 5 °C per min and held for 30 min. Carbon deposition was accomplished via propylene (200 sccm, 7 mol% 99.99% propylene in 99.999% argon) CVD at 700 °C for 5 h. After ambient pressure CVD, the gas flow was returned to dry argon at 200 sccm. A heat treatment step was performed by heating the zeolite-carbon composite up to 900 °C at 5 °C per min and held for an additional 3 h. The system was then cooled overnight, the gas flow was stopped, and the annealed zeolite-carbon composite was collected. Removal of the zeolite template was accomplished by three sequential dissoulutions in 35 mL of aqueous hydrofluoric acid (HF, 48-51%, Thermo Scientific). The final ZTC product was collected by centrifugation, washed three times with 35 mL aliquots of distilled water, and dried in air at 40 °C to obtain the final ZTC material. Some samples were subject to additional iterations of acid washing to ensure complete dissolution of the zeolite template, as determined by XRD.

6.3 Characterization of Cation-Exchanged Zeolites and Zeolite-Templated Carbons

6.3.1 Inductively Couples Plasma Optical Emission Spectrometry

The extent of cation exchange in each zeolite was determined via optical emission spectrometry (OES) using a benchtop inductively coupled plasma (ICP) emission spectrometer (Thermo iCAP-6500 Duo View, Thermo Scientific). Each sample of dried zeolite powder was dissolved in a series of proprietary reagents (UniSolv, Inorganic Ventures Inc.) prior to analysis.[154] First, 10 drops of water were added to 80 mg of zeolite to hydrate the sample and prevent agglomerations in a 250 mL Nalgene bottle. Then, 10mL of UA-1 (Inorganic

Ventures) and 0.5 mL of concentrated 70% nitric acid (Certified ACS Plus, Fisher Chemical) were added to the vessel, capped, and shaken for 2 min. The solution was neutralized by adding 50 mL of UNS-1 (Inorganic Ventures) and allowed to fully react. DI water was then added to achieve a final solution weight of 150 grams. To achieve homogeneity, the final solutions were mixed by inverting the capped bottles 50 times prior to further analysis.

6.3.2 X-Ray Diffraction

Powder XRD patterns were measured using Cu Kα radiation (λ=1.54 Å), generated at 40 kV and 40 mA, in Bragg-Brentano geometry (D8 Advance, Bruker Corp.). The powder was thinly dispersed on a "low-background" sample holder comprised of oriented crystalline silicon.

6.3.2.1 Nitrogen Adsorption Nitrogen adsorption/desorption isotherms were measured at 77 K between 10^{-4} and 100 kPa using an automated volumetric instrument (3Flex, Micromeritics Instrument Corp.). Specific surface areas were calculated by Brunauer-Emmet-Teller (BET) method between $P/P_0 = 5\times10^{-7}$-0.02 and $P/P_0 = 4\times10^{-6}$-0.10 for zeolite and ZTC samples, respectively. Pore-size distributions were determined by nonlocal density functional theory (NLDFT) calculations using a dedicated software package (MicroActive Share, Micromeritics Instrument Corp.) with a carbon slit-pore model.

6.4 Influence of Cation Identity in Zeolite-Templated Carbon Synthesis

Cation exchange across a wide range of compositions (up to 58% for Li and 94% for K) was achieved using a standard aqueous solution exchange method, as shown in Figure 6.3. Lithium-exchange is thermodynamically unfavorable owing to the stronger hydration energy of lithium as compared to sodium[153]; the maximum exchange concentration (58%) achieved in this work is comparable to the replicated study,[152,155] though greater lithium exchange has

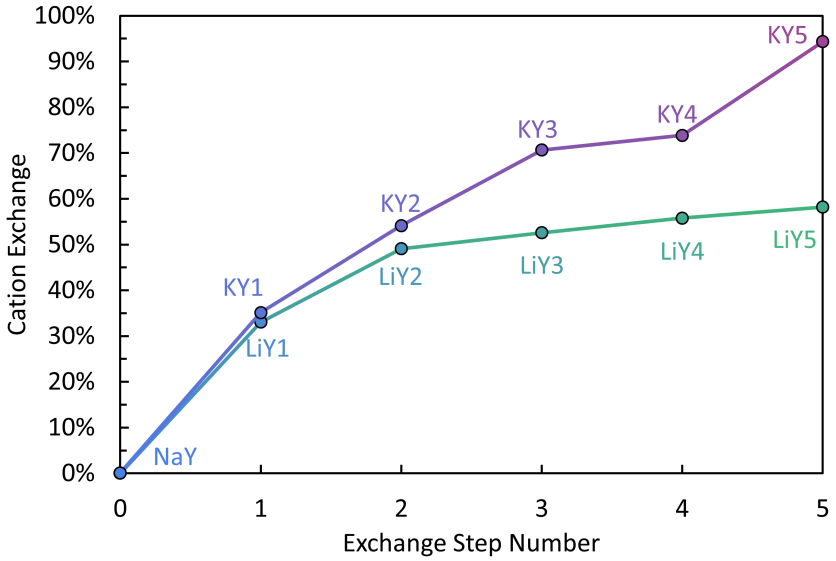

Figure 6.3: Composition of cation-exchanged **FAU** zeolite templates as a function of the exchange step number, as determined using ICP-OES.

been achieved using a lithium nitrate solution.[156] The potassium-exchange isotherm reaches a plateau between the third and fourth exchanges resulting in KY3 and KY4 having similar potassium exchange amounts.[157] Unlike lithium-exchange, complete potassium-exchange is eventually possible as previously reported.[59,156,158–160] The periodic structural integrity of the zeolite templates was maintained during cation exchange, without the loss of any characteristic XRD reflections, as shown in Figure 6.4.

The (222) reflection centered at $2\theta = 12.6^{\circ}$ intensifies upon potassium exchange at high concentrations owing to the larger scattering cross-section of K^+ compared to Na^+ and Li^+.[161] Some structural differences between the three cation-exchanged zeolites are evident by analysis of the nitrogen adsorption isotherms at 77 K (see Figure 6.5).

The pore volume decreases slightly upon incorporation of lithium and potassium (Table 6.2). Likewise, the pore size distribution of the cation-exchanged zeolites is also affected by cation identity; the larger pores present in LiY5 (~8.0 Å in width) are revealed

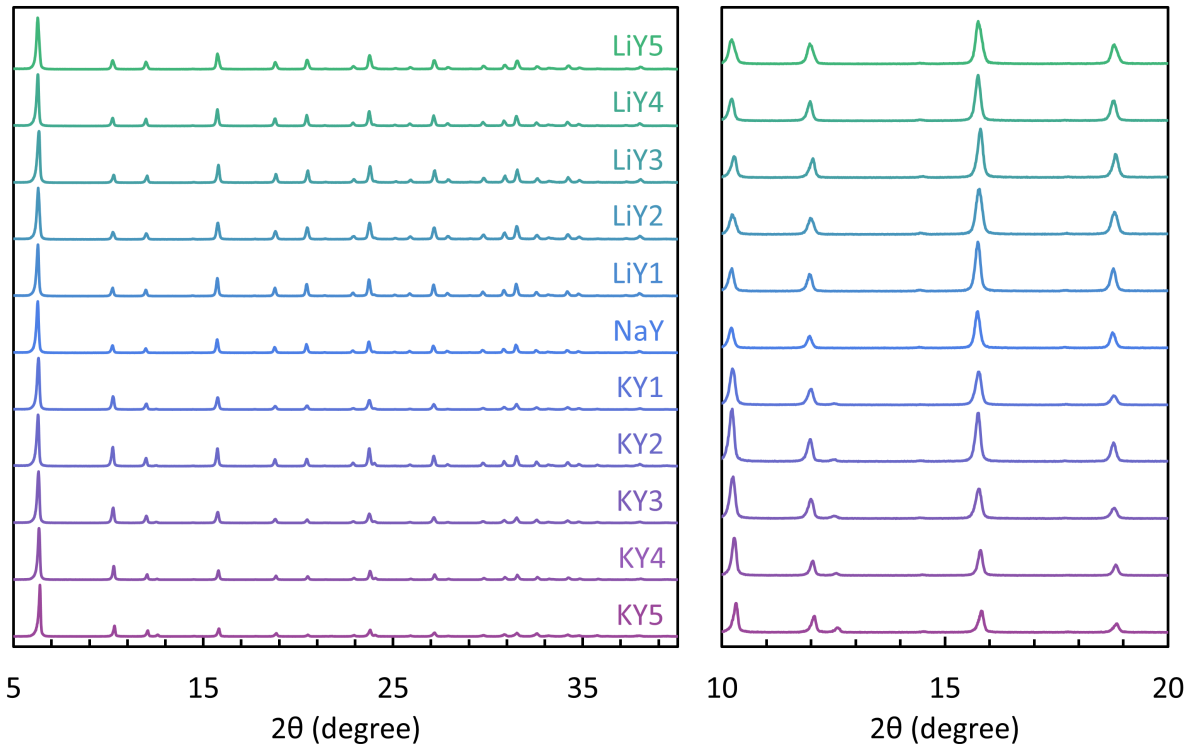

Figure 6.4: XRD patterns of the cation-exchanged **FAU** zeolite templates (originally NaY).

to decrease in prevalence as the cation size increases, as exemplified by comparison to NaY and KY5 (Figure 6.6).

Despite the minor differences in porosity of the templates as a function of cation exchange, no major change is evident in the periodic structure of the resulting ZTCs, as shown in Figure 6.8. All of the ZTCs exhibit a sharp (111) reflection at ∼6.5° in 2θ and the presence of a minor (220) reflection at ∼10.6° in 2θ indicating high pore-to-pore regularity and the same pore-to-pore spacing. Notably, no graphitic stacking is observed (expected at ∼26° in 2θ) which is typically the result of carbon deposition on the outer surfaces of the zeolite particles. Interestingly, once again, the nitrogen adsorption measurements reveal some differences between the ZTCs resulting from different cation exchange. As the size of the cation increases, surface area and pore volume also increase, as seen in Figure 6.6 and

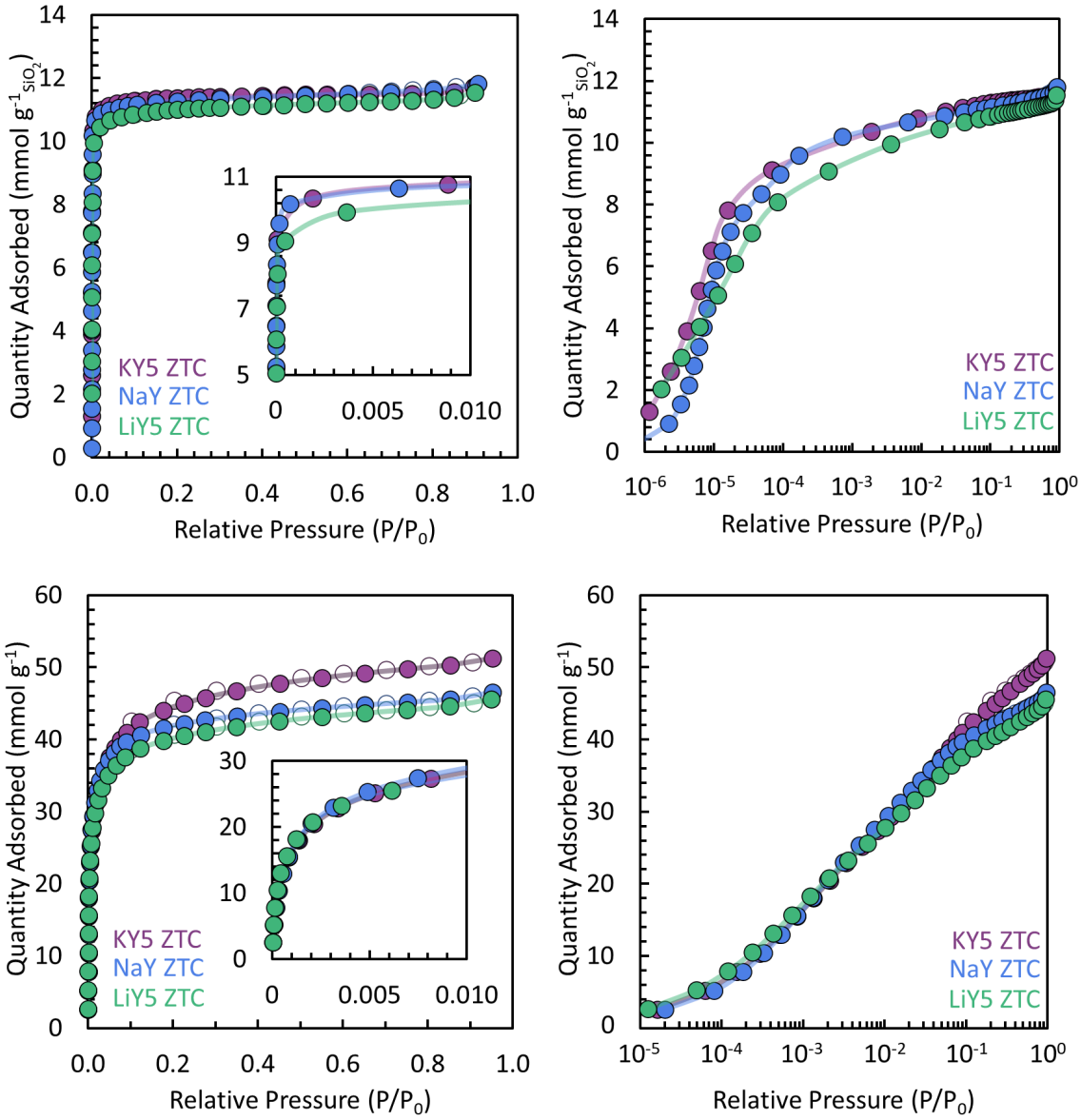

Figure 6.5: Nitrogen adsorption/desorption isotherms at 77 K of (a, b) select cation-exchanged **FAU** zeolite templates, converted to mmol $g^{-1}_{SiO_2}$, and (c, d) the corresponding ZTCs.

Table 6.2. The opposite trend is observed for SPD_{cell}, where carbon deposition within the zeolite template (slightly) increases with decreasing cation size (Figure 6.7 and Table 6.1).

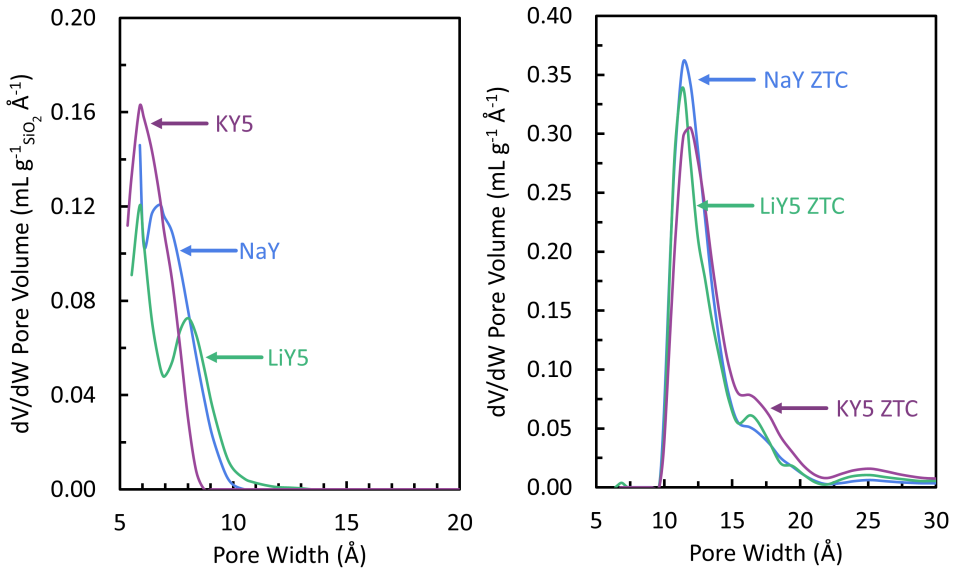

Figure 6.6: NLDFT pore size distributions of the cation-exchanged **FAU** zeolite templates, converted to mL $g^{-1}_{SiO_2}$ $Å^{-1}$ (left) and corresponding ZTC samples (right).

Lastly, combustion analysis (see Table 6.1) of the resulting ZTC samples shows a higher concentration of carbon in the overall chemical composition of KY5 ZTC when compared to both LiY5 ZTC and NaY ZTC, and a reversed trend for oxygen. The trends in SPD_{cell} and chemical composition, while subtle in magnitude, are a credible body of results as a whole.

Achieving schwarzite-like ZTCs will necessitate the formation of closed-tube carbon struts within the confined pore spaces of the zeolite template. Currently existing ZTCs, such as all of the materials produced in the present work, exhibit far lower carbon packing ($SPD_{cell} \leq 0.40$ g_{ZTC} $g^{-1}_{SiO_2}$) and far higher surface area (BET SA > 3000 m^2 g^{-1}) than would be predicted for such materials, as shown in Table 6.1.

As carbon packing within the zeolite gradually increases toward this goal, surface area and pore volume, as measured by a nitrogen molecular probe, would eventually be expected to decrease. The formation of fully enclosed closed-tube struts would be expected to result

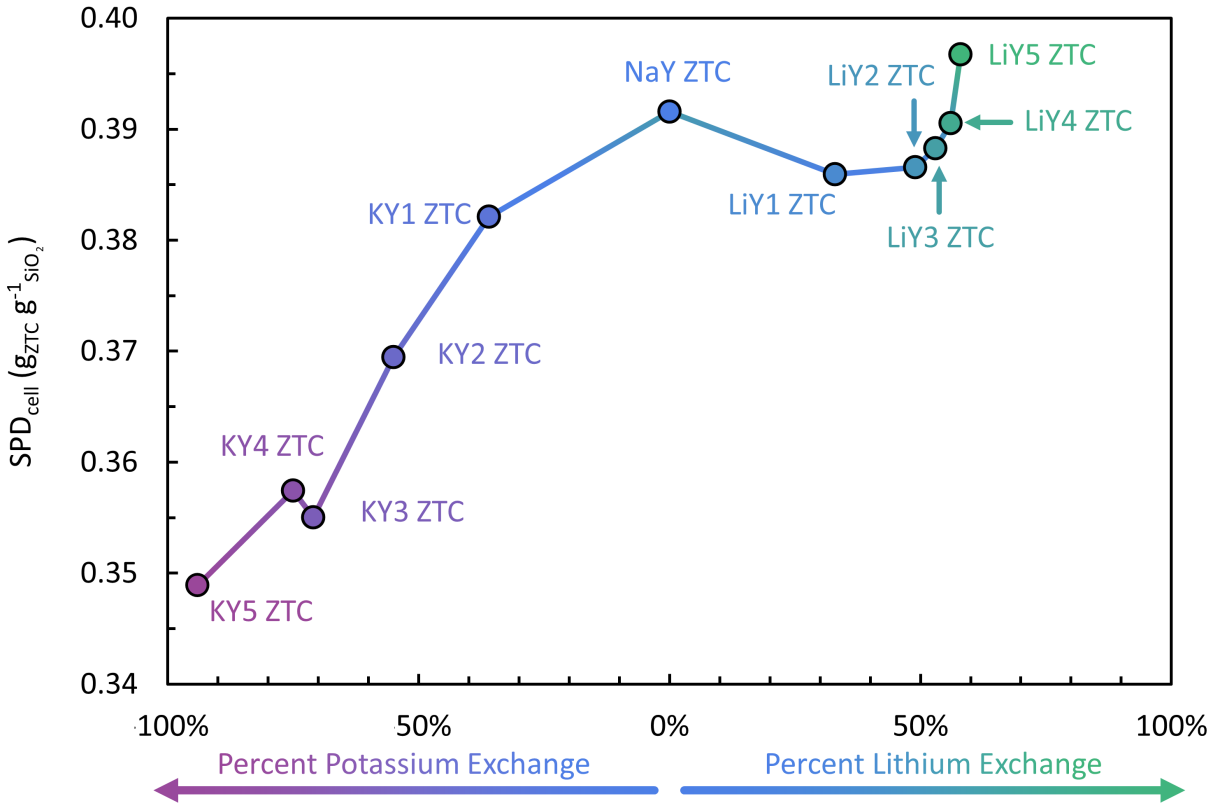

Figure 6.7: SPD plotted as a function of percent cation exchange in the zeolite template used to synthesize each respective ZTC.

in a surface area of less than half that of the open-blade variant as the pore space on the inner side of the struts becomes inaccessible to N_2. Such structures also comprise relatively more carbon than open-blade networks in addition to a higher SPD_{cell}. Therefore, the analysis of ZTC structure requires the use of combination of at least three characterization techniques together: diffraction, TGA, and elemental analysis. For example, a lower surface area could either be indicative of poor template fidelity leading to collapse of the atomically thin carbon walls upon zeolite removal, or could signal the disappearance of edge sites and an improvement in carbon deposition within the zeolite. In severe instances, the former case can be confirmed using powder XRD to detect graphitic stacking, while the latter can be verified

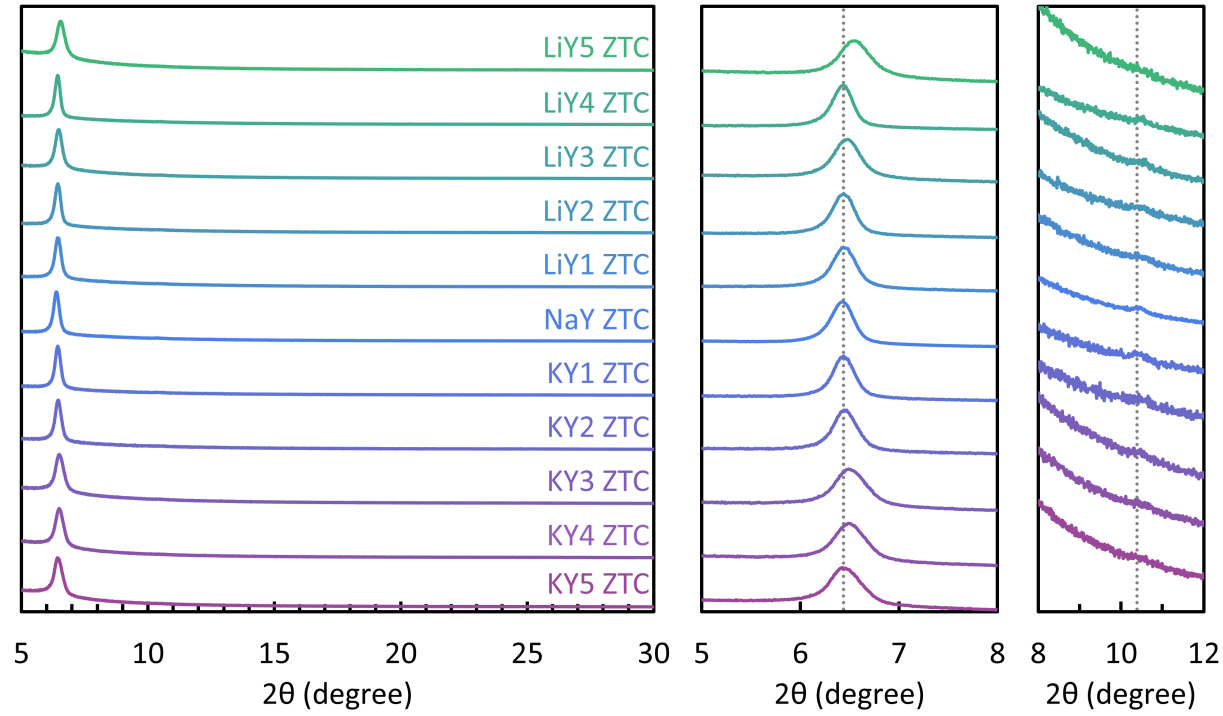

Figure 6.8: XRD patterns of ZTCs synthesized from cation-exchanged **FAU** zeolite templates. No internal standard was used to correct for sample height error.

using combustion analysis. As ZTCs consist of entirely sp^2-hybridized carbon,[102] hydrogen and oxygen must terminate edge sites of a graphene-like blade. The decrease in hydrogen content (Table 6.1) in accompaniment with lower BET surface area and pore volume signifies the disappearance of edge sites in LiY5 ZTC. Oxygen functional groups could also terminate edge sites; however, a majority of the oxygen contamination is proposed to originate from σ radicals, which are originally stabilized by the zeolite pore walls, and ultimately quenched by oxygen during the zeolite removal process.[76] Therefore, the increase in oxygen content could imply a ZTC structure which is overall templated closer to the zeolite pore wall. In comparison, KY5 ZTC exhibits both a higher BET surface area and pore volume with lower SPD_{cell} and oxygen content, indicating an open-blade structure templated mainly in the pore volume of the zeolite template. The observed difference in oxygen content between

Table 6.1: SPD, BET surface area (SA), and pore volume of ZTCs synthesized from cation-exchanged **FAU** zeolite templates compared to benchmark ZTC models.

Material/Model	**SPD_{cell}** (g_{ZTC} $g^{-1}_{SiO_2}$)	**ZTC BET SA** (m^2 g^{-1})	**ZTC Pore Volume** (mL g^{-1})	**C** (at%)	**H** (at%)	**O** (at%)
LiY5 ZTC	0.40	3360	1.57	78.4%	14.7%	6.4%
NaY ZTC	0.39	3560	1.60	78.6%	15.7%	5.3%
KY5 ZTC	0.35	3650	1.76	80.5%	15.7%	4.6%
Nishihara Model II+	0.35	4290	1.61	71.2%	23.8%	5.0%
Braun Model R	0.68	1600	0.62	100%	0%	0%

ZTCs insinuates future complications in the synthesis of high template fidelity ZTCs. If templating close to the zeolite walls results in the formation of σ radicals, oxygen may be inherently grafted to the structure of even high-fidelity schwarzite-like ZTCs. Therefore, a rigorous quenching of the σ radicals (e.g., with hydrogen gas[76] or post-synthetic heat-treatments/modifications) may be necessary to achieve a pure carbon structure. Such studies remain outside the scope of the present work but are warranted in future efforts to decouple the oxygen content from the edge content in post-HF dissolved ZTCs. In addition, it is notable that while some structural differences are observed between LiY5 ZTC and NaY ZTC (Table 6.1), the maximum effect of lithium-exchange within zeolite Y has not yet been fully captured. The CVD conditions, which were not varied in this work, would need to be optimized to determine if even higher SPD_{cell} could be achieved without the presence of graphitic stacking on the outside of the template particles.

6.5 Conclusion

Lithium- and potassium-exchange across a wide range of compositions were performed within zeolite Y using a standard procedure; 58% and 100% exchange was accomplished in five exchange steps, respectively. High template fidelity ZTCs were then prepared from all

Table 6.2: BET surface area (SA) and pore volume of cation-exchanged **FAU** zeolite templates.

Zeolite	**Zeolite BET SA** ($\mathbf{m^2\ g^{-1}_{SiO_2}}$)	**Zeolite Pore Volume** ($\mathbf{mL\ g^{-1}_{SiO_2}}$)
LiY5	1000	0.40
NaY	1040	0.41
KY5	1050	0.38

templates under identical impregnation and CVD conditions without any apparent graphitic growth on the external surfaces of the zeolite particles. Minor but important trends in the properties of the resulting materials are insightful for future efforts to prepare less open-blade-like and more closed-tube-like ZTC materials. Increasing the amount of potassium in the template led to more open-blade like structures with lower SPD_{cell} and higher BET surface area and total pore volume. On the other hand, templating LiY revealed early signs of a transition to more closed-tube-like structure, with lower BET surface area and hydrogen content. Future efforts to synthesize schwarzite-like ZTCs will require optimization of the synthesis conditions within LiY templates and may also require post-synthetic treatments to scavenge σ radicals in order to obtain a higher carbon content structure.

CHAPTER SEVEN

ENHANCED METHANE BINDING ON NC_3-TYPE NITROGEN-DOPED ZEOLITE-TEMPLATED CARBONS

Archetypical ZTC exhibits a high surface area and exclusively 1.2 nm pores making ZTCs ideal materials for methane storage.[162–164] Nitrogen and other heteroatom substitution (also referred to as "doping") of carbon-based materials is a common strategy used to tune material properties for specific applications. Among the heteroatom elements suited to direct substitution within the carbon lattice, nitrogen is perhaps the most common and easiest to incorporate, due to the availability of stable nitrogen containing precursors. Nitrogen also gives rise to perhaps the widest variety of different substitution types. In a pristine sheet of graphene with negligible edge content, nitrogen substitution can give rise to at least three important types of defects (see Figure 7.1): NC_3-type sites (also referred to as "graphitic"), :NC_2-type sites (also referred to as "pyridinic"), and, in the presence of hydrogen, HNC_2-type sites (also referred to as "pyrrolic").

Interestingly, little investigation of the effects of N-doping on methane adsorption has been reported, likely owing to a low overall incentive to increase methane binding at near ambient conditions (carbon materials without any surface modification already exhibit extraordinary densification of methane for mobile applications[165,166]). Recent systematic studies of the effects of heteroatom substitution on methane binding by an exhaustive suite of computational methods demonstrate that nitrogen doping (NC_3-type) can lead to a subtle but practically relevant increase in methane binding on open carbon surfaces, like ZTCs.[118,167]

FAU-ZTCs are promising methane storage materials[162,168,169] due to their inherited 1.2 nm pore size, optimal for methane adsorption.[165,170] However, **FAU**-ZTCs exhibit room-

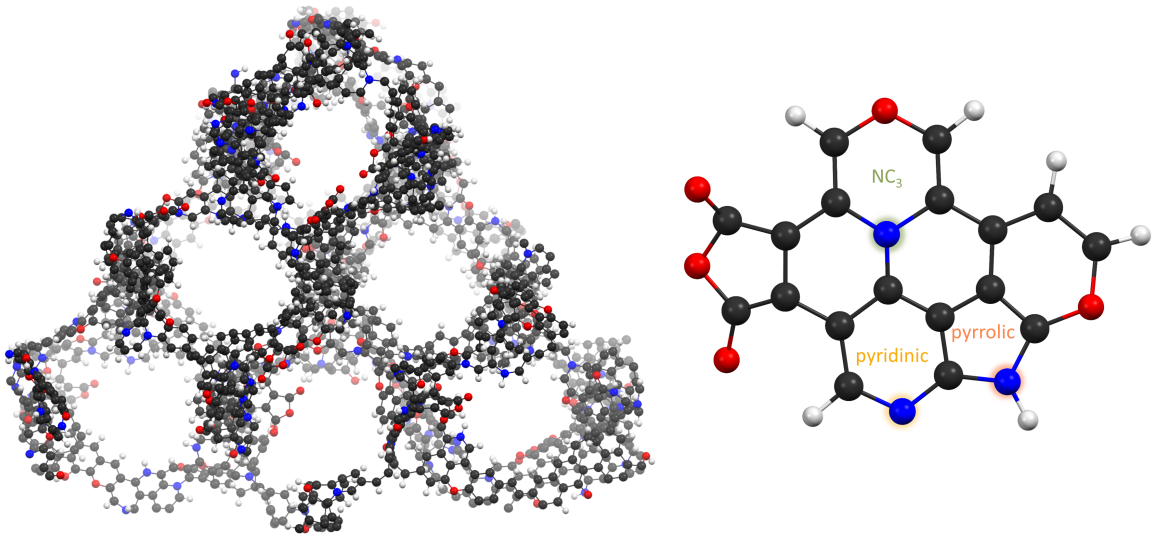

Figure 7.1: An extended multicell model of idealized N-ZTC with hydrogen, carbon, nitrogen, and oxygen shown in white, black, blue, and red, respectively. A representative N-ZTC fragment is highlighted showing graphitic, pyrrolic, and pyridinic type nitrogen environments.

temperature isosteric heats of adsorption around 14 kJ mol^{-1},[165,170] which is lower than the often referenced target of 19 kJ mol^{-1} for reversible methane binding energy.[164] A recent high-level computational study has suggested that graphitic-type nitrogen environments could amplify the induced dipole created during methane adsorption on a carbon surface, increasing the methane binding interaction by up to 3 kJ mol^{-1}.[167]

Nitrogen-doped ZTC (N-ZTC) synthesis was first attempted in 1997 via liquid impregnation of acrylonitrile into an NaY template.[29] A reported 6 at% nitrogen was incorporated into the carbon framework; however, the resulting material exhibited low surface area (700 m^2 g^{-1}) and no characteristic (111) reflection characteristic of archetypical **FAU**-ZTC.[28] This, along with the presence of an intense broad peak at 2θ=25° (characteristic of graphitic stacking), indicates collapse of the ZTC structure upon template removal.

Since then, many different precursors and synthetic techniques have been used to dope ZTC framework materials with nitrogen (see Table G.1),[83,84,92,101,117,171–174]; the highest template fidelity was achieved by Hou et al. via the incorporation of acetonitrile during CVD.[171] Nitrogen-doped ZTCs (N-ZTCs) have not yet been investigated as methane storage materials. In this work, we optimized the Hou syntehsis of N-ZTC to examine the effects of N-doping on methane binding, with a focus on NC_3-type environments for best comparison to computational predictions.

7.1 Nitrogen-Doped Zeolite-Templated Carbon Synthesis

N-ZTC was synthesized using a two-step method, inspired by the method first reported by Hou et al.[171] First, furfuryl alcohol (20 mL, FA, 98%, Aldrich) was impregnated into dried USY zeolite template (2 g, HSZ-320NAA, Si:Al=11, Tosoh Corp.). The impregnated zeolite was then filtered and washed with mesitylene (97%, Aldrich) to remove any remaining FA from the surface of the zeolite particles. The FA-zeolite composite was then placed in an alumina boat (10×30×107 mm), introduced into a horizontal quartz tube furnace (HST 12/600, Carbolite Gero), and heated to 80 °C at 5 °C per min under flowing dry argon (200 sccm) for 24 h to polymerize the FA inside the zeolite pore network. The polyFA-zeolite composite was then heated to 800 °C at 5 °C per min, at which point chemical vapor deposition (CVD) was achieved by bubbling dry argon (200 sccm) through acetonitrile (anhydrous, 99.8%, Sigma Aldrich) for 2 h. The vapor pressure of acetonitrile was varied by altering the temperature by placing the round bottom flask with acetonitrile either in an ice bath (0 °C, IB) or at room temperature (20 °C, RT). Following CVD, the gas flow was changed to dry nitrogen flow (200 sccm) and the carbon-zeolite composite underwent a heat treatment step by heating to either 850 °C or 900 °C at 5 °C per min and held for 1 h.

An archetypical ZTC sample was also prepared for comparison. The sample zeolite templated impregnated and polymerized in the same manner as for the N-ZTCs. After

polymerization, the composite was heated to 700 °C at 5 °C per min and carbon deposition was accomplished via propylene (200 sccm, 7 mol% 99.99% propylene in 99.999% argon) CVD at 700 °C for 5 h. After ambient pressure CVD, the gas flow was returned to dry argon at 200 sccm. A heat treatment step was performed by heating the zeolite-carbon composite up to 900 °C at 5 °C per min and held for an additional 3 h. In both the ZTC and N-ZTC syntheses, the system cooled overnight when heat treatment ended, gas flow was stopped, and the annealed zeolite-carbon composite was collected. Removal of the zeolite template was accomplished by three sequential dissolutions in 35 mL of aqueous hydrofluoric acid (HF, 48-51%, Thermo Scientific). The product was collected by centrifugation, washed three times with 35 mL aliquots of distilled water, and dried in air at 40 °C to obtain the final ZTC or N-ZTC material.

The N-ZTC materials are named to indicate the acetonitrile bath temperature: "IB" to indicate ice-bath temperature acetonitrile and "RT" to indicate 20 °C or room-temperature acetonitrile, followed by the heat-treatment temperature. For example, N-ZTC-IB-850 is a nitrogen-doped ZTC sample synthesized by bubbling nitrogen through acetonitrile submerged in an ice bath and then heat treated at 850 °C. The archetypical ZTC sample is referred to herein simply as ZTC.

7.2 Materials Characterization

Powder XRD was measured with Cu Kα radiation (λ=1.54 Å), generated at 40 kV and 40 mA, in Bragg-Brentano geometry using a theta-theta diffractometer (D8 Advance, Bruker Corp.). The powder was thinly dispersed on a "low-background" sample holder comprised of oriented crystalline silicon. Nitrogen adsorption/desorption isotherms were measured at 77 K between 10^{-4} and 100 kPa using an automated volumetric instrument (3Flex, Micromeritics Instrument Corp.); samples were prepared by degassing at 400 K overnight under active vacuum. Specific surface areas were calculated by fitting the

adsorption equilibria to a Brunauer-Emmet-Teller (BET) model between $P/P_0 = 3\times10^{-7}$-0.11, according the Rouquerol consistency criteria.[122] X-ray photoelectron spectroscopy (XPS) measurements were performed with Al Kα radiation (1486.6 eV) as the excitation source under ultra-high vacuum using a Physical Electronics 5600 spectrometer. Samples were prepared for XPS by pressing into indium foil on an aluminum sample holder. Depth profiling was performed by sputtering a 2×2 mm area of the sample with a 2 keV argon ion beam for specified periods of time (in min) between measurements. Spectra were analyzed by fitting to Gaussian line shapes and a Shirley background using a dedicated software package (AugerScan, RBD Instruments Inc.). X-ray absorption spectroscopy (XAS) measurements of the nitrogen K-edge were performed at beamline 7.3.1 of the Advanced Light Source (ALS), Lawrence Berkeley National Laboratory (LBNL); samples were mounted on carbon tape and transferred into an ultrahigh vacuum (10^9 mbar) chamber for analysis. XAS spectra were processed using the dedicated software package (ATHENA, Demeter).[175]

Methane adsorption/desorption isotherms were measured at 238-328 K using a custom volumetric Sieverts apparatus.[122,176] Samples were prepared by degassing overnight at 400 K under oil-free turbo molecular vacuum; between successive isotherms, each sample was reheated to 328 K and evacuated to the same base pressure. The isotherms were fitted using a global seven parameter dual-site Langmuir equation that is thermodynamically consistent and accounts for corrections due to non-ideality of the bulk fluid.

7.3 Results

Nitrogen doping was confirmed to be achieved via several characterization techniques. The nitrogen-content and binding configurations of N-ZTCs were examined using XPS and XAS. XPS is commonly used to determine the elemental composition as well as nitrogen binding environments in N-ZTCs, however, XAS had not previously been reported for N-ZTCs and there is general disagreement as to assigning the peak positions of N-

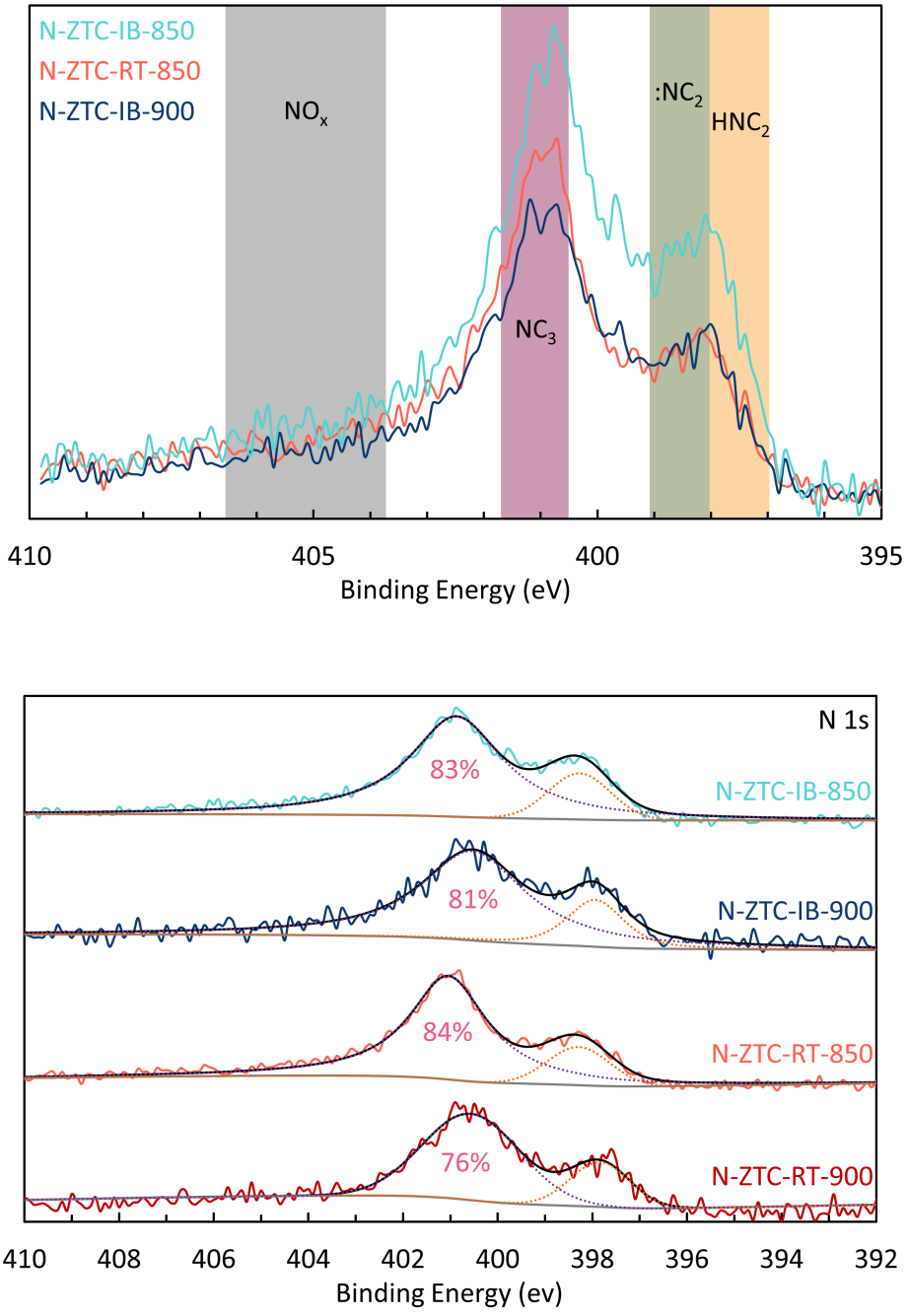

Figure 7.2: (top) XPS analysis of the nitrogen 1s region of N-ZTCs, and (bottom) XPS spectra of the nitrogen 1s region of N-ZTCs fit with Shirley background, NC_3 peak, pyrrolic/pyridinic nitrogen peak, and peak sum shown in grey, light purple, yellow, and black, respectively. The percent NC_3-type is shown under the peak fit.

type dopant environments in carbon materials (see Table H.1).[177–186] Nitrogen-substituted carbon materials typically exhibit four types of nitrogen-dopant environments distinguishable by XPS: N-oxide (406 eV), NC_3-type (401 eV), pyrrolic (398 eV), and pyridinic (397 eV). Two distinct features are present in the N 1s XPS spectra of N-ZTCs (see Figure 7.2). These two features at 401 and 398 eV are assigned herein to graphitic and a convolution of pyrrolic/pyridinic nitrogen environments, respectively, as assigned elsewhere.[83,171] No N-oxide contributions were detected. As shown in Table 7.1, the combination of FA with acetonitrile results in mainly graphitic type N-dopant environments, ranging from 76% to 84% (see Figure 7.2). XAS confirms the presence of predominately NC_3 type nitrogen dopants as shown in Figure 7.3. While there is general disagreement pertaining to the assignment of nitrogen dopant environments within the nitrogen K-edge, the assignments adopted herein are shown in Figure 7.3. The presence of pyrrolic and pyridinic type nitrogen are easily resolved in the XAS spectra (contrary to their overlap in XPS spectra). However, owing to the complex background of the edge, the relative contributions from all three observed nitrogen environments was not possible.

The XRD pattern of each N-ZTC exhbitis the characteristic feature of **FAU**-ZTCs: a (111) reflection at $2\theta{=}\sim6.5^\circ$ indicating pore-to-pore regularity imparted from the parent zeolite template, as seen in Figure 7.4. The (111) reflection is broader and weaker in intensity than that of archetypical ZTC, indicating a more amorphous pore network and lower template fidelity. No graphitic stacking is observed (expected at $2\theta{=}\sim26^\circ$) which can be the result of ZTC framework collapse after removing the zeolite template, or carbon deposition on the outer surfaces of the zeolite particles. Lower template fidelity is also supported by the results of N_2 adsorption characterization. N-ZTCs exhibit much lower surface areas than archetypical ZTC (see Table 7.1) indicating the partial collapse of the N-ZTC framework after template removal.

Methane adsorption equilibria were measured between 234-328 K and fitted to a global

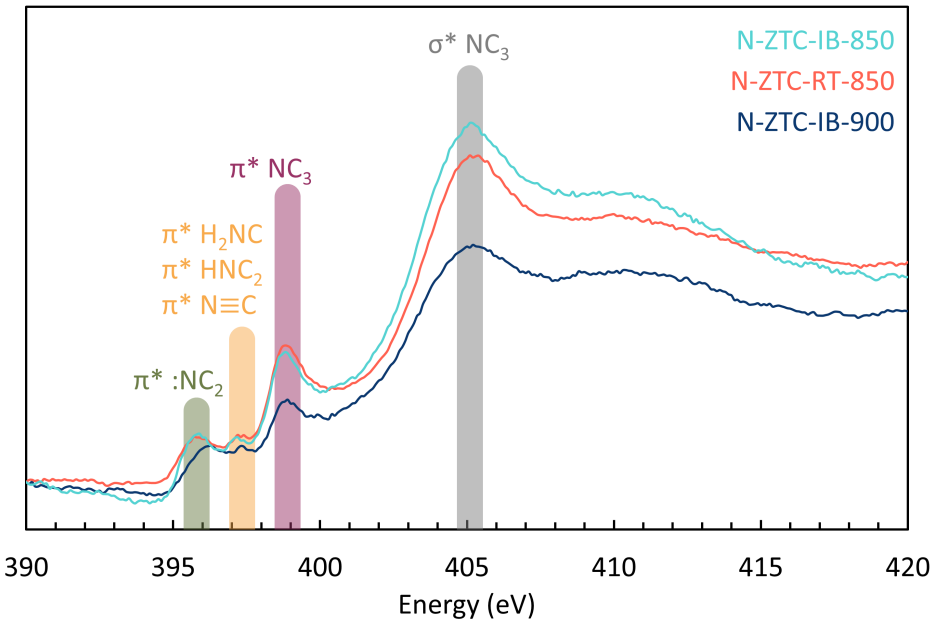

Figure 7.3: Nitrogen K-edge XAS analysis of N-ZTCs.

adsorption model, as previously described.[187] The isosteric heat of adsoprtion (-ΔH) was calculated from this fit using the Clapeyron equation. The results indicate an increase in methane binding enthaply on all N-ZTCs, by up to 1.3 kJ mol^{-1} on N-ZTC-IB-850 at 298 K compared to ZTC (see Figure 7.5). Furthermore, the adsorbed methane phase is observed to be densified on teh surface of N-ZTCs compared to that on archetypical ZTC. Therefore, the predictions of recent computational results[167] have been supported by the experimental results reported herein.

7.4 Conclusions and Outlook

The above results show that the combination of FA polymerization and acetonitrile CVD results in N-ZTCs with primarily NC_3-type nitrogen dopant environments, which have been computationally identified as sites of interested for increasing methane binding energy.

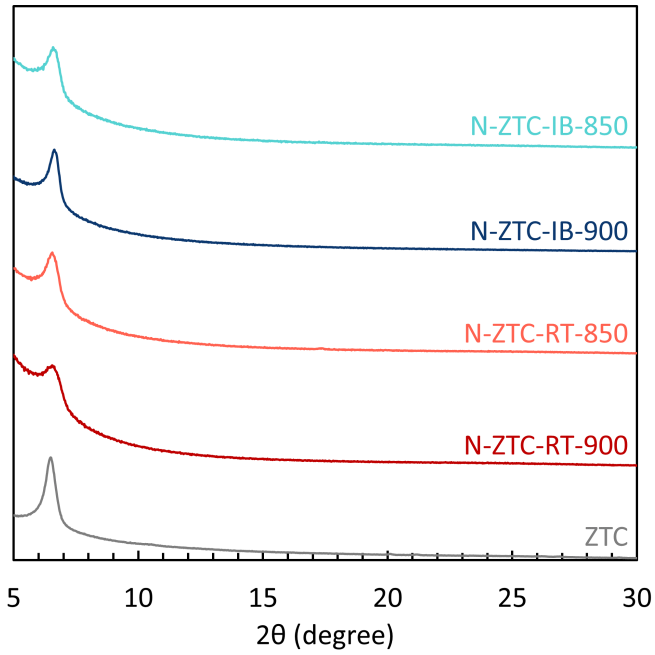

Figure 7.4: XRD patterns of ZTC and N-ZTCs.

However, the resultant N-ZTCs do not attain the same template fidelity as archetypical ZTCs. This may indicate that the mixture of FA and acetonitrile is not chemically compatible in high-quality ZTC synthesis, and N-ZTCs may require a new combination of impregnation and CVD precursors in the future, in addition to the optimization of other synthesis parameters.

In general, heat-treatment temperatures must be high enough to firm up the carbon structure after CVD without decomposing the zeolite template itself (Figure 2.4). However, the deposition temperature of acetonitrile (800 °C) is higher than most other CVD carbon precursor gases, leading to a small temperature difference between CVD and heat-treatment. This suggests that a more catalytically active zeolite may be required for acetonitrile deposition to create a larger temperature gap between deposition and annealing. Examples of this would be Li- or H-exchanged zeolites, or a zeolite with lower Si:Al ratio. Regardless

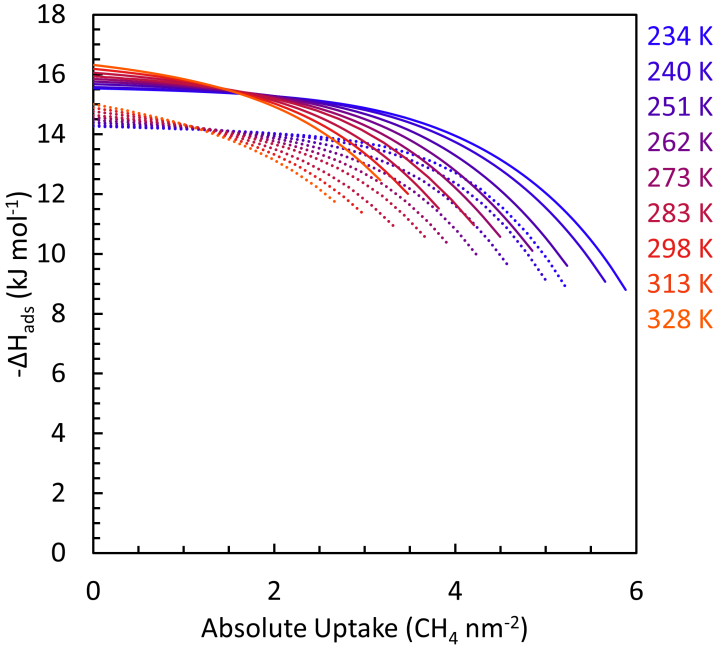

Figure 7.5: Isosteric enthalpy of adsorption of methane as a function of calculated absolute uptake determined using double-Langmuir fits on ZTC (dashed lines) and N-ZTC-IB-850 (solid lines).

of the improvements required for future N-ZTC synthesis, the methane adsorption isotherms measured in this work support the predictions of Rowsey et al. that NC_3-type nitrogen dopants can increase methane binding energy on open carbon surfaces.

Table 7.1: Nitrogen content, graphic nitrogen doping, SPD, and BET SA for ZTC and N-ZTCs.

Material	**N-content (at%)**	**Graphitic Nitrogen Doping**	**BET SA (m^2 g^{-1})**	**SPD_{cell} (g_{ZTC} $g^{-1}{}_{SiO_2}$)**
N-ZTC-IB-850	8.8	83%	2370	0.41
N-ZTC-IB-900	4.1	81%	2746	0.41
N-ZTC-RT-850	6.0	84%	2301	0.42
N-ZTC-RT-900	6.6	76%	2368	0.42
ZTC	-	-	3228	0.37

CHAPTER EIGHT

CONCLUSION

8.1 Summary of Results

In this work, computational and experimental efforts were blended to elucidate and alter ZTC structure. Through these efforts, Nishihara Model II+ was identified as an experimentally relevant ZTC atomistic model, confirming that ZTCs are made of open-blade struts with large amount of edge sites. From magnetic measurements and computational studies, it was determined that ZTCs are paramagnetic; this is not unique for porous carbon materials, but the number of unpaired electrons present is anomalously high. Extensive investigations of the origin of this anomaly showed that ZTCs contain a significant amount of zigzag edges which can energetically stabilize unpaired electrons. New routes to ZTCs with higher templating accuracy were also explored by exploiting cation-π interactions between the carbon precursor and the zeolite template. In the hope of controlling structural packing density, a series of Li-, Na-, and K-exchanged zeolite Y templates were used to synthesize corresponding ZTC samples. As predicted, decreased template fidelity was observed as the interaction strength decreased when weaker cation-π interactions were introduced (e.g., for KY-templated ZTCs). The opposite trend, though less poignant, was also observed for the LiY-templated ZTCS. Even though archeytypical ZTCs do not resemble schwarzite materials, they do exhibit a pore size and open-blade surface that is optimal for methane storage. Computational efforts identified that methane binding could be enhanced by adsorption above NC_3-type nitrogen environments. Nitrogen-doped ZTCs were synthesized using a two-step method, first impregnating with FA followed by further carbon deposition of acetonitrile, resulting in a maximum of 8.8 at % nitrogen with 83% of the nitrogen-dopants present in a graphitic-type dopant environment. These early N-ZTCs show promise as methane

storage materials, exhibiting a 1.3 kJ mol^{-1} increase in methane binding energy compared to nitrogen-free ZTC.

8.2 Future Work

Atomistic models of ZTC materials have revealed important structural features of ZTCs, such as open-blade struts with a large number of edge-sites and atomistic disorder. Future atomistic **FAU**-ZTC models should be developed that incorporate both the amorphous nature of Tanaka Model IV while also incorporating oxygen-bearing functionalities as in Nishihara Model II+.

The nature of unpaired electrons in zigzag edge-terminated blade structures head further investigation at varying levels of theory. This work should include both periodic and molecular models to verify that the results reported herein are not an artefact of the method used.

Lithium exchange of zeolite Y may be the key to converting an open-blade ZTC into a closed-tube schwarzite-like material. Future work should be carried out to optimize ZTC synthesis conditions using LiY zeolite templates, to truly assess the catalytic capability of LiY. In addition, the use of other Li salts should be explored to achieve the highest possible exchange.

N-ZTCs, while exhibiting lower template fidelity than archetypical ZTC, still exhibited an increase in methane binding energy. Future work should be focused on developing a nitrogen-doping procedure which can form a free standing framework without the use of a high heat-treatment temperature. This may require the use of different liquid impregnation and/or CVD precursors, or the use of a more catalytically active zeolite template to reduce the CVD temperature of acetonitrile.

It is the author's hope that the work described herein will lay the groundwork for the future development of new ZTC materials for energy storage applications and beyond.

REFERENCES CITED

[1] Smalley R. E. Discovering the fullerenes. *Rev. Mod. Phys.*, 69(3):723–730, 1997.

[2] Kroto H. W., Heath J. R., O'Brien S. C., Curl R. F., and Smalley R. E. C_{60}: Buckminsterfullerene. *Nature*, 318(6042):162–163, 1985.

[3] Hirsch A. The era of carbon allotropes. *Nat. Mater.*, 9(11):868, 2010.

[4] Iijima S. Helical microtubules of graphitic carbon. *Nature*, 354(6348):56–58, 1991.

[5] Novoselov K. S., Geim A. K., Morozov S. V., Jiang D., Zhang Y., Dubonos S. V., Grigorieva I. V., and Firsov A. A. Electric Field Effect in Atomically Thin Carbon Films. *Science*, 306(5696):666–669, 2004.

[6] Samsonov G. V. *Mechanical Properties of the Elements*, pages 387–446. Springer, 1968.

[7] Lee C., Wei X., Kysar J. W., and Hone J. Measurement of the Elastic Properties and Intrinsic Strength of Monolayer Graphene. *Science*, 321(5887):385–388, 2008.

[8] Zhang Y., Tan Y.-W., Stormer H. L., and Kim P. Experimental observation of the quantum Hall effect and Berry's phase in graphene. *Nature*, 438(7065):201–204, 2005.

[9] Jones D. Ghostly graphite. *Nature*, 351(6327):526–526, 1991.

[10] Roberts S. David E. H. Jones, Scientist Whose Alter Ego Challenged Conventions, Dies at 79. *The New York Times*, page 6, Jun 2017.

[11] Mackay A. L. and Terrones H. Diamond from graphite. *Nature*, 352(6338):762, 1991.

[12] Lenosky T., Gonze X., Teter M., and Elser V. Energetics of negatively curved graphitic carbon. *Nature*, 355(6358):333–335, 1992.

[13] Schwarz H. A. *Gesammelte Mathematische Abhandlungen*, volume 1. J. Springer, 1890.

[14] Schoen A. H. Infinite Periodic Minimal Surfaces without Self-Intersections (NASA Electronics Research Center, Cambridge, MA). Report, Technical Report NASA TN D-5541, C-98, 1970.

[15] Townsend S. J., Lenosky T. J., Muller D. A., Nichols C. S., and Elser V. Negatively curved graphitic sheet model of amorphous carbon. *Phys. Rev. Lett.*, 69(6):921–924, 1992.

[16] Vanderbilt D. and Tersoff J. Negative-curvature fullerene analog of C_{60}. *Phys. Rev. Lett.*, 68(4):511, 1992.

[17] O'Keeffe M., Adams G. B., and Sankey O. F. Predicted new low energy forms of carbon. *Phys. Rev. Lett.*, 68(15):2325, 1992.

[18] Phillips R., Drabold D. A., Lenosky T., Adams G. B., and Sankey O. F. Electronic structure of schwarzite. *Phys. Rev. B*, 46(3):1941–1943, 1992.

[19] Terrones H. and Mackay A. L. The geometry of hypothetical curved graphite structures. *Carbon*, 30(8):1251–1260, 1992.

[20] Terrones H. and Mackay A. L. Triply periodic minimal surfaces decorated with curved graphite. *Chemical Physics Letters*, 207(1):45–50, 1993.

[21] Terrones H. and Mackay A. L. Hypothetical curved graphite. *Nanostruct. Mater.*, 3(1-6):319–329, 1993.

[22] Lherbier A., Terrones H., and Charlier J.-C. Three-dimensional massless Dirac fermions in carbon schwarzites. *Phys. Rev. B*, 90(12):125434, 2014.

[23] Felix L. C., Woellner C. F., and Galvao D. S. Mechanical and energy-absorption properties of schwarzites. *Carbon*, 157:670–680, 2020.

[24] Yang W., Li Z.-M., Shi W., Xie B.-H., and Yang M.-B. Review on auxetic materials. *J. Mater. Sci.*, 39(10):3269–3279, 2004.

[25] Yanping J. and Hong H. A review on auxetic structures and polymeric materials. *Sci. Res. Essays*, 5(10):1052–1063, 2010.

[26] Rode A. V., Hyde S. T., Gamaly E. G., Elliman R. G., McKenzie D. R., and Bulcock S. Structural analysis of a carbon foam formed by high pulse-rate laser ablation. *Appl. Phys. A-Mater.*, 69(1):S755–S758, 1999.

[27] Cheung K. Y. and Miao Q. A ketone-functionalized aromatic saddle as a potential building block for negatively curved carbon nanobelts. *Chinese Chem. Lett.*, 2019.

[28] Nishihara H. and Kyotani T. Zeolite-templated carbons–three-dimensional microporous graphene frameworks. *Chem. Commun.*, 54(45):5648–5673, 2018.

[29] Kyotani T., Nagai T., Inoue S., and Tomita A. Formation of New Type of Porous Carbon by Carbonization in Zeolite Nanochannels. *Chem. Mater.*, 9(2):609–615, 1997.

[30] Ma Z., Kyotani T., and Tomita A. Preparation of a high surface area microporous carbon having the structural regularity of Y zeolite. *Chem. Commun.*, (23):2365–2366, 2000.

[31] Ma Z., Kyotani T., Liu Z., Terasaki O., and Tomita A. Very High Surface Area Microporous Carbon with a Three-Dimensional Nano-Array Structure: Synthesis and Its Molecular Structure. *Chem. Mater.*, 13(12):4413–4415, 2001.

[32] Baerlocher Ch. and McCusker L.B. Database of Zeolite Structures. `http://www.iza-structure.org/databases`.

[33] Braun E., Lee Y., Moosavi S. M., Barthel S., Mercado R., Baburin I. A., Proserpio D. M., and Smit B. Generating carbon schwarzites via zeolite-templating. *P. Natl. Acad. Sci.*, 115(35):E8116, 2018.

[34] Tanaka H., Seto T., Nishihara H., Kyotani T., and Miyahara M. T. Synthesis of zeolite-templated carbons for methane storage: A molecular simulation study. *TANSO*, 2018(285):197–203, 2018.

[35] Barata-Rodrigues P. M., Mays T. J., and Moggridge G. D. Structured carbon adsorbents from clay, zeolite and mesoporous aluminosilicate templates. *Carbon*, 41(12):2231–2246, 2003.

[36] Kyotani T., Ma Z., and Tomita A. Template synthesis of novel porous carbons using various types of zeolites. *Carbon*, 41(7):1451–1459, 2003.

[37] Tosheva L., Parmentier J., Valtchev V., Vix-Guterl C., and Patarin J. Carbon spheres prepared from zeolite Beta beads. *Carbon*, 43(12):2474–2480, 2005.

[38] Yang Z., Xia Y., and Mokaya R. Enhanced hydrogen storage capacity of high surface area zeolite-like carbon materials. *J. Amer. Chem. Soc.*, 129(6):1673–1679, 2007.

[39] Pacuła A. and Mokaya R. Synthesis and High Hydrogen Storage Capacity of Zeolite-Like Carbons Nanocast Using As-Synthesized Zeolite Templates. *J. Phys. Chem. C*, 112(7):2764–2769, 2008.

[40] Nishihara H., Itoi H., Kogure T., Hou P.-X., Touhara H., Okino F., and Kyotani T. Investigation of the Ion Storage/Transfer Behavior in an Electrical Double-Layer Capacitor by Using Ordered Microporous Carbons as Model Materials. *Chem.-Euro. J.*, 15(21):5355–5363, 2009.

[41] Parmentier J., Valtchev V., Gaslain F., Tosheva L., Ducrot-Boisgontier C., Möller J., Patarin J., and Vix-Guterl C. Effect of the zeolite crystal size on the structure and properties of carbon replicas made by a nanocasting process. *Carbon*, 47(4):1066–1073, 2009.

[42] Xu H., Gao Q., Guo H., and Wang H. Hierarchical porous carbon obtained using the template of NaOH-treated zeolite β and its high performance as supercapacitor. *Micropor. Mesopor. Mat.*, 133(1):106–114, 2010.

[43] Kim K., Choi M., and Ryoo R. Ethanol-based synthesis of hierarchically porous carbon using nanocrystalline beta zeolite template for high-rate electrical double layer capacitor. *Carbon*, 60:175–185, 2013.

[44] Xia Y., Yang Z., Gou X., and Zhu Y. A simple method for the production of highly ordered porous carbon materials with increased hydrogen uptake capacities. *Int. J. Hydrogen Energ.*, 38(12):5039–5052, 2013.

[45] Matei Ghimbeu C., Guerin K., Dubois M., Hajjar-Garreau S., and Vix-Guterl C. Insights on the reactivity of ordered porous carbons exposed to different fluorinating agents and conditions. *Carbon*, 84:567–583, 2015.

[46] Kim K., Lee T., Kwon Y., Seo Y., Song J., Park J. K., Lee H., Park J. Y., Ihee H., Cho S. J., and Ryoo R. Lanthanum-catalysed synthesis of microporous 3D graphene-like carbons in a zeolite template. *Nature*, 535:131, 2016.

[47] Wang J., Liu Z., Dong X., Hsiung C.-E., Zhu Y., Liu L., and Han Y. Microporous cokes formed in zeolite catalysts enable efficient solar evaporation. *J. Mater. Chem. A*, 5(15):6860–6865, 2017.

[48] Choi S., Alkhabbaz M. A., Wang Y., Othman R. M., and Choi M. Unique thermal contraction of zeolite-templated carbons enabling micropore size tailoring and its effects on methane storage. *Carbon*, 141:143–153, 2019.

[49] Noh H., Choi S., Kim H. G., Choi M., and Kim H.-T. Size Tunable Zeolite-Templated Carbon as Microporous Sulfur Host for Lithium-Sulfur Batteries. *ChemElectroChem*, 6(2):558–565, 2019.

[50] Park H., Terhorst S. K., Bera R. K., and Ryoo R. Template dissolution with NaOH–HCl in synthesis of zeolite-templated carbons: Effects on oxygen functionalization and electrical energy storage characteristics. *Carbon*, 2019.

[51] Lee S.-K., Park H., Yoon J. W., Kim K., Cho S. J., Maurin G., Ryoo R., and Chang J.-S. Microporous 3D Graphene-like Zeolite-Templated Carbons for Preferential Adsorption of Ethane. *ACS Appl. Mater. Inter.*, 12(25):28484–28495, 2020.

[52] Aumond T., Batonneau-Gener I., Pouilloux Y., Pinard L., Wisser D., Moreau M., Vezin H., Moissette A., and Sachse A. How do zeolite-templated carbons grow? *Mater. Today Chem.*, 26:101053, 2022.

[53] Gaslain F. O. M., Parmentier J., Valtchev V. P., and Patarin J. First zeolite carbon replica with a well resolved X-ray diffraction pattern. *Chem. Commun.*, (9):991–993, 2006.

[54] Wang L. and Yang R. T. Hydrogen Storage Properties of Carbons Doped with Ruthenium, Platinum, and Nickel Nanoparticles. *J. Phys. Chem. C*, 112(32):12486–12494, 2008.

[55] Ducrot-Boisgontier C., Parmentier J., Delmotte L., and Patarin J. Influence of chemical vapour infiltration conditions of acetylene on the structural and textural properties of **EMT**-type zeolite nanocasted carbon replica. *J. Mater. Sci.*, 44(24):6571–6575, 2009.

[56] Ducrot-Boisgontier C., Parmentier J., and Patarin J. Influence of the carbon precursors on the structural properties of **EMT**-type nanocasted-carbon replicas. *Micropor. Mesopor. Mat.*, 126(1):101–106, 2009.

[57] Builes S., Roussel T., Ghimbeu C. M., Parmentier J., Gadiou R., Vix-Guterl C., and Vega L. F. Microporous carbon adsorbents with high CO_2 capacities for industrial applications. *Phys. Chem. Chem. Phys.*, 13(35):16063–16070, 2011.

[58] Parmentier J., Gaslain F. O. M., Ersen O., Centeno T. A., and Solovyov L. A. Structure and Sorption Properties of a Zeolite-Templated Carbon with the **EMT** Structure Type. *Langmuir*, 30(1):297–307, 2014.

[59] Frising T. and Leflaive P. Extraframework cation distributions in X and Y faujasite zeolites: A review. *Micropor. Mesopor. Mat.*, 114(1):27–63, 2008.

[60] Julbe A. and Drobek M. *Zeolite Y: Type*, pages 1–2. Springer Berlin Heidelberg, Berlin, Heidelberg, 2016.

[61] Itoi H., Kasai Y., Morishita K., Suzuki R., Gotoh Y., Matsuoka C., Miyaji M., Hirade R., Tanabe Y., Iwata H., and Ohzawa Y. Facile synthesis of high surface area zeolite-templated carbons using divinylbenzene and propylene as carbon sources. *Micropor. Mesopor. Mat.*, 326:111378, 2021.

[62] Itoi H., Hirade R., Matsuoka C., Kasai Y., Morishita K., Gotoh Y., Iwata H., and Ohzawa Y. Facile Synthesis of High Surface Area Zeolite-Templated Carbon from Sugars and Propylene. *ACS Sustainable Chem. Eng.*, 2022.

[63] Lv Y., Wu Z., Fang Y., Qian X., Asiri A. M., Tu B., and Zhao D. Hierarchical mesoporous/microporous carbon with graphitized frameworks for high-performance lithium-ion batteries. *APL Mater.*, 2(11):113302, 2014.

[64] Hou P.-X., Yamazaki T., Orikasa H., and Kyotani T. An easy method for the synthesis of ordered microporous carbons by the template technique. *Carbon*, 43(12):2624–2627, 2005.

[65] Paredes J. I., Martínez-Alonso A., Hou P. X., Kyotani T., and Tascón J. M. D. Imaging the structure and porosity of active carbons by scanning tunneling microscopy. *Carbon*, 44(12):2469–2478, 2006.

[66] Nishihara H., Itoi H., Kogure T., Hou P.-X., Touhara H., Okino F., and Kyotani T. Investigation of the Ion Storage/Transfer Behavior in an Electrical Double-Layer Capacitor by Using Ordered Microporous Carbons as Model Materials. *Chem.-Eur. J.*, 15(21):5355–5363, 2009.

[67] Ducrot-Boisgontier C., Parmentier J., Faour A., Patarin J. l., and Pirngruber G. D. **FAU**-type zeolite nanocasted carbon replicas for CO_2 adsorption and hydrogen purification. *Energ. Fuel*, 24(6):3595–3602, 2010.

[68] Kajdos A., Kvit A., Jones F., Jagiello J., and Yushin G. Tailoring the pore alignment for rapid ion transport in microporous carbons. *J. Am. Chem. Soc.*, 132(10):3252–3253, 2010.

[69] Takai K., Suzuki T., Enoki T., Nishihara H., and Kyotani T. Structure and magnetic properties of curved graphene networks and the effects of bromine and potassium adsorption. *Phys. Rev. B*, 81(20):205420, 2010.

[70] Takai K., Suzuki T., Enoki T., Nishihara H., and Kyotani T. Fabrication and characterization of magnetic nanoporous zeolite templated carbon. *J. Phys. Chem. Solids*, 71(4):565–568, 2010.

[71] Yang Y., Tang L., Burke N., and Chiang K. Nanoporous carbon supported metal particles: their synthesis and characterisation. *J. Nanopart. Res.*, 14(8):1028, 2012.

[72] Nueangnoraj K., Nishihara H., Imai K., Itoi H., Ishii T., Kiguchi M., Sato Y., Terauchi M., and Kyotani T. Formation of crosslinked-fullerene-like framework as negative replica of zeolite Y. *Carbon*, 62:455–464, 2013.

[73] Cai J., Li L., Lv X., Yang C., and Zhao X. Large Surface Area Ordered Porous Carbons via Nanocasting Zeolite 10X and High Performance for Hydrogen Storage Application. *ACS Appl. Mater. Inter.*, 6(1):167–175, 2014.

[74] Choi S., Kim H., Lee S., Wang Y., Ercan C., Othman R., and Choi M. Large-scale synthesis of high-quality zeolite-templated carbons without depositing external carbon layers. *Chem. Eng. J.*, 280:597–605, 2015.

[75] Moon J. S., Kim H., Lee D.-C., Lee J. T., and Yushin G. Increasing Capacitance of Zeolite-Templated Carbons in Electric Double Layer Capacitors. *J. Electrochem. Soc.*, 162(5):A5070–A5076, 2015.

[76] Nishihara H., Imai K., Itoi H., Nomura K., Takai K., and Kyotani T. Formation mechanism of zeolite-templated carbons. *TANSO*, 2017(280):169–174, 2017.

[77] Boonyoung P., Kasukabe T., Hoshikawa Y., Berenguer-Murcia Á., Cazorla-Amorós D., Boekfa B., Nishihara H., Kyotani T., and Nueangnoraj K. A Simple "Nano-Templating" Method Using Zeolite Y Toward the Formation of Carbon Schwarzites. *Front. Mater.*, 6:104, 2019.

[78] Nomura K., Nishihara H., Yamamoto M., Gabe A., Ito M., Uchimura M., Nishina Y., Tanaka H., Miyahara M. T., and Kyotani T. Force-driven reversible liquid–gas phase transition mediated by elastic nanosponges. *Nat. Commun.*, 10(1):1–10, 2019.

[79] Liu Y., Wang J., Serageldin M. A., Wang T., and Pan W.-P. Carbon deposition mechanism and structural changes for zeolite-templated carbons. *Micropor. Mesopor. Mat.*, 324:111311, 2021.

[80] Yang G., Li L., Liu H., Cheng Y., Chen Y., and Li X. Metal ion (Ca^{2+}, Mg^{2+}, Zn^{2+}) catalyzed synthesis of high-quality zeolite templated carbon. *Micropor. Mesopor. Mat.*, page 111860, 2022.

[81] Garsuch A. and Klepel O. Synthesis of ordered carbon replicas by using Y-zeolite as template in a batch reactor. *Carbon*, 43(11):2330–2337, 2005.

[82] Garsuch A., Klepel O., Sattler R. R., Berger C., Gläser R., and Weitkamp J. Synthesis of a carbon replica of zeolite Y with large crystallite size. *Carbon*, 44(3):593–596, 2006.

[83] Yang Z., Xia Y., Sun X., and Mokaya R. Preparation and Hydrogen Storage Properties of Zeolite-Templated Carbon Materials Nanocast via Chemical Vapor Deposition: Effect of the Zeolite Template and Nitrogen Doping. *J. Phys. Chem. B*, 110:18424–18431, 2006.

[84] Xia Y., Walker G. S., Grant D. M., and Mokaya R. Hydrogen storage in high surface area carbons: experimental demonstration of the effects of nitrogen doping. *J. Am. Chem. Soc.*, 131(45):16493–16499, 2009.

[85] Xia Y., Yang Z., and Mokaya R. CVD Nanocasting Routes to Zeolite-Templated Carbons for Hydrogen Storage. *Chem. Vap. Deposition*, 16(10-12):322–328, 2010.

[86] Masika E. and Mokaya R. Preparation of ultrahigh surface area porous carbons templated using zeolite 13X for enhanced hydrogen storage. *Prog. Nat. Sci.*, 23(3):308–316, 2013.

[87] Masika E. and Mokaya R. Exceptional gravimetric and volumetric hydrogen storage for densified zeolite templated carbons with high mechanical stability. *Energ. Environ. Sci.*, 7(1):427–434, 2014.

[88] Balahmar N., Lowbridge A. M., and Mokaya R. Templating of carbon in zeolites under pressure: synthesis of pelletized zeolite templated carbons with improved porosity and packing density for superior gas (CO_2 and H_2) uptake properties. *J. Mater. Chem. A*, 4(37):14254–14266, 2016.

[89] Kim K., Kwon Y., Lee T., Cho S. J., and Ryoo R. Facile large-scale synthesis of three-dimensional graphene-like ordered microporous carbon via ethylene carbonization in CaX zeolite template. *Carbon*, 118:517–523, 2017.

[90] Lee H., Kim K., Kang S.-H., Kwon Y., Kim J. H., Kwon Y.-K., Ryoo R., and Park J. Y. Extremely high electrical conductance of microporous 3D graphene-like zeolite-templated carbon framework. *Sci. Rep.-UK*, 7(1):11460, 2017.

[91] Park H., Bang J., Han S. W., Bera R. K., Kim K., and Ryoo R. Synthesis of zeolite-templated carbons using oxygen-containing organic solvents. *Micropor. Mesopor. Mat.*, 318:111038, 2021.

[92] Choi W., Bera R. K., Han S. W., Park H., Go T. W., Choi M., Ryoo R., and Park J. Y. Doping effect of zeolite-templated carbon on electrical conductance and supercapacitance properties. *Carbon*, 193:42–50, 2022.

[93] Ma Z., Kyotani T., and Tomita A. Synthesis methods for preparing microporous carbons with a structural regularity of zeolite Y. *Carbon*, 40(13):2367–2374, 2002.

[94] Paredes J. I., Martínez-Alonso A., Yamazaki T., Matsuoka K., Tascón J. M. D., and Kyotani T. Structural Investigation of Zeolite-templated, Ordered Microporous Carbon by Scanning Tunneling Microscopy and Raman Spectroscopy. *Langmuir*, 21(19):8817–8823, 2005.

[95] Armandi M., Bonelli B., Bottero I., Areán C. O., and Garrone E. Synthesis and characterization of ordered porous carbons with potential applications as hydrogen storage media. *Micropor. Mesopor. Mat.*, 103(1):150–157, 2007.

[96] Chen L., Singh R. K., and Webley P. Synthesis, characterization and hydrogen storage properties of microporous carbons templated by cation exchanged forms of zeolite Y with propylene and butylene as carbon precursors. *Micropor. Mesopor. Mat.*, 102(1):159–170, 2007.

[97] Coker E. N., Steen W. A., Miller J. T., Kropf A. J., and Miller J. E. Nanostructured Pt/C electrocatalysts with high platinum dispersions through zeolite-templating. *Micropor. Mesopor. Mat.*, 101(3):440–444, 2007.

[98] Hou P.-X., Orikasa H., Itoi H., Nishihara H., and Kyotani T. Densification of ordered microporous carbons and controlling their micropore size by hot-pressing. *Carbon*, 45(10):2011–2016, 2007.

[99] Roussel T., Didion A., Pellenq R. J. M., Gadiou R., Bichara C., and Vix-Guterl C. Experimental and Atomistic Simulation Study of the Structural and Adsorption Properties of Faujasite ZeoliteTemplated Nanostructured Carbon Materials. *J. Phys. Chem. C*, 111(43):15863–15876, 2007.

[100] Ji L., Liu F., Xu Z., Zheng S., and Zhu D. Zeolite-Templated Microporous Carbon As a Superior Adsorbent for Removal of Monoaromatic Compounds from Aqueous Solution. *Environ. Sci. Technol.*, 43(20):7870–7876, 2009.

[101] Nishihara H., Hou P.-X., Li L.-X., Ito M., Uchiyama M., Kaburagi T., Ikura A., Katamura J., Kawarada T., Mizuuchi K., and Kyotani T. High-Pressure Hydrogen Storage in Zeolite-Templated Carbon. *J. Phys. Chem. C*, 113(8):3189–3196, 2009.

[102] Nishihara H., Yang Q.-H., Hou P.-X., Unno M., Yamauchi S., Saito R., Paredes J. I., Martínez-Alonso A., Tascón J. M. D., Sato Y., Terauchi M., and Kyotani T. A possible buckybowl-like structure of zeolite templated carbon. *Carbon*, 47(5):1220–1230, 2009.

[103] Yang Y.-X., Bourgeois L., Zhao C., Zhao D., Chaffee A., and Webley P. A. Ordered micro-porous carbon molecular sieves containing well-dispersed platinum nanoparticles for hydrogen storage. *Micropor. Mesopor. Mat.*, 119(1):39–46, 2009.

[104] Itoi H., Nishihara H., Kogure T., and Kyotani T. Three-Dimensionally Arrayed and Mutually Connected 1.2-nm Nanopores for High-Performance Electric Double Layer Capacitor. *J. Am. Chem. Soc.*, 133(5):1165–1167, 2011.

[105] Stadie N. P., Vajo J. J., Cumberland R. W., Wilson A. A., Ahn C. C., and Fultz B. Zeolite-Templated Carbon Materials for High-Pressure Hydrogen Storage. *Langmuir*, 28(26):10057–10063, 2012.

[106] Yang S. J., Im J. H., Nishihara H., Jung H., Lee K., Kyotani T., and Park C. R. General Relationship between Hydrogen Adsorption Capacities at 77 and 298 K and Pore Characteristics of the Porous Adsorbents. *J. Phys. Chem. C*, 116(19):10529–10540, 2012.

[107] Yang H. N., Lee J. Y., Na Y., Yi S. C., and Kim W. J. Effect of functionalization for carbon molecular sieve (CMS) synthesized using zeolite template on the incorporation of Pt nanoparticle and performance of the electrodes in PEMFC. *Micropor. Mesopor. Mat.*, 152:148–156, 2012.

[108] Berenguer R., Nishihara H., Itoi H., Ishii T., Morallón E., Cazorla-Amorós D., and Kyotani T. Electrochemical generation of oxygen-containing groups in an ordered microporous zeolite-templated carbon. *Carbon*, 54:94–104, 2013.

[109] Ito M., Nishihara H., Yamamoto K., Itoi H., Tanaka H., Maki A., Miyahara M. T., Yang S. J., Park C. R., and Kyotani T. Reversible Pore Size Control of Elastic Microporous Material by Mechanical Force. *Chem.-Eur. J.*, 19(39):13009–13016, 2013.

[110] Yang H. N., Park S. H., Lee D. C., Yi S. C., and Kim W. J. Electrochemical properties of hybrid typed electrocatalyst using Pt/carbon molecular sieve synthesized by zeolite template and Pt carbon black. *Micropor. Mesopor. Mat.*, 172:161–166, 2013.

[111] Nishihara H., Ittisanronnachai S., Itoi H., Li L.-X., Suzuki K., Nagashima U., Ogawa H., Kyotani T., and Ito M. Experimental and Theoretical Studies of Hydrogen/Deuterium Spillover on Pt-Loaded Zeolite-Templated Carbon. *J. Phys. Chem. C*, 118(18):9551–9559, 2014.

[112] Chung P.-W., Yabushita M., To A. T., Bae Y., Jankolovits J., Kobayashi H., Fukuoka A., and Katz A. Long-Chain Glucan Adsorption and Depolymerization in Zeolite-Templated Carbon Catalysts. *ACS Catal.*, 5(11):6422–6425, 2015.

[113] Itoi H., Nishihara H., and Kyotani T. Effect of heteroatoms in ordered microporous carbons on their electrochemical capacitance. *Langmuir*, 32(46):11997–12004, 2016.

[114] Panich A. M., Osipov V. Y., Nishihara H., and Kyotani T. Nuclear magnetic resonance study of zeolite-templated carbon. *Synth. Met.*, 221:149–152, 2016.

[115] Stadie N. P., Wang S., Kravchyk K. V., and Kovalenko M. V. Zeolite-Templated Carbon as an Ordered Microporous Electrode for Aluminum Batteries. *ACS Nano*, 11(2):1911–1919, 2017.

[116] Dubey R. J. C., Colijn T., Aebli M., Hanson E. E., Widmer R., Kravchyk K. V., Kovalenko M. V., and Stadie N. P. Zeolite-templated carbon as a stable, high power magnesium-ion cathode material. *ACS Appl. Mater. Inter.*, 11(43):39902–39909, 2019.

[117] Ishii T., Horiuchi A., and Ozaki J.-i. An Ion-Sensitive Field Effect Transistor Using Metal-Coordinated Zeolite-Templated Carbons as a Three-Dimensional Graphene Nanoribbon Network. *Front. Mater.*, 6, 2019.

[118] Taylor E. E., Garman K., and Stadie N. P. Atomistic Structures of Zeolite-Templated Carbon. *Chem. Mater.*, 32(7):2742–2752, 2020.

[119] Gabe A., Ouzzine M., Taylor E. E., Stadie N. P., Uchiyama N., Kanai T., Nishina Y., Tanaka H., Pan Z.-Z., Kyotani T., and Nishihara H. High-density monolithic pellets of double-sided graphene fragments based on zeolite-templated carbon. *J. Mater. Chem. A*, 2021.

[120] Youn H.-K., Kim J., Chandrasekar G., Jin H., and Ahn W.-S. High pressure carbon dioxide adsorption on nanoporous carbons prepared by Zeolite Y templating. *Mater. Lett.*, 65(12):1772–1774, 2011.

[121] Puziy A. M., Poddubnaya O. I., Gawdzik B., Sobiesiak M., Reinish C. A., Tsyba M. M., Segeda T. P., and Danylenko M. I. Nanostructured carbons for solid phase extraction. *Appl. Surf. Sci.*, 256(17):5216–5220, 2010.

[122] Rouquerol J., Rouquerol F., Llewellyn P., Maurin G., and Sing K. S. W. *Adsorption by powders and porous solids: principles, methodology and applications*. Academic press, 2013.

[123] Macrae C. F., Edgington P. R., McCabe P., Pidcock E., Shields G. P., Taylor R., Towler M., and Streek J. V. D. Mercury: visualization and analysis of crystal structures. *J. Appl. Crystallogr.*, 39(3):453–457, 2006.

[124] Willems T. F., Rycroft C. H., Kazi M., Meza J. C., and Haranczyk M. Algorithms and tools for high-throughput geometry-based analysis of crystalline porous materials. *Micropor. Mesopor. Mat.*, 149(1):134–141, 2012.

[125] Ongari D., Boyd P. G., Barthel S., Witman M., Haranczyk M., and Smit B. Accurate Characterization of the Pore Volume in Microporous Crystalline Materials. *Langmuir*, 33(51):14529–14538, 2017.

[126] Palmer D. C. Visualization and analysis of crystal structures using CrystalMaker software. *Z. Kristallogr. Cryst. Mat.*, 230(9-10):559–572, 2015.

[127] Roussel T., Jagiello J., Pellenq R. J. M., Thommes M., and Bichara C. Testing the feasibility of using the density functional theory route for pore size distribution calculations of ordered microporous carbons. *Mol. Simulat.*, 32(7):551–555, 2006.

[128] Nishihara H., Fujimoto H., Itoi H., Nomura K., Tanaka H., Miyahara M. T., Bonnaud P. A., Miura R., Suzuki A., Miyamoto N., Hatakeyama N., Miyamoto A., Ikeda K., Otomo T., and Kyotani T. Graphene-based ordered framework with a diverse range of carbon polygons formed in zeolite nanochannels. *Carbon*, 129:854–862, 2018.

[129] Gabe A., Mostazo-López M. J., Salinas-Torres D., Morallón E., and Cazorla-Amorós D. *Synthesis of conducting polymer/carbon material composites and their application in electrical energy storage*, pages 173–209. Elsevier, 2017.

[130] Itoi H., Nishihara H., Ishii T., Nueangnoraj K., Berenguer-Betrián R., and Kyotani T. Large Pseudocapacitance in Quinone-Functionalized Zeolite-Templated Carbon. *B. Chem. Soc. Jpn.*, 87(2):250–257, 2014.

[131] Kumar A., Lobo R. F., and Wagner N. J. Porous amorphous carbon models from periodic Gaussian chains of amorphous polymers. *Carbon*, 43(15):3099–3111, 2005.

[132] Jain S. K., Gubbins K. E., Pellenq R. J. M., and Pikunic J. P. Molecular Modeling and Adsorption Properties of Porous Carbons. *Carbon*, 44(12):2445–2451, 2006.

[133] Jain S. K., Pellenq R. J. M., Pikunic J. P., and Gubbins K. E. Molecular Modeling of Porous Carbons Using the Hybrid Reverse Monte Carlo Method. *Langmuir*, 22(24):9942–9948, 2006.

[134] Palmer J. C., Brennan J. K., Hurley M. M., Balboa A., and Gubbins K. E. Detailed structural models for activated carbons from molecular simulation. *Carbon*, 47(12):2904–2913, 2009.

[135] Jain S. K. Molecular modeling of microporous and templated mesoporous carbons. 2008.

[136] Jain S. K., Pellenq R. J. M., Gubbins K. E., and Peng X. Molecular Modeling and Adsorption Properties of Ordered Silica-Templated CMK Mesoporous Carbons. *Langmuir*, 33(9):2109–2121, 2017.

[137] Hagelberg F. *Magnetism in Carbon Nanostructures*. Cambridge University Press, 2017.

[138] Makarova T. L. Magnetic properties of carbon structures. *Semiconductors*, 38:615–638, 2004.

[139] Coey J. M. D. *Magnetism of localized electrons on the atom*, pages 97–127. Cambridge University Press, 2012.

[140] Moorsom T., Rogers M., Scivetti I., Bandaru S., Teobaldi G., Valvidares M., Flokstra M., Lee S., Stewart R., Prokscha T., Gargiani P., Alosaimi N., Stefanou G., Ali M., Al Ma'mari F., Burnell G., Hickey B. J., and Cespedes O. Reversible spin storage in metal oxide—fullerene heterojunctions. *Science Advances*, 6(12), 2020.

[141] Lukose B., Kuc A., and Heine T. Stability and electronic properties of 3D covalent organic frameworks. *J. Mol. Model*, 19:2143–2148, 2013.

[142] J. Frenzel, A. F. Oliveira, N. Jardillier, T. Heine, and G Seifert. Semi-relativistic, self-consistent charge Slater-Koster tables for density-functional based tight-binding (DFTB) for materials science simlulations, 2004-2009.

[143] Terrones H. and Terrones M. Curved nanostructured materials. *New. J. Physics*, 5:126–126, 2003.

[144] Lukesh J. P. and Pauling L. C. The problem of the graphite structure. *Am. Mineral.*, 35(1-2):125, 1950.

[145] Dorset D. L. and McCourt M. P. Disorder and the molecular packing of C_{60} buckminsterfullerene: a direct electron-crystallographic analysis. *Acta Cryst.*, 50(3):344–351, 1994.

[146] Ikegami M and Nagaoka Y. Quantum mechanics of an electron on a curved surface. *Prog. Theor. Phys. Supp.*, 106:235–248, 1991.

[147] Fujita M., Wakabayashi K., Nakada K., and Kusakabe K. Peculiar localized state at zigzag graphite edge. *J. Phys. Soc. Jpn.*, 65(7):1920–1923, 1996.

[148] Yamashiro A., Shimoi Y., Harigaya K., and Wakabayshi K. Spin- and charge-polarized states in nanographene ribbons with zigzag edges. *Phys. Rev. B.*, 68:193410, 2003.

[149] Park N., Yoon M., Berber S., Ihm J., Osawa E., and Tománek D. Magnetism in All-Carbon Nanostructures with Negative Gaussian Curvature. *Phys. Rev. Lett.*, 91(23):237204, 2003.

[150] Isofort O., Bodenberg B., Fujara F., and Grosse R. Molecular dynamics of benzene in zeolite NaY studied by 2D deuteron NMR. *Chem. Phys. Lett.*, 288(1):71–76, 1998.

[151] Ma J. C. and Dougherty D. A. The cation π interaction. *Chem. Rev.*, 97(5):1303–1324, 1997.

[152] Maurin G., Belmabkhout Y., Pirngruber G., Gaberova L., and Llewellyn P. CO_2 adsorption in LiY and NaY at high temperature: molecular simulations compared to experiments. *Adsorption*, 13(5-6):453–460, 2007.

[153] Jeffroy M., Boutin A., and Fuchs A. H. Understanding the Equilibrium Ion Exchange Properties in Faujasite Zeolite from Monte Carlo Simulations. *J. Phys. Chem. B*, 115(50):15059–15066, 2011.

[154] Gaines P. Elemental Analysis of Zeolites, 2018.

[155] Yashima T., Suzuki H., and Hara N. Decomposition of 2-propanol over alkali cation exchanged zeolites. *J. Catal.*, 33(3):486–492, 1974.

[156] Ward J. W. A spectroscopic study of the surface of zeolite Y: the adsorption of pyridine. *J. Colloid Interface Sci.*, 28(2):269–278, 1968.

[157] Khabzina Y., Laroche C., Pagis C., and Farrusseng D. Monovalent and bivalent cations exchange isotherms for faujasites X and Y. *Phys. Chem. Chem. Phys.*, 19(26):17242–17249, 2017.

[158] Mortier W. J. and Bosmans H. J. Location of univalent cations in synthetic zeolites of the Y and X type with varying silicon to aluminum ratio. I. Hydrated potassium exchanged forms. *J. Phys. Chem.*, 75(21):3327–3334, 1971.

[159] Costenoble M. L., Mortier W. J., and Uytterhoeven J. B. Location of cations in synthetic zeolites X and Y. Part 4.—Exchange limiting factors for Ca^{2+} in zeolite Y. *J. Chem. Soc. Farad. T. 1*, 72(0):1877–1883, 1976.

[160] Ward J. W. Spectroscopic study of the surface of zeolite Y. II. Infrared spectra of structural hydroxyl groups and adsorbed water on alkali, alkaline earth, and rare earth ion-exchanged zeolites. *J. Phys. Chem.*, 72(12):4211–4223, 1968.

[161] Biggs F. and Lighthill R. Analytical approximations for x-ray cross sections III. Report, 1988-08-01 1988.

[162] Matranga K. R., Myers A. L., and Glandt E. D. Storage of natural gas by adsorption on activated carbon. *Chem. Eng. Sci.*, 47(7):1569–1579, 1992.

[163] Meyers C. J., Shah S. D., Patel S. C., Sneeringer R. M., Bessel C. A., Dollahon N. R., Leising R. A., and Takeuchi E. S. Templated Synthesis of Carbon Materials from Zeolites (Y, Beta, and ZSM-5) and a Montmorillonite Clay (K10): Physical and Electrochemical Characterization. *J. Phys. Chem. B*, 105(11):2143–2152, 2001.

[164] Bhatia S. K. and Myers A. L. Optimum Conditions for Adsorptive Storage. *Langmuir*, 22(4):1688–1700, 2006.

[165] Stadie N. P., Murialdo M., Ahn C. C., and Fultz B. Anomalous Isosteric Enthalpy of Adsorption of Methane on Zeolite-Templated Carbon. *J. Am. Chem. Soc.*, 135(3):990–993, 2013.

[166] Casco M. E., Martínez-Escandell M., Gadea-Ramos E., Kaneko K., Silvestre-Albero J., and Rodríguez-Reinoso F. High-Pressure Methane Storage in Porous Materials: Are Carbon Materials in the Pole Position? *Chem. Mater.*, 27:959–964, 2015.

[167] Rowsey R., Taylor E. E., Irle S., Stadie N. P., and Szilagyi R. K. Methane Adsorption on Heteroatom-Modified Maquettes of Porous Carbon Surfaces. *J. Phys. Chem. A*, 125(28):6042–6058, 2021.

[168] Nicholson D. Simulation studies of methane transport in model graphite micropores. *Carbon*, 36(10):1511–1523, 1998.

[169] Cracknell R. F., Gordon P., and Gubbins K. E. Influence of pore geometry on the design of microporous materials for methane storage. *J. Phys. Chem.*, 97(2):494–499, 1993.

[170] Stadie N. P., Murialdo M., Ahn C. C., and Fultz B. Unusual Entropy of Adsorbed Methane on Zeolite-Templated Carbon. *J. Phys. Chem. C*, 119(47):26409–26421, 2015.

[171] Hou P.-X., Orikasa H., Yamazaki T., Matsuoka K., Tomita A., Setoyama N., Fukushima Y., and Kyotani T. Synthesis of nitrogen-containing microporous carbon with a highly ordered structure and effect of nitrogen doping on H_2O adsorption. *Chem. Mater.*, 17(20):5187–5193, 2005.

[172] Zhou J., Li W., Zhang Z., Xing W., and Zhuo S. Carbon dioxide adsorption performance of N-doped zeolite Y templated carbons. *RSC Adv.*, 2(1):161–167, 2012.

[173] Mostazo-López M. J., Ruiz-Rosas R., Castro-Muñiz A., Nishihara H., Kyotani T., Morallón E., and Cazorla-Amorós D. Ultraporous nitrogen-doped zeolite-templated carbon for high power density aqueous-based supercapacitors. *Carbon*, 129:510–519, 2018.

[174] Han S. W., Bang J., Ko S. H., and Ryoo R. Variation of nitrogen species in zeolite-templated carbon by low-temperature carbonization of pyrrole and the effect on oxygen reduction activity. *J. Mater. Chem. A*, 2019.

[175] Ravel B. and Newville M. ATHENA, ARTEMIS, HEPHAESTUS: data analysis for X-ray absorption spectroscopy using IFEFFIT. *J. Synchrotron Radiat.*, 12(4):537–541, 2005.

[176] Sievarts A. Die aufnahme von gasen durch metalle. *Z. Metallkd.*, 21(37):374, 1929.

[177] Shimoyama I., Wu G., Sekiguchi T., and Baba Y. Evidence for the existence of nitrogen-substituted graphite structure by polarization dependence of near-edge x-ray-absorption fine structure. *Phys. Rev. B*, 62(10):R6053, 2000.

[178] Gago R., Jiménez I., Neidhardt J., Abendroth B., Caretti I., Hultman L., and Möller W. Correlation between bonding structure and microstructure in fullerenelike carbon nitride thin films. *Phys. Rev. B*, 71(12):125414, 2005.

[179] Choi H. C., Park J., and Kim B. Distribution and Structure of N Atoms in Multiwalled Carbon Nanotubes Using Variable-Energy X-Ray Photoelectron Spectroscopy. *J. Phys. Chem. B*, 109(10):4333–4340, 2005.

[180] Hellgren N., Guo J., Luo Y., Såthe C., Agui A., Kashtanov S., Nordgren J., Ågren H., and Sundgren J.-E. Electronic structure of carbon nitride thin films studied by X-ray spectroscopy techniques. *Thin Solid Films*, 471(1):19–34, 2005.

[181] Zhang L.-S., Liang X.-Q., Song W.-G., and Wu Z.-Y. Identification of the nitrogen species on N-doped graphene layers and Pt/NG composite catalyst for direct methanol fuel cell. *Phys. Chem. Chem. Phys.*, 12(38):12055–12059, 2010.

[182] Zhong J., Deng J.-J., Mao B.-H., Xie T., Sun X.-H., Mou Z.-G., Hong C.-H., Yang P., and Wang S.-D. Probing solid state N-doping in graphene by X-ray absorption near-edge structure spectroscopy. *Carbon*, 50(1):335–338, 2012.

[183] Schiros T., Nordlund D., Pálová L., Prezzi D., Zhao L., Kim K. S., Wurstbauer U., Gutiérrez C., Delongchamp D., Jaye C., Fischer D., Ogasawara H., Pettersson L. G. M., Reichman D. R., Kim P., Hybertsen M. S., and Pasupathy A. N. Connecting Dopant Bond Type with Electronic Structure in N-Doped Graphene. *Nano Lett.*, 12(8):4025–4031, 2012.

[184] Gao Y., Hu G., Zhong J., Shi Z., Zhu Y., Su D. S., Wang J., Bao X., and Ma D. Nitrogen-Doped sp^2-Hybridized Carbon as a Superior Catalyst for Selective Oxidation. *Angew. Chem. Int. Edit.*, 52(7):2109–2113, 2013.

[185] Rabchinskii M. K., Saveliev S. D., Stolyarova D. Y., Brzhezinskaya M., Kirilenko D. A., Baidakova M. V., Ryzhkov S. A., Shnitov V. V., Sysoev V. V., and Brunkov P. N. Modulating nitrogen species via N-doping and post annealing of graphene derivatives: XPS and XAS examination. *Carbon*, 182:593–604, 2021.

[186] Sainio S., Wester N., Aarva A., Titus C. J., Nordlund D., Kauppinen E. I., Leppänen E., Palomäki T., Koehne J. E., Pitkänen O., Kordas K., Kim M., Lipsanen H., Mozetič M., Caro M. A., Meyyappan M., Koskinen J., and Laurila T. Trends in Carbon, Oxygen, and Nitrogen Core in the X-ray Absorption Spectroscopy of Carbon Nanomaterials: A Guide for the Perplexed. *J. Phys. Chem. C*, 125(1):973–988, 2021.

[187] Stadie N. P. Synthesis and Thermodynamic Studies of Physisorptive Energy Storage Materials, 2013.

[188] Brown I. D. and McMahon B. CIF: the computer language of crystallography. *Acta Crystallogr. B*, 58(3):317–324, 2002.

[189] Aroyo M. I., Perez-Mato J. M., Orobengoa D., Tasci E., de la Flor G., and Kirov A. Crystallography online: Bilbao crystallographic server. *Bulg. Chem. Commun*, 43(2):183–197, 2011.

APPENDICES

APPENDIX A

THEORETICAL MATERIAL CHARACTERISTICS OF CARBON SCHWARZITES

Table A.1: Theoretical material characteristics of the nine smallest schwarzite models.

Carbon Model	Contribution of Carbon Rings				Density	Surface Area [a,b]	Pore Volume [a,b]	Largest Free Sphere [a,c]	Energetics[d 20]
	5	6	7	8	(g mL^{-1})	(m^2 g^{-1})	(mL g^{-1})	(Å)	(kJ mol^{-1})
P688	-	40%	-	60%	2.00	0	0	0.60	51.1
G688	-	40%	-	60%	2.15	0	0	0.92	22.8
D688	-	40%	-	60%	3.09	0	0	1.02	4.3
P7par	-	81%	19%	-	1.20	1170	0.44	7.14	45.5
IWPg	7%	80%	-	13%	1.03	900	0.36	4.85	55.0
D766	-	70%	30%	-	1.07	800	0.26	5.23	26.8
P8bal	-	87%	-	13%	1.13	1100	0.41	3.85	21.5
G8bal	-	87%	-	13%	1.19	1190	0.38	4.72	24.1
D8bal	-	87%	-	13%	1.29	1240	0.42	5.06	27.3
C_{60}	38%	62%	-	-	1.65	5090	-	74.65	64.2
Graphite	-	100%	-	-	2.26	0	0	0.44	0

[a] Calculations performed using Zeo++ (see Appendix E)

[b] N_2 accessible

[c] probe diameter

[d] relative to graphite

APPENDIX B

SYNTHESIS OF ARCHETYPICAL ZEOLITE-TEMPLATED CARBON

B.1 Drying Zeolite

In order to impregnate a zeolite template, the zeolite must first be vacuum dried and transferred to a glove box. Fill a tall test tube (55 mL) approximately half-way with zeolite template and cap with a vented piece of aluminum foil. Leave the zeolite powder loose inside the test tube and do not tap the zeolite down or the zeolite may bump out of the test tube when a vacuum is pulled. Place the assembled test tube into the Büchi oven (B-585 glass oven), as shown in Figure B.1. Once the Büchi oven is sealed, pull a vacuum and heat to 300 °C for 24 hours before bringing the cooled zeolite into the glovebox where it can be stored indefinitely in inert gas.

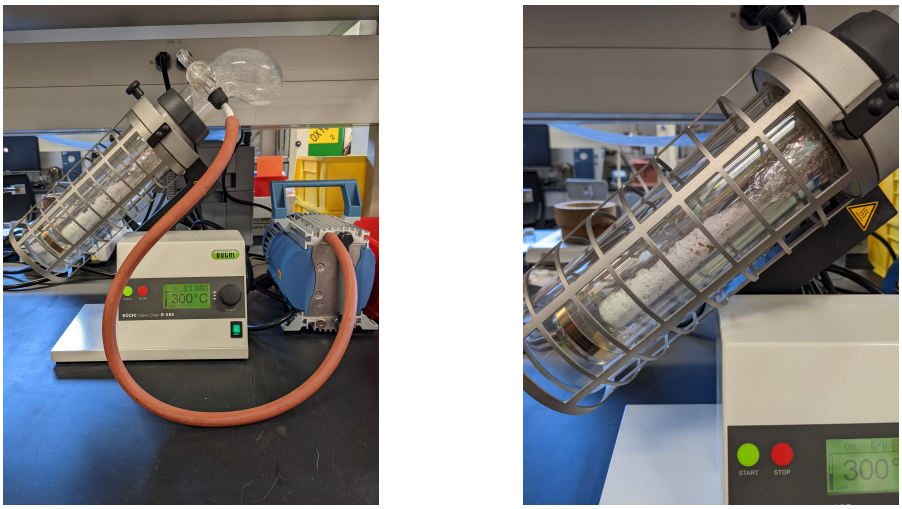

(a) (b)

Figure B.1: Drying NaY in a Büchi oven (a) showing Büchi oven set-up to oil-free vacuum pump and (b) a close up of the vented foil capped test tube filled approximately half-way with zeolite template. Notice the loose nature of the zeolite.

B.2 Zeolite Impregnation with Furfuryl Alcohol

For a single boat horizontal tube CVD synthesis, begin by transferring 2 g of dried zeolite from the glovebox into a 2-neck round-bottom flask and assemble as shown in Figure B.2a and Figure B.2b with a stir bar, rubber septum, and Teflon stopcock.

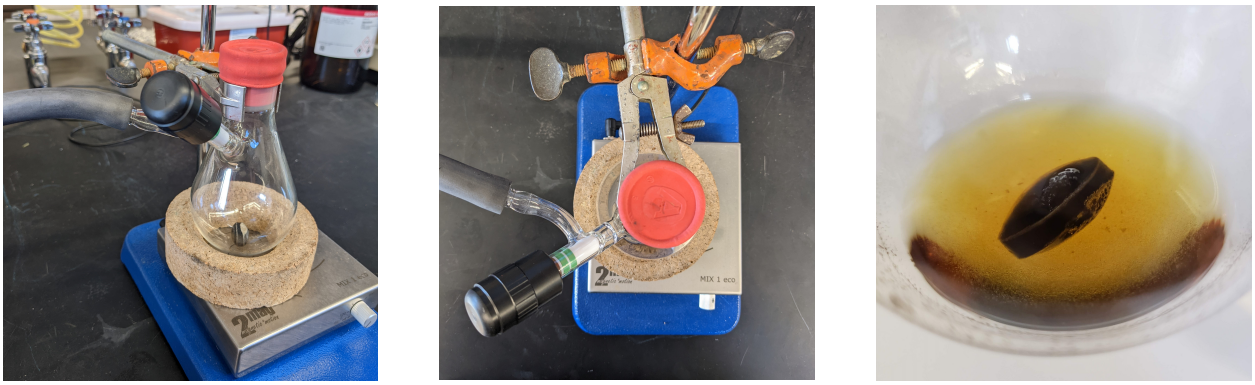

(a) (b) (c)

Figure B.2: FA-Zeolite Impregnation Set-Up: (a) side-view of 2-neck round-bottom flask set up for FA impregnation, (b) top-down view of 2-neck round-bottom flask set up for FA impregnation, and (c) zeolite soaking in FA in 2-neck round-bottom flask with stir bar.

Upon bringing the 2-neck round-bottom flask out of the glovebox, attach the flask to a vacuum system, open the stopcock and pull a vacuum, ensuring that the rubber septum compresses. Measure 20 mL of furfuryl alcohol (FA) into a syringe equipped with an 18G disposable needle. Close the stopcock and add the FA to the 2-neck round-bottom flask by inserting the needle into the rubber septum. The decreased pressure will pull the FA from the syringe into the flask. The color of the FA may change from a light yellow to a dark forest green or amber color (as seen in Figure B.2c). Note any color changes, however, no correlation between FA color and synthesis conditions have been identified so far. Once all of the FA has been added to the flask, begin stirring the zeolite-FA mixture at a speed that effectively mixes the FA without splashing onto the walls of the flask. If any dried zeolite is stuck to the side of the walls, gently tilt the round-bottom flask to incorporate the zeolite into the FA. Allow the mixture to stir under passive vacuum for at least 12 hours. To achieve a passive vacuum, do not open the stopcock, but leave the vacuum turned on to prevent any air leaks into the flask. Be sure to setup the impregnation out of direct sunlight, as this can cause premature polymerization of FA.

After the mixture has stirred for at least 12 h, assemble a vacuum filtration set up as shown in Figure B.3a, with a 125 mL glass-fritted Büchner funnel (Por. 4, Robu) attached

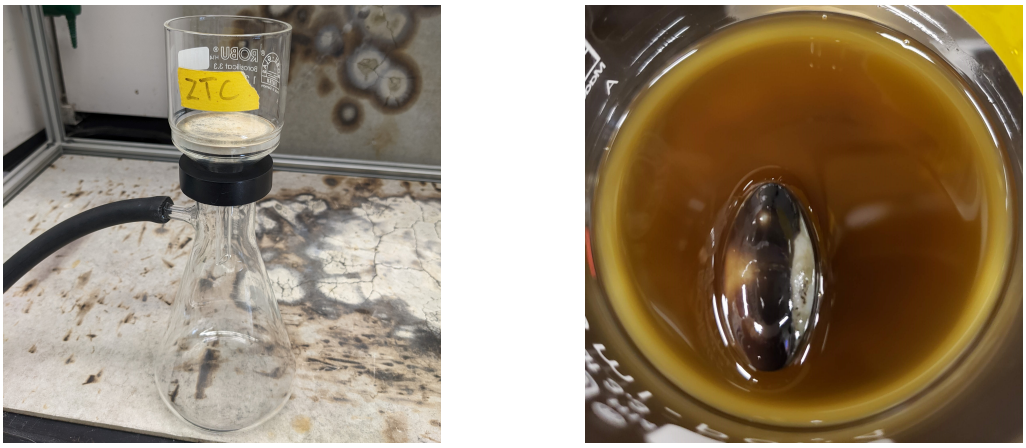

(a) (b)

Figure B.3: FA-Zeolite Composite Filtration; (a) Vacuum-filtration set-up with designated "ZTC" Büchner funnel and (b) FA with FA-zeolite composite and stir bar poured onto the Büchner funnel filter frit.

to a 500 mL filtration flask. Remove the vacuum line on the 2-neck round-bottom flask and open the stopcock to remove the rubber septum. Swirl the mixture and empty the contents of the round bottom flask into the Büchner funnel. While pulling a vacuum on the filtration setup, rinse the flask out with mesitylene (98%, Aldrich) and add to the Büchner funnel. Gently, remove the stir bar with a spatula and rinse the spatula over the Büchner funnel with mesitylene. Allow the surface of the zeolite to dry before proceeding. Mesitylene will be used to remove any excess FA from the external surface of the zeolite particles. Add enough mesitylene to cover the surface of the zeolite and allow the liquid to filter through. Once the filtrate becomes colorless, proceed with one more mesitylene wash. Usually three washes of mesitylene are needed to rinse the zeolite. At this point, the zeolite will still be a dark reddish brown color, as shown in Figure B.4a. Allow the zeolite to dry under vacuum on the filter frit for at least 10 min. If the zeolite is scraped while wet, the zeolite will conglomerate as seen in Figure B.4b. The dark coloration indicates that mesitylene is left on the surface of the zeolite. Any leftover mesitylene will carbonize and form graphitic build-up on the external surface of the zeolite during CVD. Once the zeolite has conglomerated like the material shown in Figure B.4b, the material will not be recoverable. A fully dried zeolite (Figure B.4c) will be

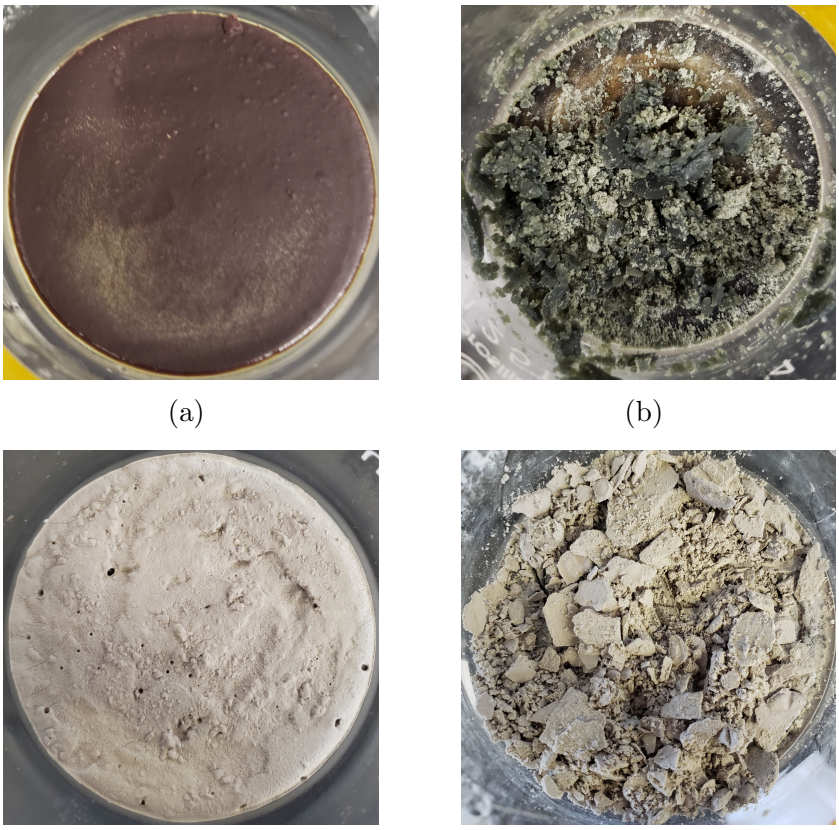

(a) (b)

(c) (d)

Figure B.4: FA-Zeolite Composite Drying Steps: a) filtered FA-zeolite composite that is still wet, b) FA-zeolite composite stirred while still wet, c) filtered FA-zeolite composite after drying under vacuum on filter frit for 10 min, and d) FA-zeolite composite stirred when dry and ready to be transferred to alumina boat.

much lighter in color. At this point it is safe to break up the zeolite with a spatula while still pulling a vacuum (Figure B.4d). Obtain an alumina boat (10×30×107 mm) and prepare for a quick transfer. Once the Büchner funnel is removed from the flask, some vapors will be able to saturate the zeolite through the filter frit. Therefore it is important to work quickly while avoiding any material that resembles Figure B.4b. Remove the Büchner funnel from the filtration flask and quickly transfer the dried FA-zeolite composite to 2/3 of the alumina boat, as shown in Figure B.5a. Regardless of the liquid FA color, the FA impregnated zeolite is always green in color.

(a) FA-zeolite composite in alumina boat.

(b) ZTC-zeolite composite in alumina boat.

Figure B.5: Material in alumina boat (a) before, and (b) after pyrolysis and CVD.

B.3 Chemical Vapor Deposition

Once the zeolite has been impregnated and any excess FA has been removed from the surface of the zeolite particles, the FA can be polymerized and pyrolyzed inside the zeolite pores and more carbon can be introduced via propylene chemical vapor deposition (CVD). CVD is accomplished using a homemade CVD manifold (Figure B.6c), where gas is flowed from gas cylinders (Figure B.6a) to LabView controlled Bronkhorst flowmeters (Figure B.6b) through the manifold and into a quartz tube (ϕ 45 mm), which is installed into a horizontal tube furnace (HST 12/600, Carbolite Gero) furnace. Insert the alumina boat into the quartz tube and push the alumina boat to the center of the furnace using a thin meter stick. Assemble the quartz tube into the metal fitting as shown in Figure B.6e. Be sure to create a complete seal by observing complete contact around the o-ring as shown in Figure B.6f.

The CVD temperature profile for FA-ZTCs (see Figure B.7) involves a 24 h hold at 80 °C (step B to C) to polymerize the FA inside the zeolite pores, followed by a ramp (step C to D) and hold at the desired deposition temperature (step D to G), with a set period of time dedicated to flowing carbon deposition gas (step E to F), ending in a ramp (step G to H) and hold at a higher temperature for a heat treatment step (step H to I). The ramp rate used for

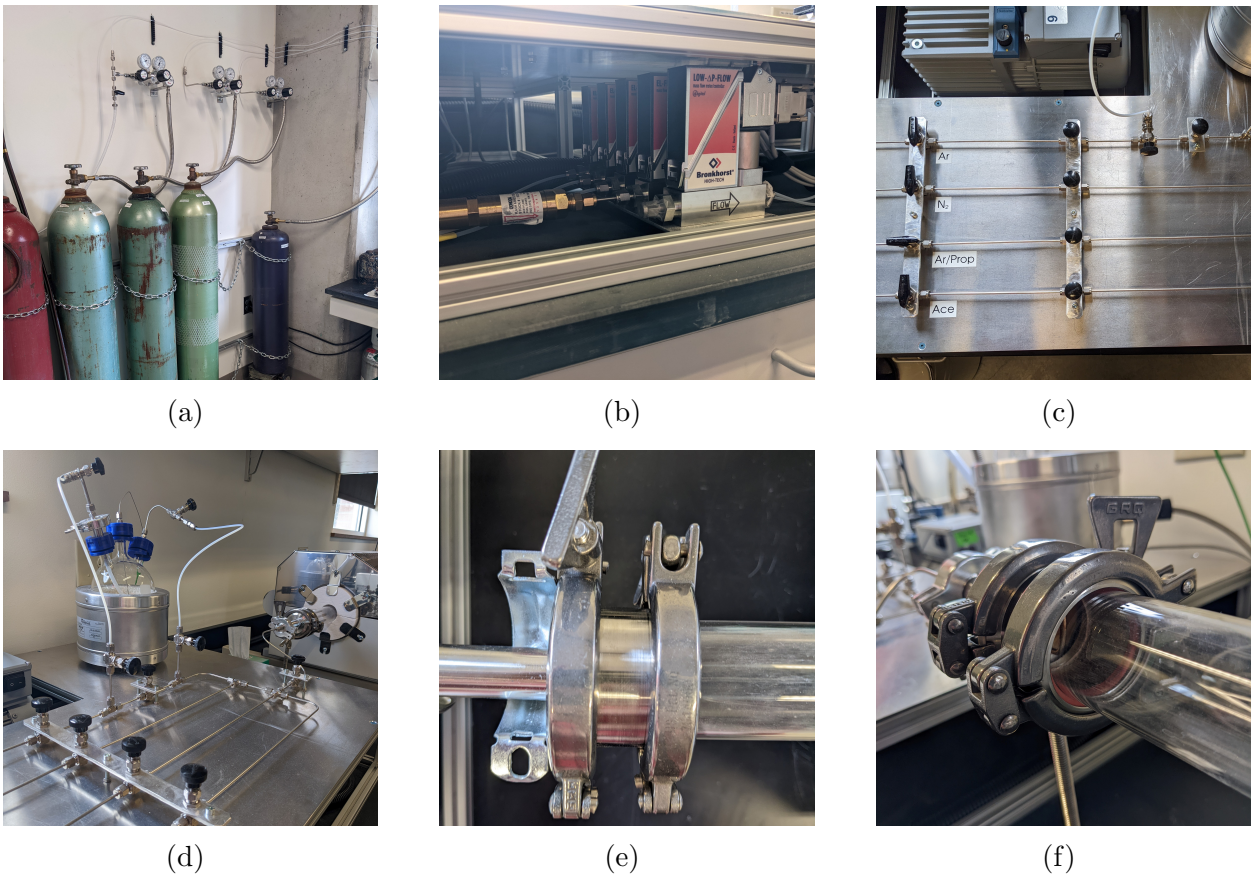

(a) (b) (c)

(d) (e) (f)

Figure B.6: Chemical Vapor Deposition Set-Up: (a) gas cylinder set up, (b) Bronkhorst flow meters installed below CVD manifold, (c) CVD manifold, (d) CVD manifold with optional liquid bubbler attachment, (e) metal to quartz tube joint, and (f) metal to quartz tube seal.

all ramping steps was set to 5 °C per min, which is the maximum ramp rate recommended by Carbolite. Using the furnace controller, program in the desired temperature profile. Based on the start time, calculate the times required to change gas flow. After the furnace has cooled overnight, under inert flow, collect a small amount of zeolite-ZTC composite for TGA analysis and transfer the remaining material to a centrifuge tube (50 mL, polypropylene, self-standing with polypropylene cap). If more than one alumina boat was used for CVD, empty each alumina boat into separate centrifuge tubes.

The resulting zeolite-ZTC powder is black in color and usually light and fluffy. If the

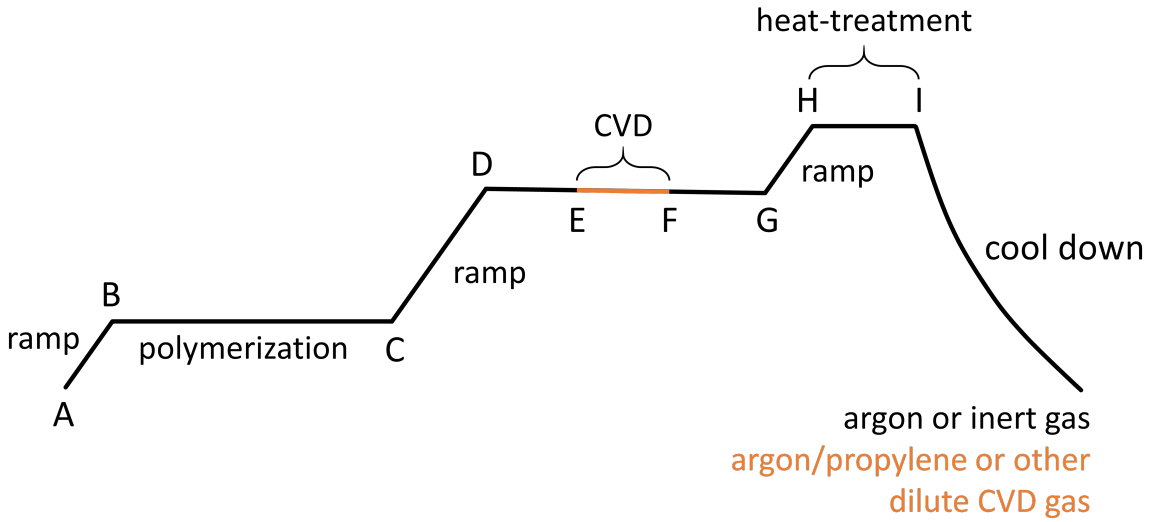

Figure B.7: General ZTC synthesis temperature profile.

material appears to be chunky and hard to break up with a spatula the ZTC is usually over deposited.

B.4 Zeolite Dissolution with Hydrofluoric Acid

After CVD and heat treatment, the ZTC will be formed inside the zeolite template. Hydrofluoric acid (HF) can be used to dissolve the zeolite, leaving a freestanding ZTC framework. To the centrifuge tube with zeolite-ZTC composite, add approximately 5 mL of deionized (DI) water to help mitigate any splattering that can occur when adding HF. For the first HF wash, slowly add a couple drops of HF (48-51%, Thermo Scientific) observing any reaction taking place. If the HF is splattering, wait until the reaction stops before adding more HF. However, if the mixture is not noticeably reacting, fill the centrifuge tube to 37 mL with HF and allow to sit for 24 h. Be sure to cap the HF bottle and do not leave any HF loosely covered as HF can vaporize and etch any glassware or table top in the hood.

Without disturbing the settled solid, carefully pour out as much HF as possible without pouring out any black ZTC powder. Fill the centrifuge tube back to 37 mL with HF and repeat the HF wash a total of three times. The second and third HF washes should not react

as violently as the initial wash when HF is added. After the third HF wash, the ZTC will need to be rinsed with DI water to ensure any remaining HF is removed. After pouring out as much HF as possible, centrifuge the tube at 7830 rpm for 5 min. The ZTC should now form a more compact pile at the bottom of the centrifuge tube making it easier to remove the last bit of HF. Fill the centrifuge tube to 37 mL with DI water, shake to disperse the ZTC and centrifuge at 7830 rpm for 10 min. Decant all of the water from the ZTC. Some ZTC may be lost during the water wash steps. Repeat the water wash a total of three times. After decanting the third water wash, centrifuge the tube once more at 7830 rpm for 5 min and pour off any remaining water. Cover the centrifuge tube with a vented piece of aluminum foil and place in a 40 °C drying oven for at least one week. Set aside a designated drying oven without any important glass ware and do not dry more than four to five samples at a time in a single drying oven as any leftover HF fumes can etch glass and the inside of the drying oven. Check the dryness of the ZTC by rotating the centrifuge tube after one week. Do not store the ZTC wet. After using XRD to determine if all of the zeolite has successfully been removed, weigh and transfer the ZTC to a glass vial.

B.5 Storing Zeolite-Templated Carbons

ZTCs may break down over time if stored in ambient conditions. Storing ZTCs in inert conditions can extend the shelf-life of these materials. However, before storing the materials in a glovebox they must first be degassed. Make sure the glass vial is no more than one third full with material. If the vial is filled more, split the sample into two vials during the drying process. Cover the glass vial(s) with a vented piece of aluminum foil and place into the glass Büchi oven suspended by a wire. Slowly pull a vacuum on the oven, ensuring the the powder does not bump out of the vial. Heat the furnace to 120 °C and hold for at least 12 h. After the oven has cooled, the glass vial(s) can be transferred into a glovebox and stored indefinitely under inert gas.

APPENDIX C

EXPERIMENTAL ZEOLITE-TEMPLATED CARBON CHARACTERIZATION METHODS

C.1 X-Ray Diffraction

Powder XRD patterns were measured using Cu Kα radiation (λ=1.54 Å), generated at 40 kV and 40 mA, in Bragg-Brentano geometry (D8 Advance, Bruker Corp.). The powder was thinly dispersed on a "low-background" sample holder comprised of oriented crystalline silicon.

C.2 Thermogravimentric Analysis

Thermogravimetric analysis (TGA) was performed using a microbalance (Discovery TGA 5500, TA Instruments) under flowing dry air at 25 mL min^{-1} (Grade D breathing air with a moisture trap) to determine the hydrocarbon content of each zeolite-carbon composite prior to HF treatment. The temperature program was specified as follows: the sample was first held at 50 °C for 15 min under dry air to purge, and then water removal was performed by heating up to 300 °C at 10 °C per min and holding for 1 h. The weight at the end of this dehydration step was taken to be the initial mass, m_i. The carbon was oxidized by heating up to 800 °C at 5 °C per min and holding for 2 h, and finally remaining sample was cooled to 300 °C and held for 1 h to determine the final weight (m_f).

C.2.1 SPD Example Calculations

The structural packing density (SPD) can be calculated using the data obtained from thermogravimetric analysis (see Figure 2.7), where in this case m_i and m_f are measured to be 16.219 mg and 11.978 mg, respectively.

$$\mathrm{SPD_{exp}} = \frac{m_{ZTC}}{m_{zeolite}} = \frac{m_i - m_f}{m_f} = g_{ZTC}\, g_{zeolite}^{-1} \tag{C.1}$$

$$\mathrm{SPD_{cell}} = \frac{m_{ZTC}}{m_{SiO_2}} = \mathrm{SPD_{exp}} \times \frac{MW_{zeolite}}{MW_{SiO_2}} = g_{ZTC}\, g_{SiO_2}^{-1} \tag{C.2}$$

Thus, from Equation C.1,

$$\mathrm{SPD_{exp}} = \frac{\mathrm{m_i - m_f}}{\mathrm{m_f}} = \frac{16.219\ \mathrm{mg} - 11.978\ \mathrm{mg}}{11.978\ \mathrm{mg}} = 0.354\ \mathrm{g_{ZTC}\ g_{zeolite}^{-1}} \tag{C.3}$$

To convert from $\mathrm{SPD_{exp}}$ to $\mathrm{SPD_{cell}}$ the molecular weight of the zeolite can be used. For this example, the zeolite used is Tosoh NaY ($5.5\mathrm{SiO_2 \cdot Al_2O_3 \cdot Na_2O}$), thus the molecular weight of the zeolite is defined as:

$$\mathrm{MW_{zeolite}} = 5.5(60.08\ \mathrm{g\ mol^{-1}}) + 101.96\ \mathrm{g\ mol^{-1}} + 61.98\ \mathrm{g\ mol^{-1}} = 494.38\ \mathrm{g\ mol^{-1}} \tag{C.4}$$

The corresponding pure $\mathrm{SiO_2}$ version of this zeolite would take the form of $7.5\mathrm{SiO_2}$ (5.5+2). Therefore, the molecular weight of the corresponding pure $\mathrm{SiO_2}$ zeolite would be:

$$\mathrm{MW_{SiO_2}} = 7.5(60.08\ \mathrm{g\ mol^{-1}}) = 450.60\ \mathrm{g\ mol^{-1}} \tag{C.5}$$

Now, using Equation C.2, $\mathrm{SPD_{exp}}$ can be converted to $\mathrm{SPD_{cell}}$, which is a comparable metric across all ZTCs synthesized inside the same type of zeolite framework (example **FAU**).

$$\mathrm{SPD_{cell}} = 0.354\ \mathrm{g_{ZTC}\ g_{zeolite}^{-1}} \times \frac{494.38\ \mathrm{g_{zeolite}\ mol^{-1}}}{450.60\ \mathrm{g_{SiO_2}\ mol^{-1}}} = 0.388\ \mathrm{g_{ZTC}\ g_{SiO_2}^{-1}} \tag{C.6}$$

C.3 Nitrogen Adsorption

Nitrogen adsorption/desorption isotherms were measured at 77 K using an automated volumetric instrument (3Flex, Micromeritics Instrument Corp.). Specific surface areas were calculated by the Brunauer-Emmett-Teller (BET) method. Pore-size distributions were determined by nonlocal density functional theory (NLDFT) calculations using a dedicated software package (MicroActive Share, Micromeritics Instrument Corp.) with the "version 2 deconvolution" setting using a carbon slit-pore model.

APPENDIX D

CONVERTING CIF TO P1 SETTING

Many theoretical structure calculations requires a fractional coordinate input file with no built-in symmetry operations. However, most periodic atomistic models are provided as crystallographic information files (CIF),[188] which are constructed using space groups with built-in symmetry operations. In order to remove implied symmetry operations, each CIF must first be converted to a P1 setting. This conversion can be performed using the Bilbao Crystallographic Server Structure Data Converter & Editor.[189]

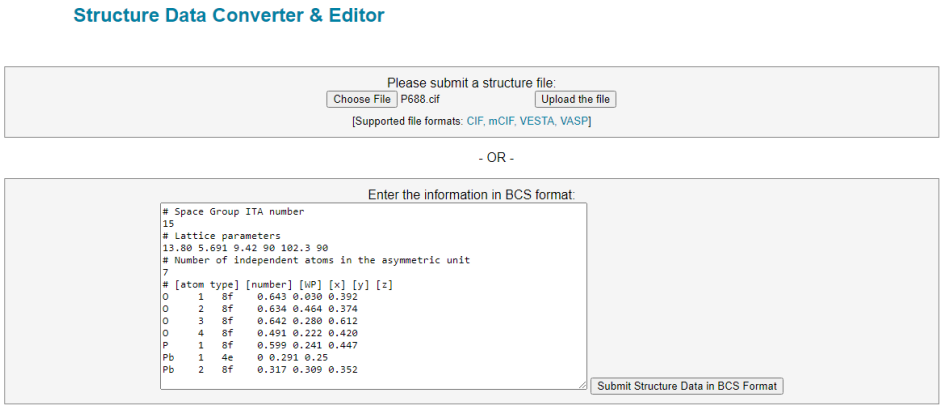

Figure D.1: Uploading CIF to Bilbao Crystallographic Server Structure Data Converter & Editor

First, choose the CIF to be converted and upload the file, as shown in Figure D.1. Ensure that the space group was correctly identified from the CIF, as seen outlined in green in Figure D.2. If the space group is not correct, or if one was not assigned, navigate to the Table of Space Group Symbols to identify the correct space group number.

The CIF can then be converted by clicking on "Transform the structure to P1 setting" outlined in orange in Figure D.2. Larger unit cells can take a long time, but the web-page will refresh when the conversion is complete.

When the web-page refreshes, scroll down to the converter and editor options and select "Export to Standard CIF format", as outlined in purple in Figure D.2. In the new web-page scroll down to the bottom of the page to find a a copy-allowed P1 version of the original CIF can be saved and used for various calculations.

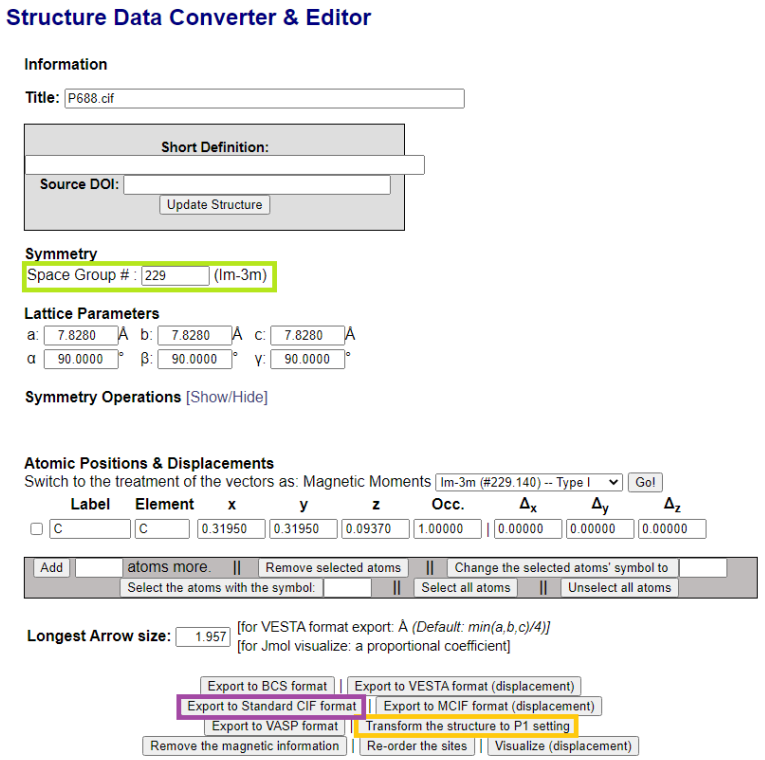

Figure D.2: Bilbao Crystallographic Server Structure Data Converter & Editor General View

APPENDIX E

THEORETICAL SURFACE AREA, PORE-SIZE DISTRIBUTION, AND PORE VOLUME CALCULATIONS USING ZEO++

Zeo++[124] is a software package designed to analyze periodic porous materials. Zeo++ version 0.3 (released 6/20/2017) was used for all calculations in this work.

E.1 Input File Set-Up

Zeo++ uses a modified CSSR file format as structural input files. Starting with a P1 formatted CIF (see Appendix D), copy and paste the fractional coordinates section to an Excel sheet. Remove columns A and F, leaving only atom type, x-, y-, and z-fractional coordinates. To the left of the atom type, add a column that enumerates the rows, and to the right of the z-fractional coordinates, add nine columns filled with zeros. A finished example can be seen in Figure E.1.

	A	B	C	D	E	F	G	H	I	J	K	L	M	N
1	1	C	0.3195	0.3195	0.0937	0	0	0	0	0	0	0	0	0
2	2	C	0.8195	0.8195	0.5937	0	0	0	0	0	0	0	0	0
3	3	C	0.3195	0.6805	0.9063	0	0	0	0	0	0	0	0	0
4	4	C	0.8195	0.1805	0.4063	0	0	0	0	0	0	0	0	0
5	5	C	0.6805	0.3195	0.9063	0	0	0	0	0	0	0	0	0
6	6	C	0.1805	0.8195	0.4063	0	0	0	0	0	0	0	0	0
7	7	C	0.6805	0.6805	0.0937	0	0	0	0	0	0	0	0	0
8	8	C	0.1805	0.1805	0.5937	0	0	0	0	0	0	0	0	0
9	9	C	0.3195	0.0937	0.3195	0	0	0	0	0	0	0	0	0
10	10	C	0.0937	0.3195	0.3195	0	0	0	0	0	0	0	0	0
11	11	C	0.8195	0.5937	0.8195	0	0	0	0	0	0	0	0	0
12	12	C	0.3195	0.9063	0.6805	0	0	0	0	0	0	0	0	0
13	13	C	0.9063	0.3195	0.6805	0	0	0	0	0	0	0	0	0
14	14	C	0.8195	0.4063	0.1805	0	0	0	0	0	0	0	0	0
15	15	C	0.6805	0.0937	0.6805	0	0	0	0	0	0	0	0	0
16	16	C	0.9063	0.6805	0.3195	0	0	0	0	0	0	0	0	0
17	17	C	0.1805	0.5937	0.1805	0	0	0	0	0	0	0	0	0
18	18	C	0.6805	0.9063	0.3195	0	0	0	0	0	0	0	0	0
19	19	C	0.0937	0.6805	0.6805	0	0	0	0	0	0	0	0	0

Figure E.1: Example Excel Sheet used to format a Zeo++ compatible CSSR file

At this point, the coordinate section of the CSSR file is complete. Open a text editor, and name the file according to the structure, followed by an extension of .cssr. The first four rows of the file include structural information and notes. In the first row, input the unit cell dimensions (a, b, and c) separated by spaces. The second row is used for defining the unit cell angles (α, β, and γ) separated by spaces, followed by "SPGR= 1 P 1 OPT=1" which defines symmetry information but is currently not used by Zeo++. In the third row, insert the number of atoms per unit cell followed by a space and a zero. The fourth row is used record the name of the structure, starting with a zero followed by a space, and name:name. The fifth row starts the fractional coordinates section, which can be copied and

```
7.8280 7.8280 7.8280
90   90   90   SPGR =  1 P 1         OPT = 1
48 0
0 P688: P688
1       C       0.3195  0.3195  0.0937  0       0       0       0       0       0       0       0       0
2       C       0.8195  0.8195  0.5937  0       0       0       0       0       0       0       0       0
3       C       0.3195  0.6805  0.9063  0       0       0       0       0       0       0       0       0
4       C       0.8195  0.1805  0.4063  0       0       0       0       0       0       0       0       0
5       C       0.6805  0.3195  0.9063  0       0       0       0       0       0       0       0       0
6       C       0.1805  0.8195  0.4063  0       0       0       0       0       0       0       0       0
7       C       0.6805  0.6805  0.0937  0       0       0       0       0       0       0       0       0
8       C       0.1805  0.1805  0.5937  0       0       0       0       0       0       0       0       0
9       C       0.3195  0.0937  0.3195  0       0       0       0       0       0       0       0       0
10      C       0.0937  0.3195  0.3195  0       0       0       0       0       0       0       0       0
11      C       0.8195  0.5937  0.8195  0       0       0       0       0       0       0       0       0
12      C       0.3195  0.9063  0.6805  0       0       0       0       0       0       0       0       0
13      C       0.9063  0.3195  0.6805  0       0       0       0       0       0       0       0       0
14      C       0.8195  0.4063  0.1805  0       0       0       0       0       0       0       0       0
15      C       0.6805  0.0937  0.6805  0       0       0       0       0       0       0       0       0
16      C       0.9063  0.6805  0.3195  0       0       0       0       0       0       0       0       0
17      C       0.1805  0.5937  0.1805  0       0       0       0       0       0       0       0       0
18      C       0.6805  0.9063  0.3195  0       0       0       0       0       0       0       0       0
19      C       0.0937  0.6805  0.6805  0       0       0       0       0       0       0       0       0
20      C       0.1805  0.4063  0.8195  0       0       0       0       0       0       0       0       0
21      C       0.5937  0.8195  0.8195  0       0       0       0       0       0       0       0       0
22      C       0.5937  0.1805  0.1805  0       0       0       0       0       0       0       0       0
23      C       0.4063  0.8195  0.1805  0       0       0       0       0       0       0       0       0
24      C       0.4063  0.1805  0.8195  0       0       0       0       0       0       0       0       0
25      C       0.6805  0.6805  0.9063  0       0       0       0       0       0       0       0       0
26      C       0.1805  0.1805  0.4063  0       0       0       0       0       0       0       0       0
27      C       0.6805  0.3195  0.0937  0       0       0       0       0       0       0       0       0
28      C       0.1805  0.8195  0.5937  0       0       0       0       0       0       0       0       0
29      C       0.3195  0.6805  0.0937  0       0       0       0       0       0       0       0       0
30      C       0.8195  0.1805  0.5937  0       0       0       0       0       0       0       0       0
31      C       0.3195  0.3195  0.9063  0       0       0       0       0       0       0       0       0
32      C       0.8195  0.8195  0.4063  0       0       0       0       0       0       0       0       0
33      C       0.6805  0.9063  0.6805  0       0       0       0       0       0       0       0       0
34      C       0.1805  0.4063  0.1805  0       0       0       0       0       0       0       0       0
35      C       0.6805  0.0937  0.3195  0       0       0       0       0       0       0       0       0
36      C       0.1805  0.5937  0.8195  0       0       0       0       0       0       0       0       0
37      C       0.3195  0.9063  0.3195  0       0       0       0       0       0       0       0       0
38      C       0.8195  0.4063  0.8195  0       0       0       0       0       0       0       0       0
39      C       0.3195  0.0937  0.6805  0       0       0       0       0       0       0       0       0
40      C       0.8195  0.5937  0.1805  0       0       0       0       0       0       0       0       0
41      C       0.9063  0.6805  0.6805  0       0       0       0       0       0       0       0       0
42      C       0.4063  0.1805  0.1805  0       0       0       0       0       0       0       0       0
43      C       0.9063  0.3195  0.3195  0       0       0       0       0       0       0       0       0
44      C       0.4063  0.8195  0.8195  0       0       0       0       0       0       0       0       0
45      C       0.0937  0.6805  0.3195  0       0       0       0       0       0       0       0       0
46      C       0.5937  0.1805  0.8195  0       0       0       0       0       0       0       0       0
47      C       0.0937  0.3195  0.6805  0       0       0       0       0       0       0       0       0
48      C       0.5937  0.8195  0.1805  0       0       0       0       0       0       0       0       0
```

Figure E.2: Example Zeo++ CSSR Input File

pasted directly from the Excel sheet made above. An example CSSR file is shown in Figure E.2. Save the CSSR file in the zeo++ folder where the Zeo++ code is located.

In order to ensure the input file is set up correctly, Zeo++ can generate an .xyz file which can be viewed using any structure viewing program. Navigate to the zeo++ folder using a terminal like Cygwin if using a Windows operating system (`https://www.cygwin.com/`). To generate an xyz file, use the code below:

```
./network -xyz input.cssr
```

Where "-xyz" signals the xyz conversion and "input.cssr" is the formatted cssr file generated above.

```
./network -xyz P688.cssr
```

View the generated xyz file to ensure the geometry is correct.

E.2 Surface Area Calculation

To perform a surface area calculation, navigate to the zeo++ folder and follow the code below:

```
./network -ha -sa chan_radius probe_radius num_samples outputfile.sa
    input.cssr
```

Where, "-ha" is recommended for high accuracy calculations to reduce the maximum expected error to less than 0.1 Å, "-sa" signals a surface area measurement, the "chan_radius" is defined as the radius of the probe used to determine the proportion of accessible space, "probe_radius" as the radius of the probed used in Monte Carlo sampling, and "num_samples" is the number of Monte Carlo points per atom.

It is recommended by Zeo++ to set chan_radius and probe_radius to the same value. Therefore, to calculate the N_2 accessible surface area use a chan_radius and probe_radius of 1.86 Å.[125] An example script for calculating the N_2 accessible surface area is proved below.

```
./network -ha -sa 1.86 1.86 5000 P688_186.sa P688.cssr
```

E.3 Pore Volume Calculation

Zeo++ includes multiple ways to calculate the pore volume of a given model; however, Ongari et al. suggest using the -volpo calculation these calculations best match experimental pore volume results.[125] A general template for performing a -volpo calculation is provided below.

```
./network -ha -volpo chan_radius probe_radius num_samples output.sa
    input.cssr
```

Where, "-volpo" signals a probe accessible pore volume measurement, the "chan_radius" is defined as the radius of the probe used to determine the proportion of accessible space, "probe_radius" as the radius of the probed used in Monte Carlo sampling, and "num_samples" is the number of Monte Carlo points per unit cell. To keep calculations between different models consistent the value of " num_samples" will change depending on the unit cell size.

An example script for calculating the N_2 accessible pore volume with 200 probes per atom for P688 (48 atoms in a unit cell) is proved below.

```
./network -ha -volpo 1.86 1.86 9600 P688_186.volpo P688.cssr
```

E.4 Pore-Size Distribution Calculation

Pore-size distributions (PSD) can also be calculated using Zeo++ on periodic models using the following template:

```
./network -ha -psd chan_radius probe_radius num_samples output.
    psd_histo input.cssr
```

Where "num_samples" is the number of Monte Carlo points per atom. The output file contains histogram data which can be plotted using a graphing program. An example script for calculating the N_2 PSD is provided below.

```
./network -ha -psd 1.86 1.86 50000 P688_186.psd_histo P688.cssr
```

APPENDIX F

FOLDING MOLECULAR MODELS

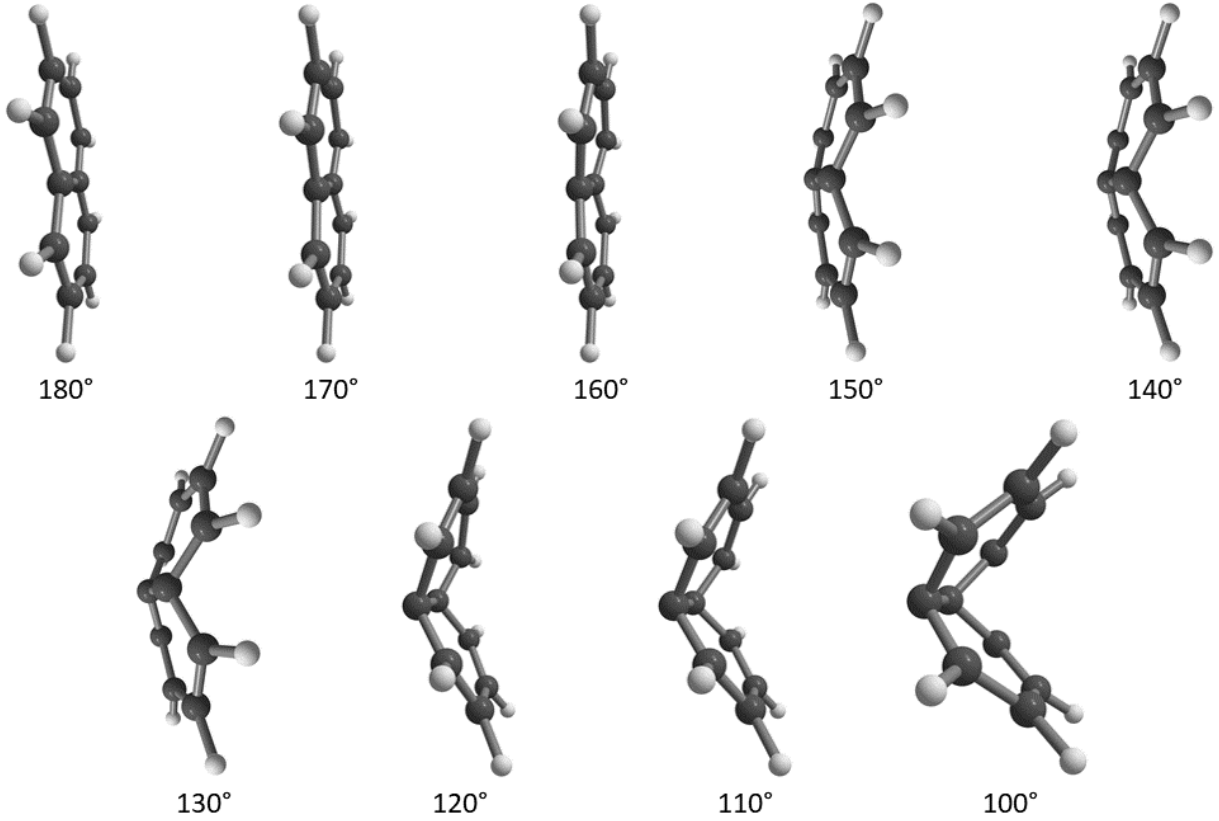

Figure F.1: Folding geometries of naphthalene used in Chapter 5.3.2, while fixing the dihedral angles to the angles indicated below each structure.

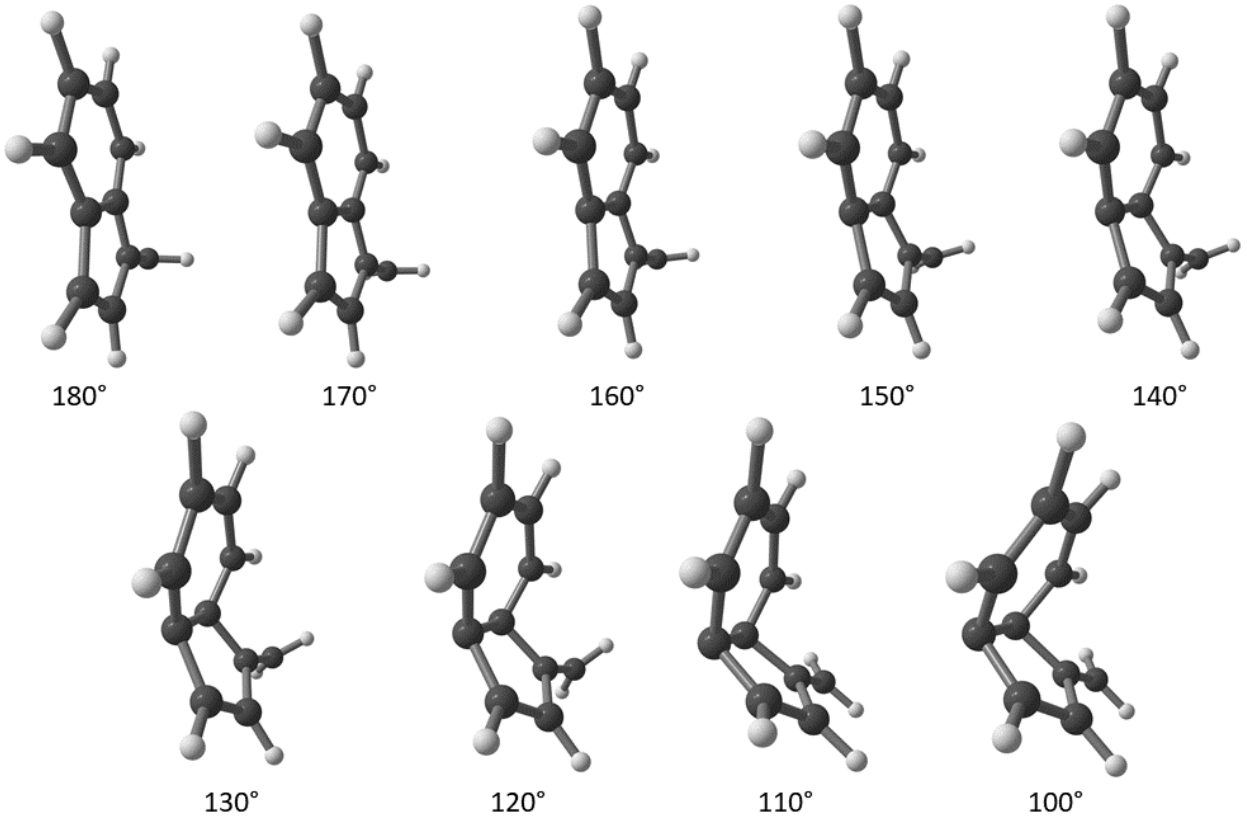

Figure F.2: Folding geometries of 1-methyleneindene used in Chapter 5.3.2, while fixing the dihedral angles to the angles indicated below each structure.

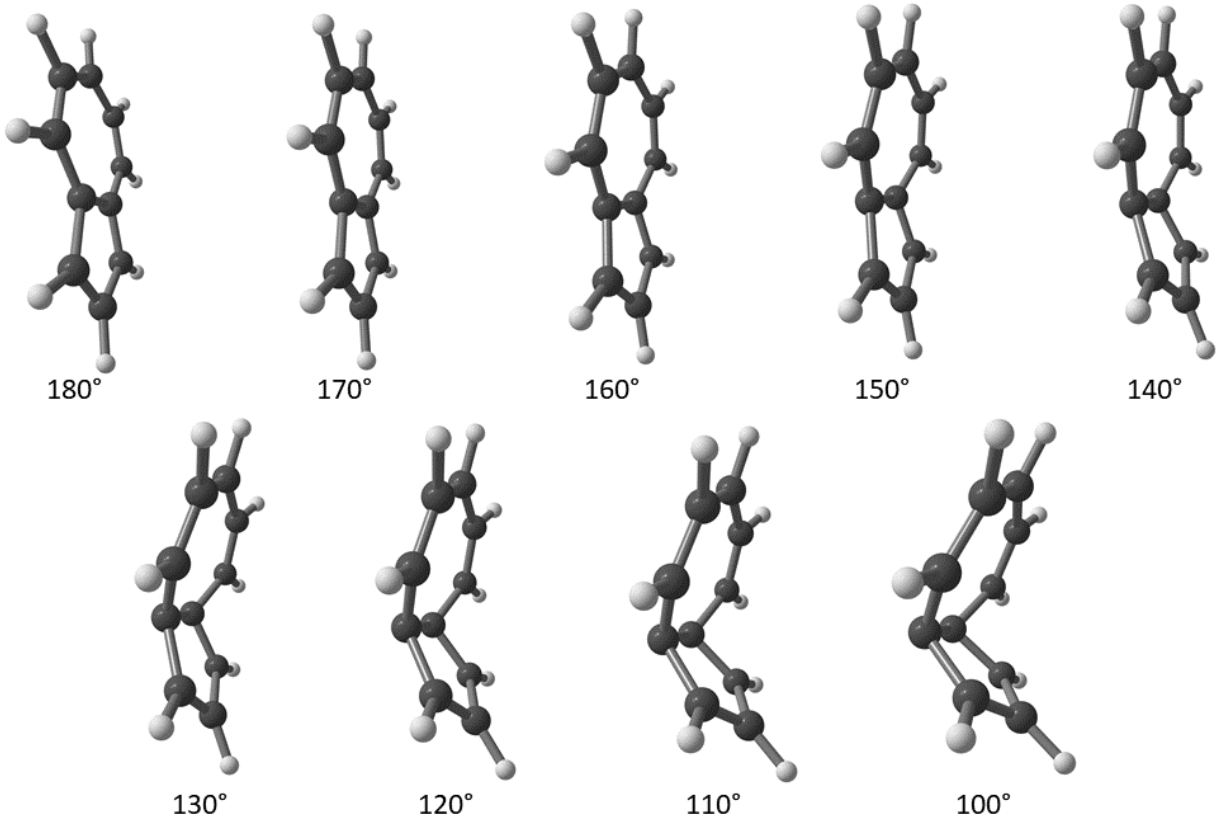

Figure F.3: Folding geometries of azulene used in Chapter 5.3.2, while fixing the dihedral angles to the angles indicated below each structure.

APPENDIX G

NITROGEN-DOPED ZTC REVIEW

Table G.1: Nitrogen-Doped ZTC Review: impregnation and CVD precursors along with template type, reported nitrogen content, BET SA, and XRD characteristics.

Author	**CVD Temperature**	**N-ZTC Precursor(s)**	**Template**	**N-content**	**BET SA** (m^2 g^{-1})	**XRD**	
						(111) reflection	**Graphitic Stacking**
Kyotani et al.[29]	700 °C	acrylonitrile	NaY	6 at%	700	None	Yes
Hou et al.[171]	800 °C	acetonitrile	NaY	4 at %	3310	Sharp	No
Yang et al.[83]	850 °C	acetonitrile	NaY	7 wt%	1918	Weak	Yes
Nishihara et al.[101]	800 °C	furfuryl alcohol & acetonitrile	NaY	3.9 at%	2900	Sharp	No
Xia et al.[84]	800 °C	acetonitrile	NaY	7.7 wt%	1912	Weak	Yes
Zhou et al.[172]	800 °C	acetonitrile	NaY	3.2 at%	2001	Weak	No
Mostazo-Lopez et al.[173]	800 °C	furfuryl alcohol & acetonitrile	NaY	3.7 at%	2760	Sharp	Yes
Han et al.[174]	600 °C	pyridine	CaY	6.5 wt%	2360	Weak	No
Han et al.[174]	600 °C	pyrrole	CaY	5.0 wt%	2520	Weak	No
Ishii et al.[117]	800 °C	acetonitrile (liquid impregnation)	NaY	2.4 at%	3620	Weak	No
Choi et al.[92]	700 °C	pyrrole	CaY	3.7 at%[a]	2420	Weak	No

[a] Converted to at% herein

APPENDIX H

NITROGEN K-EDGE XAS PEAK ASSIGNMENT REVIEW

Table H.1: Nitrogen K-edge XAS Peak Assignment Review.

Author	**Material Studied**	**π* feature locations**			**σ* feature location (eV)**
		Pyridinic (eV)	**Pyrrolic/Nitrilic/Amino (eV)**	**Graphitic (eV)**	
Shimoyama et al.[177]	Graphite-like carbon nitride	398.3	399.5	400.7	410
Gago et al.[178]	Carbon nitride thin films	398	399	400.8	405-411
Choi et al.[179]	Nitrogen-substituted MWCNT	399	-	401	408
Hellgren et al.[180]	Carbon nitride thin films	398.5	398.5-398.7	400.8-401.1	405
Zhang et al.[181]	N-substituted graphene	397.4	398.2	399.8	406
Zhong et al.[182]	N-substituted graphene	399.8	399	401	406
Schiros et al.[183]	N-substituted graphene	399	399.5	401	408
Gao et al.[184]	N-substituted reduced graphene oxide	397.2	398.3	400.0	405.2
Rabchinskii et al.[185]	N-substituted graphene	398.3	399.2	400.8	406.7
Sainio et al.[186]	Multiple Material Sources	398.4	399.7	401.1	405.1